Biaxial Fatigue Crack Growth and Crack Closure under Constant Amplitude and Periodic Compressive Overload Histories in 1045 Steel

by

Ahmad Varvani-Farahani

A thesis

Presented to the University of Waterloo

in fulfillment of the

thesis requirement for the degree of

Doctor of Philosophy

in

Mechanical Engineering

Waterloo, Ontario, Canada, 1998

The University of Waterloo requires the signatures of all persons using or photocopying this thesis. Please sign below and include the address and the date.

Abstract

This thesis examines the fatigue crack growth and crack closure mechanisms of SAE 1045 Steel under various biaxial loading conditions. The influence of periodic compressive overloads on crack growth, crack closure, and fracture surface asperity are investigated.

A new measurement technique, confocal scanning laser microscopy, is used to measure crack length and depth, crack shape, and crack opening loads by optical tomography of small fatigue cracks. This is the first time direct submicron resolution of the interior of cracks has been obtained.

Fatigue crack growth and fatigue life tests, under constant amplitude loading and block load histories containing periodic compressive overload cycles, were performed under four biaxial principal strain ratios (hoop strain/axial strain) of λ=-1 (pure shear loading), λ=-v (uniaxial loading), biaxial strain ratio of λ=-0.625, and λ=+1 (equibiaxial loading).

For biaxial strain ratios of λ=-1 and λ=-0.625, surface cracks initially nucleated on slip bands at 45° to the axis of the specimen which coincides with the plane of maximum shear strain. For these ratios, growth on shear planes (microcracks) into the specimen occupied up to 90% of the fatigue life during which time the surface length of the microcracks remained nearly constant. It was found that at about 90% of the fatigue life the aspect ratio a/c reached unity (semi-circular), and the shear cracks started growing in the

length direction as well as into the material. Failure then occurred by a rapid linking of microcracks.

In uniaxial loading (λ=-v), cracks initiated along the maximum shear plane at 45° to the surface of the specimen (Stage I growth) and failure then took place by Stage II growth perpendicular to the axis of the specimen.

In equibiaxial fatigue loading (λ=+1), cracks nucleated on the two maximum shear planes parallel and perpendicular to the specimen axis and propagated into the specimen on planes at 45° to the specimen surface. In equibiaxial fatigue loading, once a crack initiated, it grew in the length and depth directions until failure took place.

Quantitative experimental measurements of fracture surface asperity were made to investigate interference shielding at the crack tip. Asperity heights and shapes were correlated with crack growth and crack closure for both constant amplitude and periodic compressive overload biaxial fatigue tests with various strain ratios using measurements made with a Confocal Scanning Laser Microscopy (CSLM) image processing technique.

The effective strain intensity factor range was modeled based on parameters in the maximum shear strain plane in which fatigue cracks initiated. The components of the strain intensity factor range model consisting of the maximum shear strain range and the normal strain range acting on the critical plane were used as driving forces to describe the crack growth rates and predict the fatigue life.

The results of effective fatigue life predictions obtained from the various ΔK_{eff}-da/dN curves showed that the strain based critical shear plane approaches correlated the predicted and experimental effective life data within a factor of ±2 for the low cycle fatigue regime, $10^3 < N \leq 10^5$, and a factor of ±3 for high cycle fatigue regime, $N > 10^5$.

Acknowledgments

I wish to express my deepest gratitude to my supervisor, Professor Tim Topper, for his expertise, guidance, patience, and understanding. I wish to thank my cosupervisor Professor G. Glinka for providing helpful suggestions and discussions. I would also thank Professor A. Plumtree, Professor C. Thompson, and Professor H. Kerr for their suggestions and encouragement in the course of this investigation. I would like to appreciate my external examiner, Professor D. Socie, from University of Illinois at Urbana-Champaign for his invaluable suggestions.

I would like to thank my friends A. Dabayeh, C. MacDougall, H. Jahedmotlagh, A. Samani and J. Bonnen. They provided support and assistant whenever I needed it. I would also like to thank Dick Powers, Andy Barber, Peter Hanson and Ken Bowman for their help with the experimental apparatus and computer software.

I thank Professor S. Damaskinos and Professor A. E. Dixon from the Department of Physics for their kind assistance in developing CSLM technique to be used for short fatigue crack measurements.

I gratefully acknowledge the Ministry of Culture and Higher Education of Iran for my Ph.D. scholarship.

I thank my parents, and my wife who have lovingly supported me throughout the work and who have waited patiently for this day.

Lastly, I gratitude God who granted me the ability to comprehend the subject matter, and the patience and zeal to do the research as unto Him.

In The Name of God, the Beneficent, the Merciful

"....For the first time, this thesis shows direct measurements of crack depth, shape, and crack opening loads for small fatigue cracks in biaxial stress/strain fields using a novel and unique technique, Confocal Scanning Laser Microscopy, by optical tomography of small fatigue cracks with a high accuracy and resolution of 0.25 μm. This is a very important step toward a better understanding of fatigue crack growth mechanisms and understanding of the nature of fatigue damage accumulation....."

Professor Darrell Socie
University of Illinois at Urbana-Champaign
Date: Feb. 11, 1998

TO THE MEMORIES OF

MY LATE BROTHER

SHAHID MAJID VARVANI FARAHANI

Table of Contents

List of Tables

List of Figures

Nomenclature

$(da/dN)_{Overload}$:	Crack growth rate of overloads
$(da/dN)_{small}$:	Crack growth rate of small cycles
$(da/dN)_{Total}$:	Total crack growth rate
2θ:	The asperity tip angle
a:	Crack depth
A:	Maximum lateral strain
A^1_f:	Initial asperity contact area
A^1_i:	Final asperity contact area
a_f:	Crack size at failure
a_i:	Crack initiation size
B:	A constant describing the decay of total strain
c:	Half crack length
D:	Grain size
$\Delta\varepsilon$:	Cyclic strain range
$\Delta\varepsilon_a$:	Axial strain range
$\Delta\varepsilon_{fl}$:	Fatigue limit strain range
$\Delta\varepsilon_h$:	Hoop strain range
$\Delta\varepsilon_n$:	Normal strain range

$\Delta\varepsilon_{th}$: Threshold strain range

$\bar{\gamma}$: Equivalent shear strain parameter

$\gamma^{P}{}_{max}$: Plastic maximum shear strain

$\varepsilon^{P}{}_{n}$: Plastic Normal strain

$\Delta\gamma$: Cyclic shear strain range

d_i: The diameter of the ith cylindrical element in an asperity

$\Delta K^{BM}{}_{eff}$: Effective strain intensity factor range based on the Brown and Miller parameter

ΔK_{eff}: Effective strain intensity factor range

ΔK_I: Uniaxial strain intensity factor range

ΔK_{II}: Shear strain intensity factor range

$\Delta K^{K}{}_{eff}$: Effective strain intensity factor range based on the Kandil et al. parameter

$\Delta K^{s}{}_{eff}$: Effective strain intensity factor range based on the shear strain parameter

ΔK_{th}: Threshold strain intensity factor range

D_{OL}: The damage due to overload cycles

δ_{op}: Crack opening displacement

$\Delta\sigma$: Cyclic stress range

D_{SM}: The damage due to small cycles

$\Delta\sigma_n$: Normal stress range

$\Delta\tau$:	Shear stress range
D_T:	The total damage in a block load history
E:	Elastic modulus
$\varepsilon_{11}, \varepsilon_{22}, \varepsilon_{33}$:	Principal amplitude strains
ε_a:	Axial strain
ε_{ampl}:	Amplitude strain
ε_{eq}^{p}:	Equivalent plastic strain
ε_h:	Hoop strain
ε_{ij}:	Tensorial strain
ε_{ij}^{e}:	Elastic component of tensorial strain
ε_{ij}^{p}:	Plastic component of tensorial strain
ε_T^i:	True strain of ith cylindrical element in an asperity
ε_n:	Normal strain
E_p:	Plastic modulus
ε_{pco}:	Periodic compressive overstrain
ε_r:	Radial strain
ε_T:	Total true strain
Φ:	Elliptical integral
ϕ:	Normalized x by initial height of asperity (h_0)
F_I and F_{II}:	Shape factors for Mode I and Mode II loading respectively

$G=E/2(1+\nu)$:	Shear modulus
γ_{ampl}:	Amplitude shear strain
γ_{max}:	Maximum shear strain
h_0:	Initial height of asperity
h_f:	Final height of asperity
h'_0:	Initial height of ith element of an asperity
h'_f:	Final height of ith element of an asperity
φ:	The angle in the parametric equation of an ellipse
k:	Constant in the Fatemi-Socie parameter
λ:	Biaxial strain ratio
n:	Number of cycles between two overloads
ν_e:	Elastic Poisson's ratio
ν^*:	Effective Poisson's ratio
N:	Number of fatigue cycles
N_{eq}:	Equivalent fatigue life
N_f:	Number of cycles to failure (1mm crack size)
N_{fOL}:	The number of overload cycles to failure
ν_p:	Plastic Poisson's ratio
N_T:	The total number of cycles
Q:	Surface strain concentration factor
R:	Stress (strain) ratio
ρ:	The ratio of initial and final height of an asperity
S and κ:	Constants in the Kandil's parameter

σ_{11} (= σ_a):	Axial (principal) stress
σ_{22} (= σ_h):	Hoop (principal) stress
σ_{33} (= σ_r):	Radial (principal) stress
σ_a:	Amplitude stress
σ_{eq}:	Equivalent stress
S_{ij}:	Deviatoric stress tensor
σ_t:	Tensorial stress
σ_{kk}:	Summation of stresses at axial, hoop, and radial directions
σ_n:	Normal stress
σ_{pco}:	Periodic compressive overload
σ_y:	Cyclic yield stress
ω:	The ratio of hoop stress to axial stress
x:	Instantaneous distance from the tip to the base of an asperity
CAL:	Constant amplitude loading history
CSLM:	Confocal scanning laser microscopy
CSSA:	Constant shear strain amplitude loading history
HCF:	High cycle fatigue
IPCO:	In-phase periodic compressive overload cycles
LCF:	Low cycle fatigue
PCO:	Periodic compressive overload history
SEM:	Scanning electron microscope
SLRT:	Surface layer removal technique

CHAPTER 1

Introduction

Fatigue is known to be the principal cause of many mechanical failures. In spite of this fact, fatigue mechanisms are still not fully understood. This is due partly to the complex geometrical shapes and /or multiaxial loading of engineering components and structures such as pressure vessels, gas turbines, nuclear reactors, aircraft, ground vehicles, and so on.

Recently, significant attention has been devoted to fatigue crack growth under multiaxial loading. The practical importance of multiaxial fatigue crack growth requires a better understanding of the mechanisms of crack nucleation and growth under multiaxial stress loading conditions. Crack growth, under multiaxial fatigue during the very early stage of crack growth, is believed to occur along the plane of maximum shear strain.

In this chapter, first, crack initiation and early stages of crack growth under multiaxial fatigue loading are reviewed, and then multiaxial fatigue life parameters are assessed. Second, roughness induced crack closure under uniaxial and multiaxial constant amplitude loading is described and the effects of periodic compressive overload histories on crack growth and crack closure are addressed. Finally, the scope and objective of the present work is presented.

1.1 The Plane of Crack Initiation and Growth

It has long been recognized [1] that in uniaxial cyclic loading of smooth specimens, cracks nucleate on planes of intense shear deformation and propagate initially along persistent slip bands which form on or close to the maximum shear plane, inclined at 45 degrees to the tensile loading axis. Grains, whose crystallographic slip planes and directions are also oriented at 45 degrees to the tensile axis, will have the highest critical resolved shear stress on this slip plane and the highest plastic strains and will be the first to form slip bands and cracks. It is documented [2-4] that crack initiation is associated with the generation and coalescence of excess vacancies along persistent slip bands in ductile materials. Gough [5] reported that crack nucleation is dependent on the shear stress acting on the slip plane rather than on the normal stress. Peterson [6] observed that microcracks develop from persistent slip bands which then grow in an axial, transverse, or 45° direction.

There are two distinct modes of crack initiation and early growth, growth on planes of high shear stress (Mode II) or growth in planes of high tensile stress (Mode I) [7]:

Shear cracking is most likely at high strains but may occur even at low strains for pure shear loading. Brown and Miller [8] considered the nucleation and growth of fatigue cracks, and suggested the terms Case A and Case B cracks (see Fig 1.1). In Case A cracks, for torsion loading, the shear stress is in-plane and acts on the free surface in a direction parallel to the length of the crack. They suggested that there was no shear stress acting in the direction of the crack depth. Therefore, Case A cracks would tend to be shallow and have a small aspect ratio.

Tensile cracking is most likely to occur in equal biaxial stress (λ=1) but it is also common for uniaxial loading. In biaxial tension (Case B), shear stress causes the cracks to grow into the depth of the material.

1.2 Multiaxial Fatigue Cracking Behaviour

Compared to the large volume of information on the growth of fatigue cracks under uniaxial loading conditions, experimental studies on fatigue crack propagation and closure in biaxial fatigue loading are comparatively rare in the literature. Some studies have been done on crack initiation and initial growth under biaxial fatigue loading, for instance, Parson and Pascoe [9] showed that crack initiation and the direction of initial crack growth were dependent on the applied strain and biaxiality ratio. Brown and Miller [8] provided a comprehensive review of the literature on crack initiation and crack growth planes under biaxial loading. They considered nucleation and the initial growth of fatigue cracks under torsion and biaxial tension and suggested the terms Case A and Case B cracks. In Case A (torsion) the initial crack growth was along the specimen surface however, in Case B (biaxial tension), cracks grew into the specimen. Bannantine and Socie [10] provided extensive observations of cracking behaviour in tensile and torsional fatigue loading. Socie [11] mapped cracking behavior into the three regions of A, B, and C. Region A behavior was observed at short lives. Microcracks were initiated on shear planes. Region B behavior was observed only at long lives and growth occurred on the tensile plane by a linking of previously initiated shear cracks. Region C behavior was observed at the longest lives in torsion. A small number of cracks were initiated on the shear planes, but they quickly branched to Stage II planes. Growth on these planes occurred by the propagation of the main crack rather than by the linking process.

The results of the SAE 1045 steel torsion tests reported by Socie [11] revealed that the cracks were initiated and remained on the maximum shear plane (Region A) throughout the fatigue life. Region B behavior occurred at the lowest strain amplitude of 0.24%. The crack branched and growth occurred on the tensile plane by the linking of shear plane cracks created in Region A. The final failure occurred by a mixture of Region A and Region B behavior.

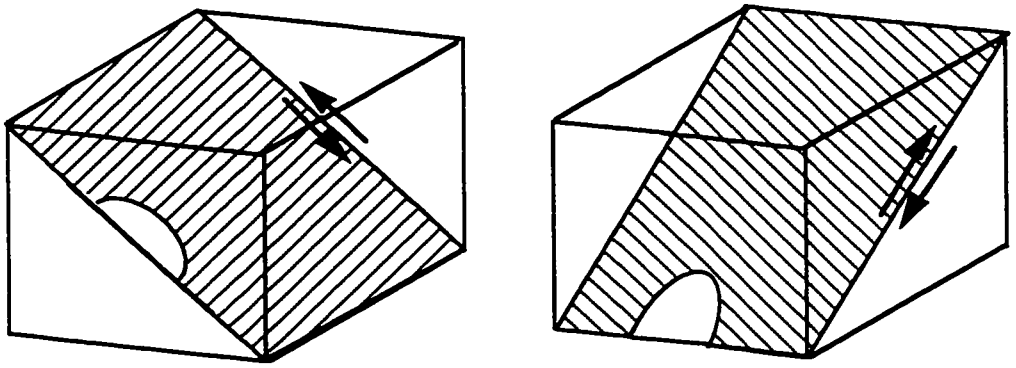

Fig 1.1 Crack nucleation and growth plane : a) Case A and b) Case B [8].

In Fig 1.2, the vertical axis gives the life fraction (N/N_f), which the horizontal axis is given fatigue life (N_f) in cycles. The lower curve represents the first observation of a surface crack length of 100 μm and serves as a demarcation between crack nucleation and growth and the upper curve represents the demarcation between crack growth on planes of maximum shear strain and crack growth on the planes of maximum principal strain amplitude. In Fig 1.2b [11] the lower line indicates the life to reach a crack of 0.1 mm. Hence, a specimen with a failure life of less than 20,000 cycles undergoing tension loading would reach a crack length of 0.1 mm at N/N_f=0.24 and continue cracking on the shear planes. Life fraction of N/N_f=0.8 corresponds to the crack growth on the tensile planes (Region B) and continues until failure.

1.3 Multiaxial Fatigue Life Parameters

Many engineering components that undergo fatigue loading experience multiaxial stresses, in which two or three principal stresses fluctuate with the time. Our knowledge of multiaxial fatigue has developed over many decades. The complete reviews of multiaxial development are presented by Socie [11], Brown and Miller [12], and You and Lee [13]. Methods for predicting the multiaxial fatigue life are briefly summarized.

1.3.1 Equivalent stress (strain) approaches

The most commonly used approach for the evaluation of multiaxial fatigue life transforms cyclic multiaxial stresses into an equivalent uniaxial stress amplitude thought to produce the same fatigue life as the multiaxial stresses. The most popular methods for making the transformation are extensions of the von Mises yield criterion, in which static values of principal stress are replaced by amplitudes and the yield strength is replaced by uniaxial fatigue strength. Jordan [14] and Garud [15] showed that the von Mises criterion was limited to correlating multiaxial life data under proportional loading in the high cycle fatigue regime.

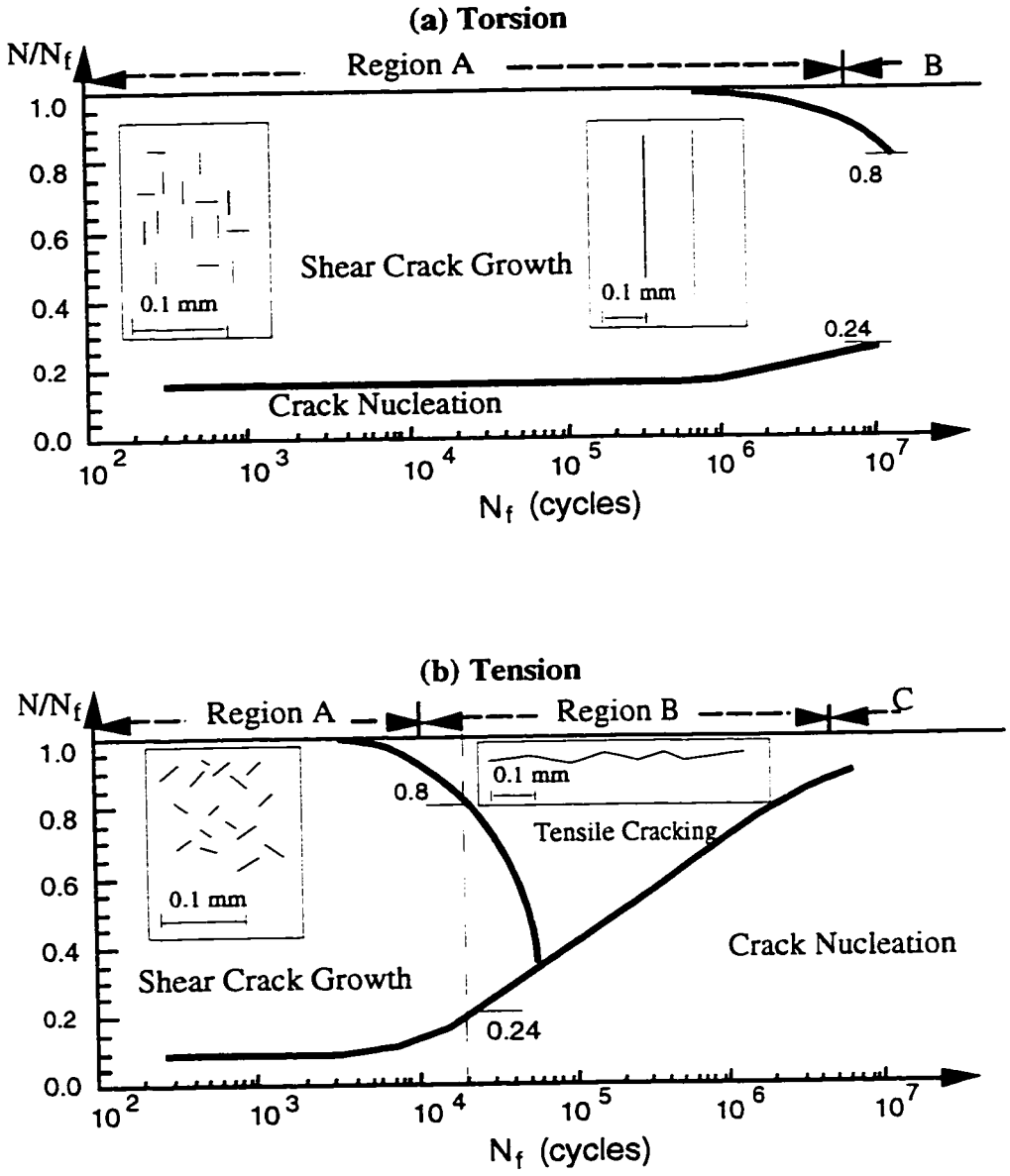

Fig 1.2 Cracking behavior observed in normalized 1045 Steel a) Torsion, and b) Tension [11]

1.3.2 Energy approach

Fatigue is generally believed to involve cyclic plastic deformations which are dependent on the stress-strain path. The energy concept includes an explicit consideration of the multiaxial stress-strain response. Garud [16] applied this approach in conjunction with incremental plasticity theory to predict fatigue crack initiation life under complex non-proportional multiaxial loading conditions. The approach did not successfully correlate the uniaxial and torsional fatigue life data obtained for 1% Cr-Mo-V steel. Ellyin et al. [17-18] tried to correlate uniaxial and torsional data using the total strain energy density. Ellyin and Golos [19] proposed that the durability of components should be characterized by the quantity of energy which a material could absorb. They proposed a ratio of axial strain to maximum shear strain to correlate multiaxial life data. You and Lee [13] criticized the ratio presented by Ellyin and Golos because the hysteresis energy method they used, does not hold any terms to reflect this strain ratio.

The energy approach was criticized by Fatemi and Socie [20] for its inability to account for differences in damage done by normal and by shear stresses and its lack of a way of accounting for the directionality of crack formation and growth in multiaxial fatigue.

1.3.3 Critical shear plane theories

Fatigue analysis using the concept of a critical plane of maximum shear strain is very effective because the critical plane concept is based on the fracture mode or the initiation mechanism of cracks. In the critical plane concept, after determining the maximum shear strain plane, many researchers define the parameter as a combination of the maximum shear strain (or stress) and normal strain (or stress) on that plane to explain multiaxial fatigue behavior [8,15,21,22]. Strain terms are used in the region of low cycle fatigue (LCF) and stress terms are used in the high cycle fatigue (HCF) region with critical plane approaches to multiaxial fatigue analysis. Brown and Miller [8] tried to analyze multiaxial

fatigue in the LCF region by using the state of strain on the plane where maximum shear strain occurred, while Findley et al. [21] and Stulen and Commings [23] used stress terms in the HCF region. The following reviews some critical plane approaches.

Shear strain parameter (Tresca)- the earliest shear plane theory used the shear strain amplitude on the plane of maximum shear strain amplitude to correlate fatigue lives for different biaxial strain ratios.

$$\gamma_{max} = \text{Max}\left[|\varepsilon_a - \varepsilon_r| \text{ or } |\varepsilon_a - \varepsilon_h| \text{ or } |\varepsilon_h - \varepsilon_r|\right] \tag{1.1}$$

Brown and Miller [8] proposed that fatigue cracks initiate on the planes of maximum shear strain and hypothesized that the maximum shear strain amplitude (γ_{max}) and the amplitude of the strain normal to the plane of maximum shear strain (ε_n) were the critical parameters governing fatigue damage. The Brown-Miller life parameter is defined as

$$\frac{\Delta\gamma_{max}}{2} + C\,\Delta\varepsilon_n = \text{Constant} \tag{1.2}$$

where $\Delta\gamma_{max}$ and $\Delta\varepsilon_n$ are the maximum shear strain range and normal strain range on the maximum shear strain plane, respectively. A value of the constant C of 0.30 was chosen to best fit the data.

The Lohr and Ellison [24] parameter is similar to the Brown and Miller parameter. However, the shear strain that dominates failure acts on a plane inclined at 45° to the surface, i.e., the through thickness shear strain is assumed to drive the crack until failure takes place.

Kandil et al. [25] derived the following equivalent shear strain parameter for correlating multiaxial fatigue data

$$\bar{\gamma} = 2\left[\left(\frac{\gamma_{max}}{2}\right)^{\kappa} + S\,\varepsilon_n{}^{\kappa}\right]^{\frac{1}{\kappa}} \qquad (1.3)$$

Kandil et al. [25] found the value of the constant κ ranged from 0.50 to 3.0. The values of the constants κ and S were chosen and calculated (see Appendix D) to give the best fit curve to fatigue data .

Socie and Shield [26] performed experiments to examine the effect of mean stress under multiaxial fatigue loading with a tubular specimen of Inconel 718. They suggested the following parameter

$$\gamma^p{}_{max} + \varepsilon^p{}_n + \frac{\sigma_n}{E} = f(N_f) \qquad (1.4)$$

where $\gamma^p{}_{max}$ and $\varepsilon^p{}_n$ are the plastic maximum shear strain and the plastic normal strain respectively and σ_n is the component of mean stress applied on the maximum shear strain plane.

Fatemi and Socie [20] have demonstrated a robust correlation of fatigue data for various stress states for both case A and case B histories with and without mean stress, based on the assumption that peak normal stress to the plane of maximum range of shear strain directly affects the Stage I shear-dominated propagation of small cracks. They proposed the following parameter

$$\frac{\Delta\gamma_{max}}{2}\left[1 + k\frac{\sigma_n}{\sigma_y}\right] = f(N_f) \qquad (1.5)$$

where k is a constant equal to 0.60 for 1045 steel [20], and σ_n and σ_y are the normal stress and yield stress, respectively.

Glinka et al. [27] proposed a multiaxial life parameter based on the summation of the products of normal and shear strains and stresses on the critical shear plane as

$$W^{*} = \frac{\Delta\gamma}{2}\frac{\Delta\tau}{2} + \frac{\Delta\varepsilon_n}{2}\frac{\Delta\sigma_n}{2} \qquad (1.6)$$

where $\Delta\gamma$ and $\Delta\tau$ are the shear strain range and shear stress range on the critical shear plane respectively and $\Delta\varepsilon_n$ and $\Delta\sigma_n$ are the normal strain range and normal stress range to the critical shear plane respectively.

Jadaan and Boys [28] proposed two energy parameters associated with two different physical modes of failure. The first parameter is a Mode I energy parameter associated with the critical plane where principal stress and strain take place, while the second parameter is a Mode II energy parameter associated with the critical planes where maximum shear stresses and strains occur. For the Mode II energy parameter they suggested a relation similar to equation (1.6).

1.4 Asperity Induced Crack Closure

Elber [29] showed a fatigue crack in a body experiencing positive cyclic loading remains fully open only at high load levels. At lower loads, the crack fracture surfaces come into premature contact at some distance behind the crack tip and the crack remains closed during part of the loading as well as the unloading phase of the cycle.

Roughness induced crack closure results from the mismatch of opposing fracture surface topography. Walker and Beevers [30] showed that plasticity induced closure was not responsible for the crack closure they observed in the titanium alloy which they tested. Microstructurally sensitive fatigue crack growth in this metal produced an extensive faceted formation in favorably oriented grains whose average grain size was 20 μm. These variously oriented facets interconnected to produce non-planar cracks and erratic crack growth behaviour. The mismatch of these facets during unloading resulted in premature

crack closure. They concluded that closure did not result from residual plasticity but from the non-planar crack geometry.

The earliest analysis to quantify the effect of fracture surface roughness on fatigue crack closure was presented by Purushothaman and Tien [31]. These authors suggested that the closure stress intensity K_{cl} can be estimated by equating the change in fracture surface asperity height to the crack opening displacement.

Minakawa and McEvily [32] attributed the high closure levels found in near threshold stress intensity regions to the result of increased shear facets and a serrated fracture surface profile. They reasoned that this roughness-induced closure was related to mixed mode (Mode II-Mode I) crack growth.

Suresh and Ritchie [33] proposed an alternative description for fracture roughness-induced crack closure in the form of a two dimensional geometric model by incorporating both Mode I and Mode II displacements.

Morris et al. [34] proposed a model which related the threshold value of cyclic stress intensity (required for crack propagation) ΔK_{th} to the crack closure stress arising from fracture surface roughness.

Shouxin et al. [35] proposed a geometrical model dealing with roughness-induced crack closure under Mode I displacement in the absence of Mode II and III displacements at the crack tip. They reported that the hypotheses of plane strain and Mode II crack displacements at the crack tip for roughness-induced crack closure are not satisfied on a microscopic scale, the fracture surface at the tip of the crack is not smooth and angles of inclination of the small strips (facets) near the crack tip are quite different.

Carlson and Beevers [36] proposed a closure model based on contact between impinging fracture surface asperities. Asperity angle, magnitude of Mode II interference,

friction between contacting surfaces and distance of contact surfaces from the crack tip are considered in this model.

Tschegg [37] proposed a sliding mode crack closure for Mode III crack growth in which the crack remains closed but the fracture surfaces move parallel to each other. He related this closure to the appearance of the fracture surface of materials sliding against each other.

Based on these models roughness induced crack closure is significantly affected by the size, shape, and distribution of fracture surface irregularities and the type load histories. The following section provides a brief review of the effect of periodic overloads on the fracture surface irregularities and eventually on crack closure and growth rate.

1.5 The Effect of Periodic Compressive Overloads on Crack Growth and Closure

The effect of compressive overload cycles has been the subject of a number of experimental programs during the past several years. A review of the results of these investigations indicates that compressive overloads contribute significantly to fatigue crack growth. A comprehensive review of crack growth under variable amplitude loading was done by Geary [38]. Variable amplitude crack growth tests involving compressive overloads have generally shown accelerated growth rates when compared to constant amplitude test data [39-41]. Stephens et al. [39] tested specimens of 2024-T3 aluminum and 7075-T6 aluminum. They found that compressive overloads caused an accelerated crack growth and a reduced fatigue life. These effects have been attributed to the flattening of crack asperities, which leads to a reduction of crack closure.

There has been relatively little work describing crack growth and crack closure under compressive overloads that approach or exceed cyclic yield stress. Most of the work done involves tests of long fatigue cracks under loads that are a fraction of the cyclic yield

stress. Crack behaviour under a high magnitude of stress is noteworthy because as Topper et al.[42] pointed out, notch root strains under service loading usually exceed the cyclic yield stress at the highest load levels. Furthermore, for a finite life design of a structural component, most of the life will be characterized by short crack lengths. Topper and Yu [43] found that compressive overloads significantly decreased the threshold stress intensity and increased the crack propagation rate for 2024-T351 aluminum alloy and for three steel alloys. The magnitude of compressive overload applied was a high fraction of the material's yield stress. They observed that the crack opening stress decreased below zero following the compressive overloads.

Varvani and Topper [44-45] conducted several biaxial fatigue tests under various biaxiality ratios on 1045 steel thin-walled tubular specimens. They applied both constant amplitude loading and load histories containing periodic compressive overloads of yield stress magnitude. They reported that the application of the periodic compressive overloads of yield point magnitude left the crack open at zero load. They attributed this reduced crack closure to the plastic crushing of crack face asperities under compressive overloads. This resulted in an increase in the effective strain intensity factor range and crack growth rate.

Kemper et al. [46] and Tack and Beevers [47] observed a saturation effect during tests having compressive overloads in which an increase in compressive overload magnitude beyond a certain level did not result in an additional increase in crack growth rate. The reduction of asperity heights could reasonably be subject to a limiting plastic deformation as the asperity contact areas are increased under increasing compressive overloads. Varvani and Topper [48], showed a similar saturation in the increase of crack growth rate in 1045 steel specimens loaded under a uniaxial fatigue load history containing periodic compressive overload cycles. They found that as the magnitude of compressive overloads increased cracks grew faster. In this study, the saturation of the crack growth

rate at a periodic compressive overload level of -430 MPa was shown to correspond to closure free crack growth.

1.6 Objective and Outline of the Research

This thesis examines fatigue crack growth and crack closure mechanisms of SAE 1045 Steel under various biaxial loading conditions. The influence of periodic compressive overloads on crack growth, crack closure mechanism, and fracture surface asperity are investigated.

Quantitative experimental measurements of fracture surface asperity were made to investigate interference shielding at the crack tip. Asperity heights and shapes were correlated with crack growth and crack closure for biaxial fatigue tests with various stress ratios using measurements made with a Confocal Scanning Laser Microscopy (CSLM) image processing technique. The inclination of the crack growth plane, crack length and crack depth, and crack shape, crack opening stress levels, and fracture surface asperity geometry have been determined in this study. Finally, biaxial fatigue crack growth rates have been modeled and used to predict fatigue life. This thesis is divided into seven chapters.

Chapter 1 presents a review of the features of multiaxial fatigue which are relevant to this study.

Chapter 2 provides background concerning the analysis of stress and strain states required in this study.

Chapter 3 describes the material, apparatus, experimental procedures and techniques used in this research.

Chapter 4 contains fatigue tests results for constant amplitude loading and load histories containing periodic compressive overload cycles. This chapter also presents measurements of crack shape and growth mechanisms under various biaxiality ratios and provides crack growth and crack depth measurements under constant amplitude loading and periodic compressive overload histories. Crack opening stress data are also presented.

Chapter 5 examines the influence of periodic compressive overloads on the fracture surface asperities of short fatigue cracks, crack growth and closure under uniaxial and biaxial fatigue loading. A model of the plastic deformation of asperities is developed which correlates the compressive overload, fracture surface asperity contact areas, and the initial and final geometry of asperities before and after the application of a compressive overload. This chapter provides evidence that cracks are open at zero load when a periodic compressive overload of yield stress magnitude is applied.

Chapter 6 provides a biaxial fatigue life evaluation based on strain based critical plane approaches for constant amplitude loading and for load histories having periodic compressive overloads of yield stress magnitude. This chapter provides biaxial fatigue crack growth rate modeling based on strain based critical plane parameters for fully effective (closure free) fatigue data obtained for load histories having periodic compressive overloads of yield stress magnitude and various biaxial strain ratios. Fatigue life predictions for the various biaxiality ratios based on various life parameters are presented.

Chapter 7 discusses conclusions and presents the some suggestions for future research.

CHAPTER 2

Stress and Strain State and Analysis

2.1 Stress and Strain State

In the present study, biaxial fatigue tests were performed on thin-walled tubular fatigue specimens. The two controlled applied strains were the principal strains in the plane of the tube. Fig 2.1 presents the state of stress and strain for a thin-walled tubular specimen which in a stress tensor form is

$$\sigma_{ij} = \begin{bmatrix} \sigma_{11} & 0 & 0 \\ 0 & \sigma_{22} & 0 \\ 0 & 0 & \sigma_{33} = 0 \end{bmatrix} \qquad (2.1)$$

where σ_{ij} is the stress tensor (i and j=1,2,3), and the stress components σ_{11}, σ_{22}, and σ_{33} are principal stresses. Since the thin-walled tubular specimens are in a plane stress condition, $\sigma_{33} = \sigma_r = 0$, $\sigma_{22} = \sigma_h$, and $\sigma_{11} = \sigma_a$ where subscripts r, h, and a correspond to the radial, hoop, and axial directions on a thin-walled tubular specimen. The radial stress is taken to be zero because only the stresses in this direction are the small stresses due to oil pressure.

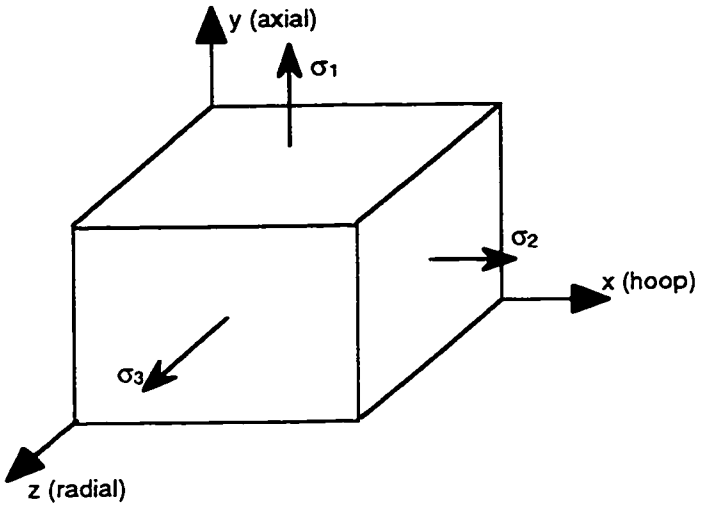

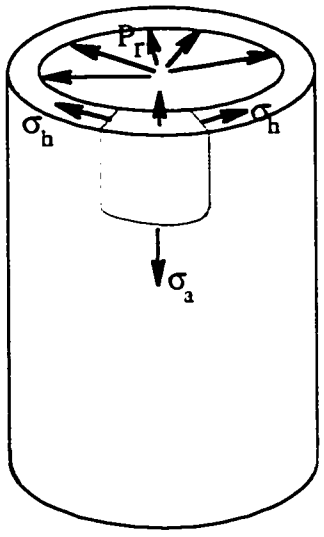

Thin-walled tubular specimen

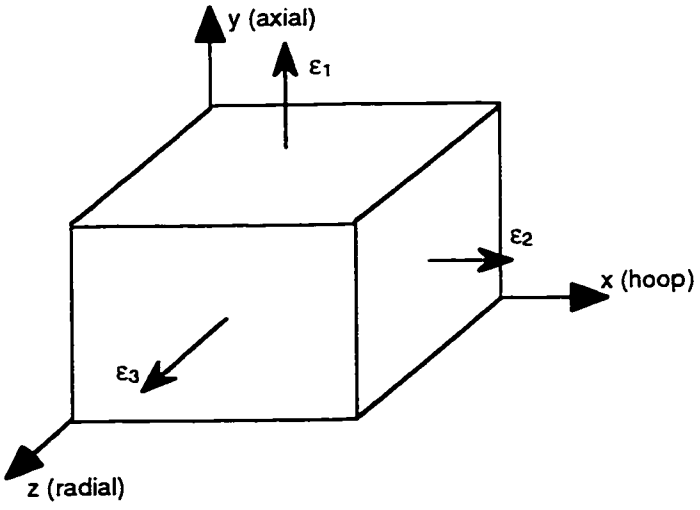

Fig 2.1 Stress and strain state on a thin-walled tubular specimen under plane stress condition.

The state of strain for the thin-walled tubular specimen in the tensorial form is

$$\varepsilon_{ij} = \begin{bmatrix} \varepsilon_{11} & 0 & 0 \\ 0 & \varepsilon_{22} & 0 \\ 0 & 0 & \varepsilon_{33} \end{bmatrix} \qquad (2.2)$$

where ε_{ij} is the strain tensor (i and j=1,2,3) the strain components ε_{11}, ε_{22}, and ε_{33} are principal strains where, $\varepsilon_{33}= \varepsilon_r$, $\varepsilon_{22}= \varepsilon_h$, and $\varepsilon_{11}= \varepsilon_a$. Again the subscripts r, h, and a represent the radial, hoop and axial directions respectively.

To show the stress-strain state, a Mohr's circle representation of strain at a point in time during the loading cycle is used. Fig 2.2 presents the strain Mohr's circles for four biaxial strain ratios of λ=-v, -0.625, -1, and +1 in a thin-walled tubular specimen.

Using strain Mohr's circles, the maximum shear strain γ_{max} and the normal strain ε_n from the largest Mohr's circle are obtained as

$$\gamma_{max} = \varepsilon_a - \varepsilon_h \qquad (2.3)$$

and

$$\varepsilon_n = \frac{\varepsilon_a + \varepsilon_h}{2} \qquad (2.4)$$

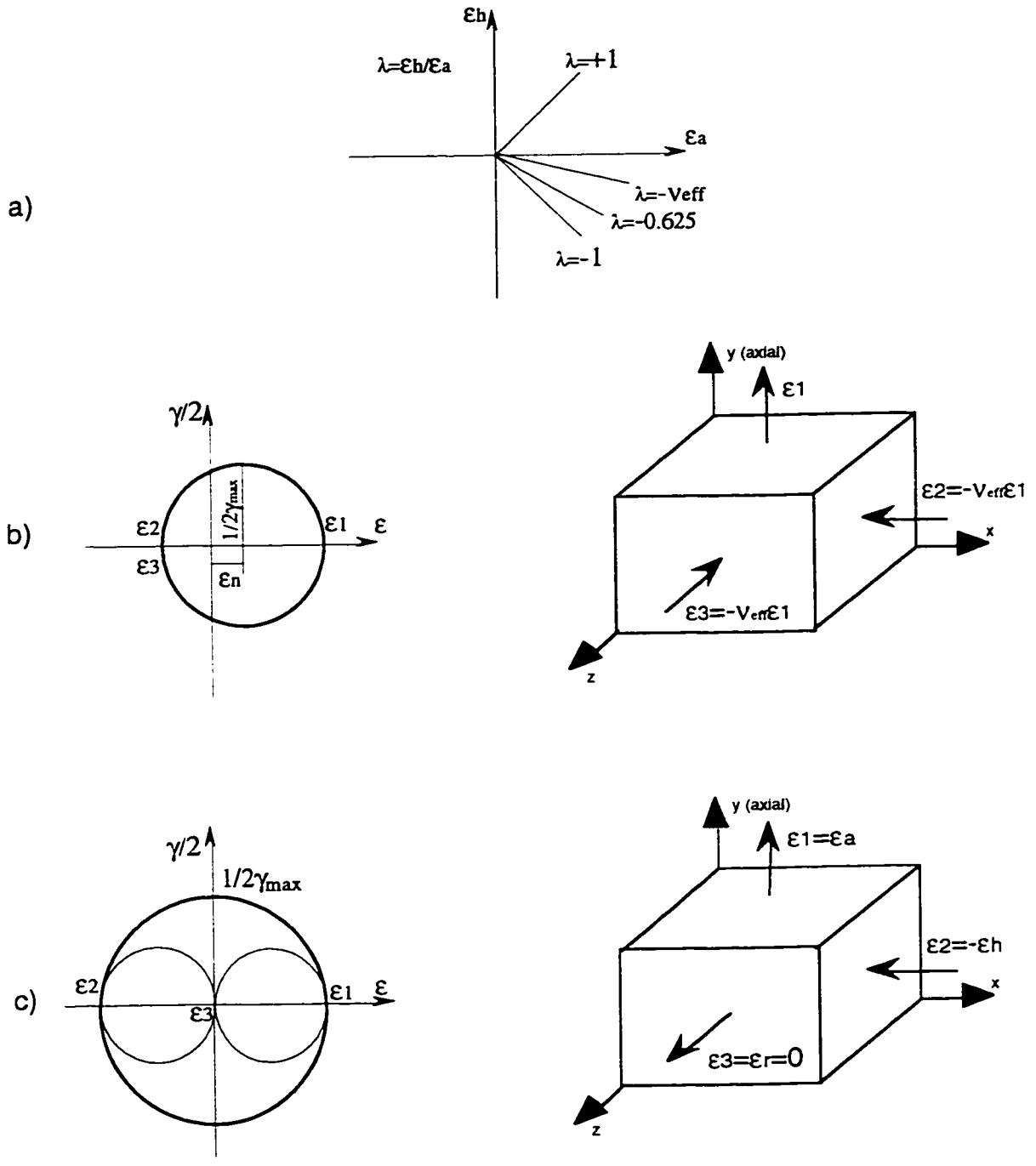

Fig 2.2 a) Biaxial strain ratio λ , b, c, d and e) strain state and Mohr's circle for strain ratios of -ν, -1, -0.625, and +1.

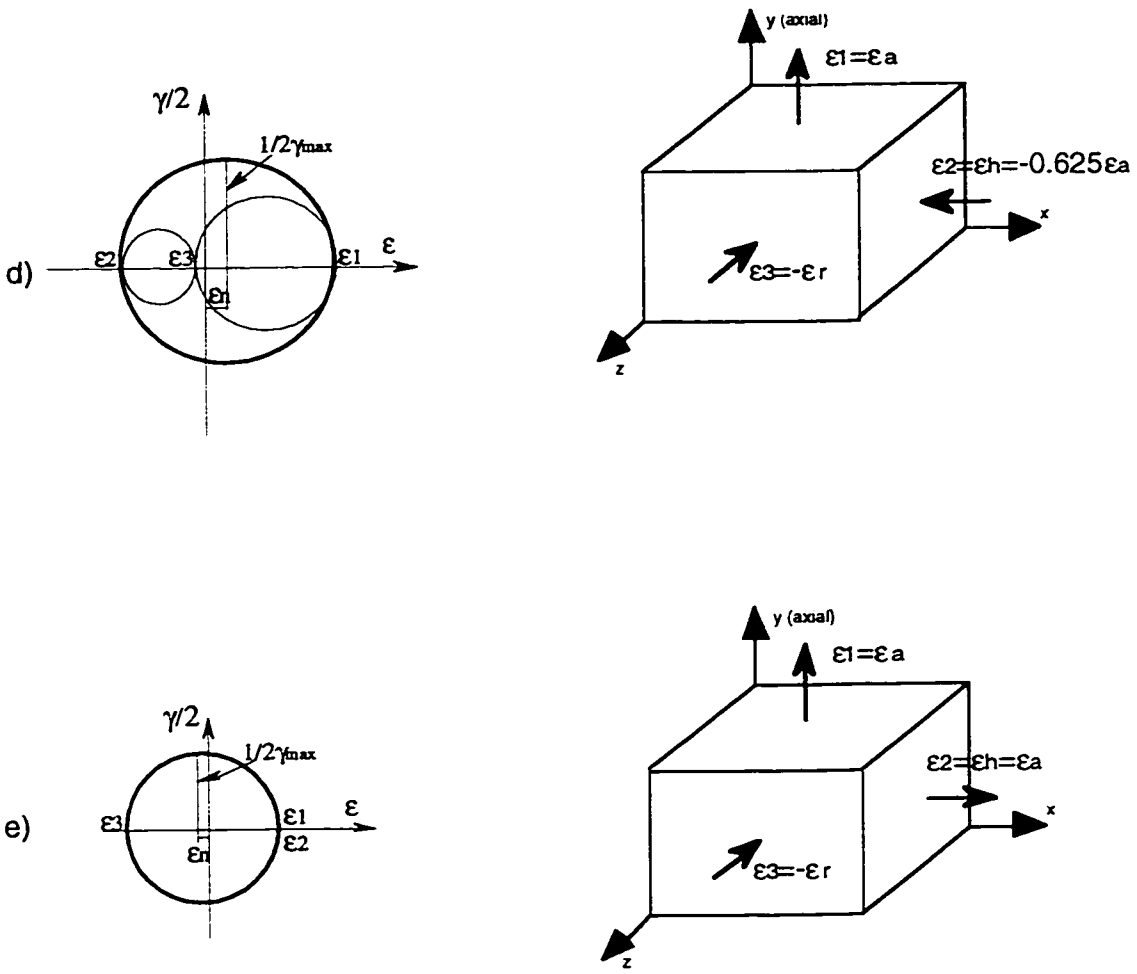

Fig 2.2 continued.

2.1.1 Strain state for various biaxiality ratios

Uniaxial fatigue loading ($\lambda=-\nu$), for plane stress condition, $\varepsilon_{11}=\varepsilon_a$, $\varepsilon_{22}=-\nu_{eff}\varepsilon_a$ and $\varepsilon_{33}=-\nu_{eff}\varepsilon_a$. For uniaxial loading the strain tensor can be written as

$$\varepsilon_{ij}=\begin{bmatrix}\varepsilon_a & 0 & 0\\ 0 & -\nu_{eff}\varepsilon_a & 0\\ 0 & 0 & -\nu_{eff}\varepsilon_a\end{bmatrix} \qquad (2.5)$$

Shear fatigue loading ($\lambda=-1$), for pure shear loading of a thin-walled tubular specimen, $\sigma_{33}=\sigma_r=0$, $\varepsilon_{11}=\varepsilon_a$, $\varepsilon_{22}=\varepsilon_h$ and $\varepsilon_{33}=\varepsilon_r=0$ where , $\varepsilon_a=-\varepsilon_h$. For pure shear loading the tensorial strain is

$$\varepsilon_{ij}=\begin{bmatrix}\varepsilon_a & 0 & 0\\ 0 & \varepsilon_h & 0\\ 0 & 0 & 0\end{bmatrix} \qquad (2.6)$$

Biaxial fatigue loading ($\lambda=-0.625$), for a thin-walled tubular specimen, $\sigma_{33}=\sigma_r=0$, $\varepsilon_{11}=\varepsilon_a$, $\varepsilon_{22}=\varepsilon_h$ and $\varepsilon_{33}=\varepsilon_r$ where , $\varepsilon_a=-0.625\varepsilon_h$. For biaxial fatigue loading of $\lambda=-0.625$, the strain tensor is

$$\varepsilon_{ij}=\begin{bmatrix}\varepsilon_a & 0 & 0\\ 0 & \varepsilon_h & 0\\ 0 & 0 & \varepsilon_r\end{bmatrix} \qquad (2.7)$$

Equibiaxial fatigue loading ($\lambda=+1$), for a thin-walled tubular specimen, $\varepsilon_{11}=\varepsilon_a$, $\varepsilon_{22}=\varepsilon_h$ and $\varepsilon_{33}=\varepsilon_r$ where , $\varepsilon_a=\varepsilon_h$. For equibiaxial fatigue loading, the strain tensor is

$$\varepsilon_{ij} = \begin{bmatrix} \varepsilon_a & 0 & 0 \\ 0 & \varepsilon_h & 0 \\ 0 & 0 & \varepsilon_r \end{bmatrix} \tag{2.8}$$

2.2 Stress and Strain Analysis

When a material is loaded beyond its elastic limit, it undergoes permanent plastic deformation. Plastic flow in metals can be assumed to be incompressible. The total strain imposed on an elastic-plastic solid, ε_{ij}, can be written as the sum of the elastic and plastic strains ε_{ij}^{e} and ε_{ij}^{p}, respectively as

$$\varepsilon_{ij} = \varepsilon_{ij}^{e} + \varepsilon_{ij}^{p} \tag{2.9}$$

The elastic and plastic behaviour under uniaxial and biaxial loading are described by constitutive laws which relate the strains and stresses.

2.2.1 Constitutive equations

2.2.1.1 Elastic strains

Hook's law for elastic strains can be presented as [7, 49-50]

$$\varepsilon_h^{e} = \frac{1}{E}\left[\sigma_h - \nu_e(\sigma_a + \sigma_r)\right] = \frac{1+\nu_e}{E}\sigma_h - \frac{\nu_e}{E}(\sigma_h + \sigma_a + \sigma_r) \tag{2.10}$$

Equation (2.10) in a general form can be written as

$$\varepsilon_{ij}^{e} = \frac{1+\nu_e}{E}\sigma_{ij} - \frac{\nu_e}{E}\sigma_{kk}\,\delta_{ij} \tag{2.11}$$

where
$$\begin{aligned} \delta_{ij} &= 1 \quad \text{if} \quad i = j \\ \delta_{ij} &= 0 \quad \text{if} \quad i \neq j \end{aligned} \tag{2.11a}$$

where E is the elastic modulus and the ν_e=0.30 is the elastic Poisson's ratio for the steel used in this thesis and σ_{kk} is the summation of stresses at axial, hoop, and radial directions.

For the plane stress condition ($\sigma_{33}= \sigma_r =0$)

The elastic strain in the axial direction, ε_a^e, is

$$\varepsilon_a^e = \frac{1}{E}\left[\sigma_a - \nu_e(\sigma_h)\right] \tag{2.12a}$$

The elastic strain in the hoop direction, ε_h^e, is

$$\varepsilon_h^e = \frac{1}{E}\left[\sigma_h - \nu_e(\sigma_a)\right] \tag{2.12b}$$

The elastic strain in the radial direction, ε_r^e, is

$$\varepsilon_r^e = -\frac{\nu_e}{E}(\sigma_a + \sigma_h) \tag{2.12c}$$

2.2.1.2 Plastic strains

Equations analogous to Hook's law are used to relate stresses and plastic strains. The plastic strain components in the axial, hoop, and radial directions are calculated respectively as

$$\varepsilon_a^p = \frac{1}{E_p}\left[\sigma_a - \nu_p(\sigma_h + \sigma_r)\right] \tag{2.13a}$$

$$\varepsilon_h^p = \frac{1}{E_p}\left[\sigma_h - \nu_p(\sigma_a + \sigma_r)\right] \tag{2.13b}$$

and

$$\varepsilon_r^p = \frac{1}{E_p}\left[\sigma_r - \nu_p(\sigma_h + \sigma_a)\right] \tag{2.13c}$$

where ν_p=0.5 is the plastic Poisson's ratio. For the plane stress condition ($\sigma_{33}= \sigma_r$=0), and the plastic constitutive equations simplify to

$$\varepsilon_a^p = \frac{1}{E_p}\left[\sigma_a - \tfrac{1}{2}\sigma_h\right] \tag{2.14a}$$

$$\varepsilon_h^{\,p} = \frac{1}{E_p}\left[\sigma_h - \tfrac{1}{2}\sigma_a\right] \tag{2.14b}$$

and

$$\varepsilon_r^{\,p} = \frac{-1}{2E_p}\left(\sigma_h + \sigma_a\right) \tag{2.14c}$$

The plastic modulus E_p is the secant of modulus to a point on the equivalent stress versus equivalent plastic strain curve [7]

$$E_p = \frac{\sigma_{eq}}{\varepsilon_{eq}^{\,p}} \tag{2.15}$$

The relationship between the equivalent plastic strain $\varepsilon_{eq}^{\,p}$ and equivalent stress σ_{eq} obtained from uniaxial stabilized stress-strain data was

$$\varepsilon_{eq}^{\,p} = 2.63 * 10^{-9}\ (\sigma_{eq})^{2.8} \tag{2.16}$$

The equivalent plastic strain versus equivalent stress relationship will be presented in the next section of this chapter.

Equations (2.15) in terms of the deviatoric stress tensor can be written as

$$\varepsilon_{ij}^{\,p} = \tfrac{3}{2} S_{ij} \frac{\varepsilon_{eq}^{\,p}}{\sigma_{eq}} \tag{2.17}$$

The deviatoric stress S_{ij} is defined as the difference between the tensorial stress and hydrostatic stress $(\frac{1}{3}\sigma_{kk})$

$$S_{ij} = \sigma_{ij} - \frac{1}{3}\sigma_{kk}\,\delta_{ij} \tag{2.18}$$

2.2.1.3 Elastic-plastic strains

The total strain is composed of elastic and plastic parts. The total strain components in the axial and hoop directions were measured and controlled using axial and radial extensometers mounted on the thin-walled tubular specimen.

The constitutive equations for elastic-plastic behavior are written as

$$\varepsilon_{ij} = \left[\frac{1+\nu_e}{E}\sigma_{ij} - \frac{\nu_e}{E}\sigma_{kk}\delta_{ij}\right] + \left[\frac{3}{2}S_{ij}\frac{\varepsilon_{eq}^{\ p}}{\sigma_{eq}}\right] \qquad (2.19)$$

In equation (2.19) the first bracket presents the elastic component of strain and the second bracket presents the plastic component of strain.

2.2.1.4 Strain and stress components for various biaxiality ratios

Uniaxial case ($\lambda=-\nu_{eff}$), considering the state of strain under uniaxial case, $\varepsilon_{11}=\varepsilon_a$, $\varepsilon_{22}=-\nu_{eff}\,\varepsilon_a$ and $\varepsilon_{33}=-\nu_{eff}\,\varepsilon_a$, constitutive equation (2.19) for uniaxial elastic-plastic behaviour is reduced to

$$\varepsilon_{11} = \left[\frac{1+\nu_e}{E}\sigma_{11} - \frac{\nu_e}{E}\sigma_{11}\right] + \left[\frac{3}{2}\left(\sigma_{11} - \frac{1}{3}\sigma_{11}\right)\sigma_{11}^{1.8}(2.63*10^{-9})\right] \qquad (2.20a)$$

which results in the following Ramberg-Osgood equation as

$$\varepsilon_{11} = \frac{\sigma_{11}}{E} + \left(\frac{\sigma_{11}}{1159.58}\right)^{2.8} \qquad (2.20b)$$

Biaxial case (λ**=-0.625, -1, and +1**), considering the plane stress condition and the state of strain under the biaxial case; $\sigma_{33}=\sigma_r=0$, $\varepsilon_{11}=\varepsilon_a$, $\varepsilon_{22}=\varepsilon_h$ and $\varepsilon_{33}=\varepsilon_r$, the constitutive equations for ε_{11} and ε_{22} are

$$\varepsilon_{11} = \left[\frac{1+\nu_e}{E}\sigma_{11} - \frac{\nu_e}{E}(\sigma_{11}+\sigma_{22})\right] + \left[\frac{3}{2}\left(\sigma_{11} - \frac{1}{3}(\sigma_{11}+\sigma_{22})\right)(2.63*10^{-9})\left(\sqrt{\tfrac{1}{2}[(\sigma_{11}-\sigma_{22})^2+(\sigma_{11})^2+(\sigma_{22})^2]}\right)^{1.8}\right] \quad (2.21a)$$

$$\varepsilon_{22} = \left[\frac{1+\nu_e}{E}\sigma_{22} - \frac{\nu_e}{E}(\sigma_{11}+\sigma_{22})\right] + \left[\frac{3}{2}\left(\sigma_{22} - \frac{1}{3}(\sigma_{11}+\sigma_{22})\right)(2.63*10^{-9})\left(\sqrt{\tfrac{1}{2}[(\sigma_{11}-\sigma_{22})^2+(\sigma_{11})^2+(\sigma_{22})^2]}\right)^{1.8}\right] \quad (2.21b)$$

and

$$\varepsilon_{33} = \left[-\frac{\nu_e}{E}(\sigma_{11}+\sigma_{22})\right] + \left[\left(-\frac{1}{2}(\sigma_{11}+\sigma_{22})\right)(2.63*10^{-9})\left(\sqrt{\tfrac{1}{2}[(\sigma_{11}-\sigma_{22})^2+(\sigma_{11})^2+(\sigma_{22})^2]}\right)^{1.8}\right] \quad (2.21c)$$

Axial strain $\varepsilon_{11} = \varepsilon_a$, and hoop strain $\varepsilon_{22} = \varepsilon_h$ are measured from axial and radial extensometers on the tubular specimen. Principal stresses σ_{11} and σ_{22} are obtained by solving equations (2.21a and 2.21b).

2.2.1.5 Biaxial proportional loading

Principal axial and hoop stresses obtained under various biaxiality ratios are plotted in Fig 2.4. The lines shown for various biaxial strain ratios λ are the loading paths. If the loading path is a straight line through the origin the loading is termed proportional loading [7]. Proportional loading provides a constant ratio ω of principal stresses for each particular biaxiality ratio. For shear loading, the ratio ω is constant and equal to -1.

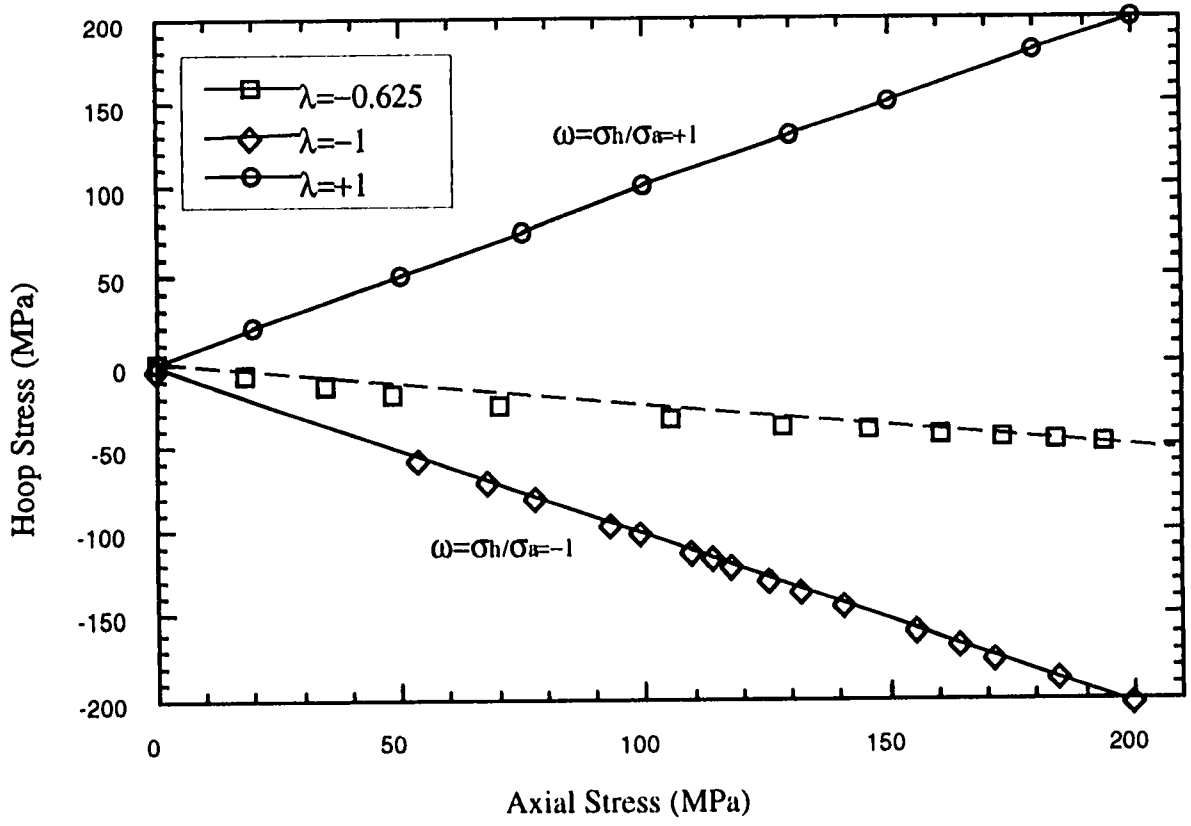

Fig 2.3 Biaxial Proportional loading path for various biaxial principal strain ratios.

For equibiaxial loading, the constant ratio ω is equal to +1. For a biaxial strain ratio of -0.625 the loading path data deviates slightly from linearity but is close to proportional loading. The dashed linear curve in Fig 2.3 represents proportional loading.

2.2.2 Cyclic stress-strain response

Fatigue specimens were cycled between total strain limits. The strain pattern consisted of a set of strain cycles with linearly increasing and decreasing amplitude from zero to a maximum strain of 0.3%. After the stress amplitudes increased (fatigue hardening) to their saturation values, there were no further changes in the hysteresis loop shapes or magnitudes. Fig 2.4 presents typical stabilized hysteresis loops under various biaxiality ratios in SAE 1045 steel.

The curve connecting the tips of such stable hysteresis loops for fatigue tests is called the stabilized cyclic stress-strain curve. The stabilized cyclic stress-strain curve for uniaxial loading is presented in Fig 2.5.

2.3 Elastic-Plastic Strain Analysis

Based on the total theory of deformation, total strain can be decomposed into elastic and plastic strain components. The components of stress were then used to calculate the elastic strain components using the constitutive elastic strain relations.

The plastic strain components were obtained by subtracting the elastic strain components from the total (elastic-plastic) strain.

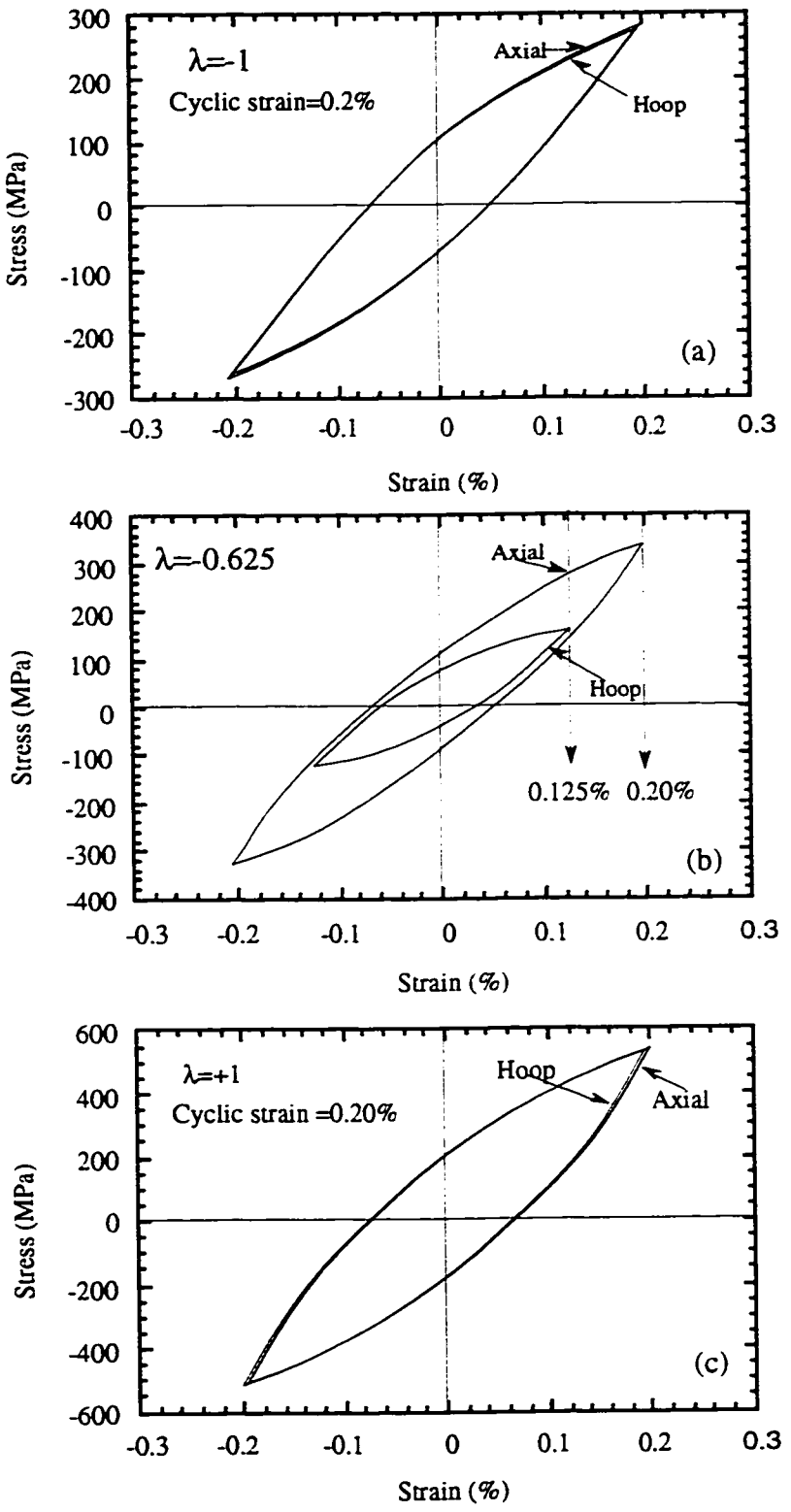

Fig 2.4 Typical strain-stress loops under biaxiality ratios of -1,-0.625, and +1.

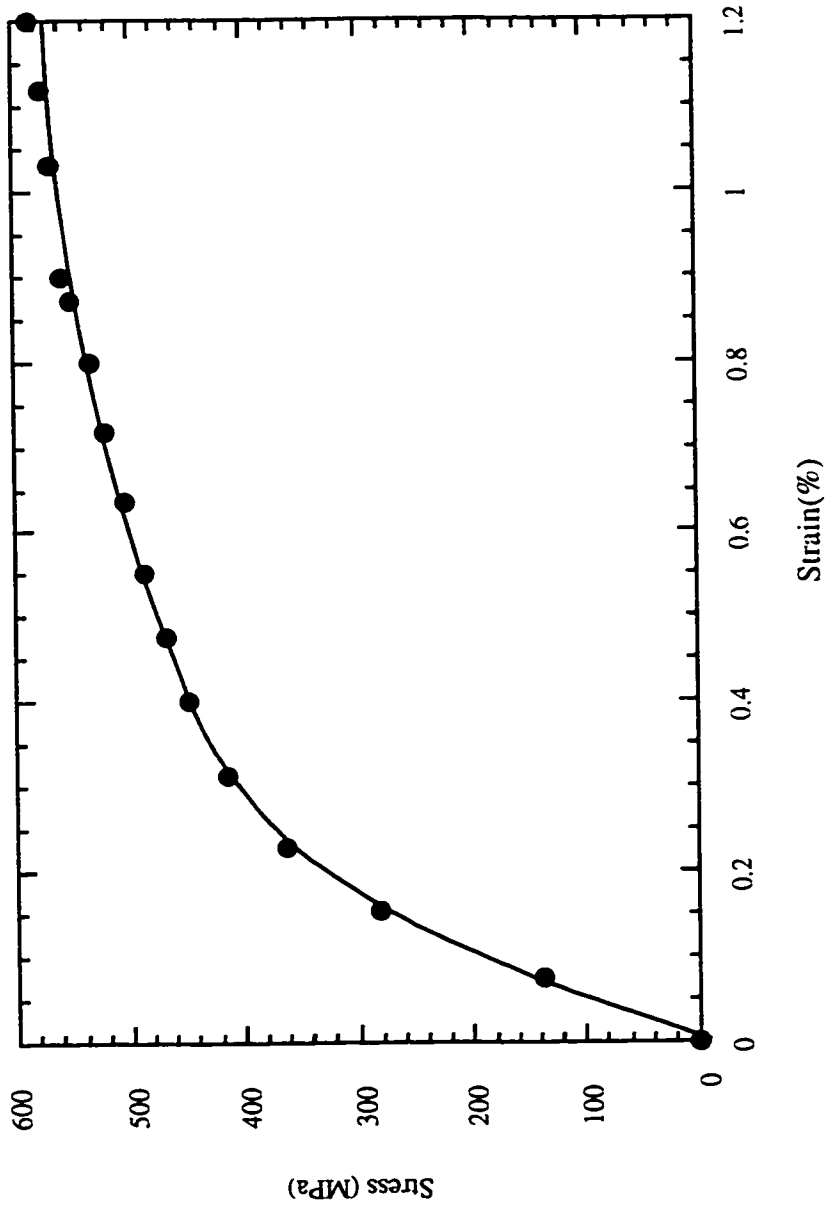

Fig 2.5 Stabilized stress-strain curve for uniaxial loading.

2.3.1 Equivalent plastic strain versus equivalent stress

Equivalent plastic strain and equivalent stress were respectively calculated using

$$\varepsilon_{eq}{}^{p} = \frac{\sqrt{2}}{3}\left[\left(\varepsilon_1{}^{p} - \varepsilon_2{}^{p}\right)^2 + \left(\varepsilon_2{}^{p} - \varepsilon_3{}^{p}\right)^2 + \left(\varepsilon_1{}^{p} - \varepsilon_3{}^{p}\right)^2\right]^{1/2} \qquad (2.22a)$$

and

$$\sigma_{eq} = \frac{\sqrt{2}}{2}\left[\left(\sigma_1 - \sigma_2\right)^2 + \left(\sigma_2 - \sigma_3\right)^2 + \left(\sigma_1 - \sigma_3\right)^2\right]^{1/2} \qquad (2.22b)$$

A linear regression of experimental data for equivalent plastic strain and equivalent stress gave

$$\varepsilon_{eq}{}^{p} = 2.63 * 10^{-9}\ (\sigma_{eq})^{2.8} \qquad (2.16)$$

Fig 2.6 presents the equivalent plastic strain plotted against the equivalent stress in logarithmic scales for the various biaxiality ratios examined.

2.3.2 Normal strain-normal stress and shear strain-shear stress components on the critical plane

Normal strain components are calculated from the largest Mohr's circle for strain (see Fig 2.2)

For the elastic component

$$\varepsilon_n{}^{e} = \frac{\varepsilon_1{}^{e} + \varepsilon_3{}^{e}}{2} \qquad (2.23a)$$

For the plastic component

$$\varepsilon_n{}^{p} = \frac{\varepsilon_1{}^{p} + \varepsilon_3{}^{p}}{2} \qquad (2.23b)$$

The total normal strain is

$$\varepsilon_n{}^{t} = \frac{\varepsilon_1{}^{e} + \varepsilon_3{}^{e}}{2} + \frac{\varepsilon_1{}^{p} + \varepsilon_3{}^{p}}{2} \qquad (2.23c)$$

Similarly, the maximum shear strain components are calculated from the largest strain Mohr's circle as

$$\gamma_{max} = (\varepsilon_1^{\,e} - \varepsilon_3^{\,e}) + (\varepsilon_1^{\,p} - \varepsilon_3^{\,p}) \tag{2.24}$$

Normal stress and maximum shear stress components are calculated from the largest stress Mohr's circle as

$$\sigma_n = \frac{\sigma_1 + \sigma_3}{2} \tag{2.25a}$$

and

$$\tau_{max} = \frac{\sigma_1 - \sigma_3}{2} \tag{2.25b}$$

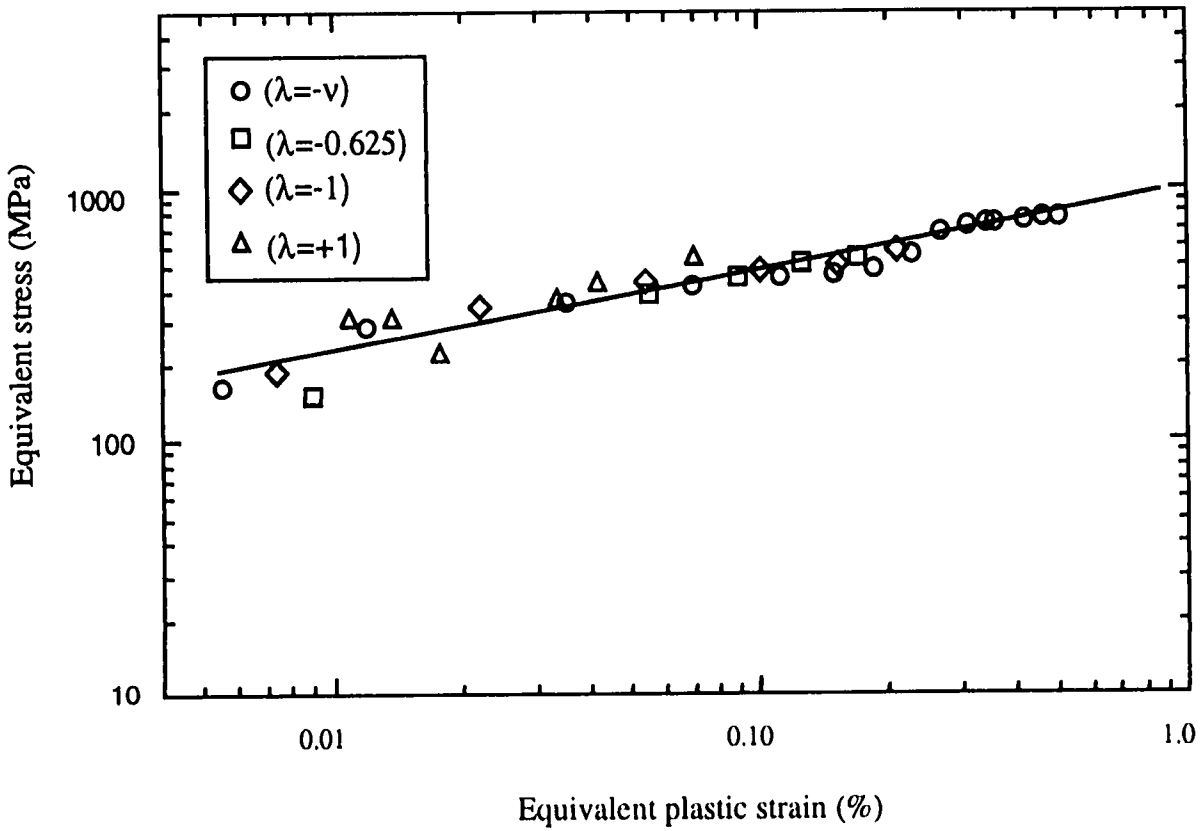

Fig 2.6 Equivalent plastic strain versus the equivalent stress data for various biaxial strain ratios.

CHAPTER 3

Experimental Procedures and Techniques

3.1 Material and Properties

The material examined in this investigation was a SAE 1045 Steel in the form of 2.5 in diameter bar stock with the following chemical composition (Wt %): 0.46 C, 0.17 Si, 0.81 Mn, 0.027 P, 0.023 S, and the remainder Fe. This material is a medium carbon heat treatable steel which is widely used in the automotive industry. The microstructure of the SAE 1045 steel after final polishing showed pearlitic-ferritic features containing up to 30 μm long sulfide inclusions in the rolling direction.

The modulus of elasticity is 206 GPa, the ultimate tensile stress is 745 MPa, the fracture stress is 1047 MPa, the hardness of the material is 200 HB, the cyclic yield stress is 448 MPa (0.2% strain), the uniaxial fatigue limit (stress ratio of R=-1) is 300 MPa and the shear strain amplitude at a fatigue life of 10^7 cycles (R=-1) is 0.27%.

3.2 Specimen Design and Preparation

Cylindrical and tubular specimens with the geometry and dimensions given in Fig 3.1 were used respectively for uniaxial and biaxial fatigue tests. The specimens were machined from a 2.5 in diameter bar with the axial loading axis parallel to the direction of extrusion. After machining, the specimens were mechanically polished using emery cloth of grit 240 and 400. A pneumatic grinder was then used with the finer emery cloth (grit

600). Polishing was done with a paste of 5 μm alumina particles, then diamond pastes of 1 μm and 0.25 μm particles. An optical microscope with a magnifying power of 30 was used to examine the specimen surface to ensure that all the polishing marks (stress raisers) had been removed.

3.3 Fatigue Test Apparatus

3.3.1 Uniaxial fatigue tests

Uniaxial fatigue tests were performed in axial stress control on an MTS servo-hydraulic test machine with a load-cell capacity of 25000 Lb (111.20 KN).
Uniaxial cylindrical specimens were used for fatigue life tests (Fig 3.1a) while crack growth tests were performed using the flat specimens shown in Fig 3.1b.

3.3.2 Biaxial fatigue tests

Figure 3.2 shows the biaxial facility. A servo-controlled, electro-hydraulic testing system and a computer equipped with Flex software [51] were adapted to perform biaxial cyclic straining tests with different biaxial stress ratios. Independent control of principal strain magnitudes, allowed both in-phase and out-of-phase inelastic biaxial straining at all strain ratios to be investigated. In biaxial fatigue tests, failure was defined by the passage of oil from the inside to the outside of the tubular specimen.

A series of thin-walled tubular specimens (Fig 3.1c) were cyclically strained in the axial direction in the strain frame while pressure was alternately applied to the inside and outside of the specimen during each cycle. The test machine actuator applies the fluctuating axial stress, while the pressure system applies the fluctuating transverse stress via a differential pressure across the specimen wall thickness. Axial and transverse extensometers were attached to the outside and inside of the specimen respectively and

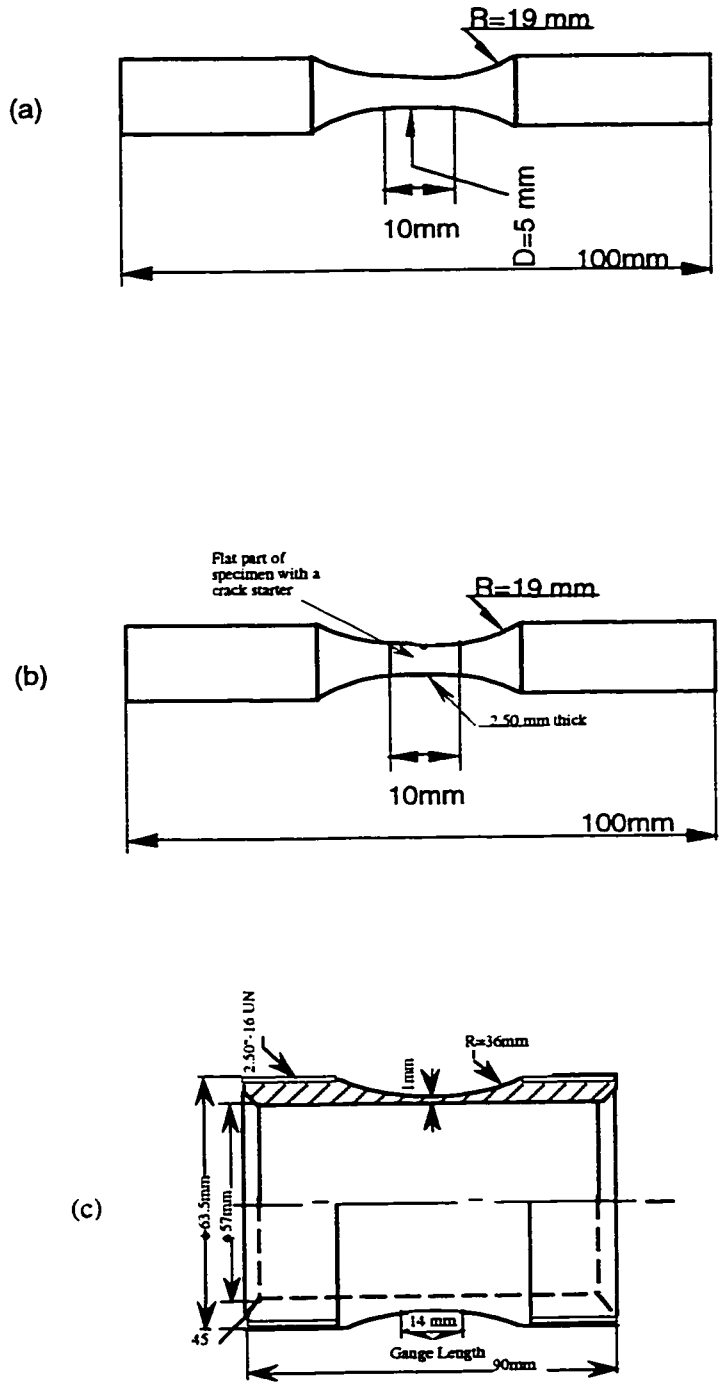

Fig 3.1-a) Uniaxial round specimen b) uniaxial plate specimen, and c) biaxial tubular specimen.

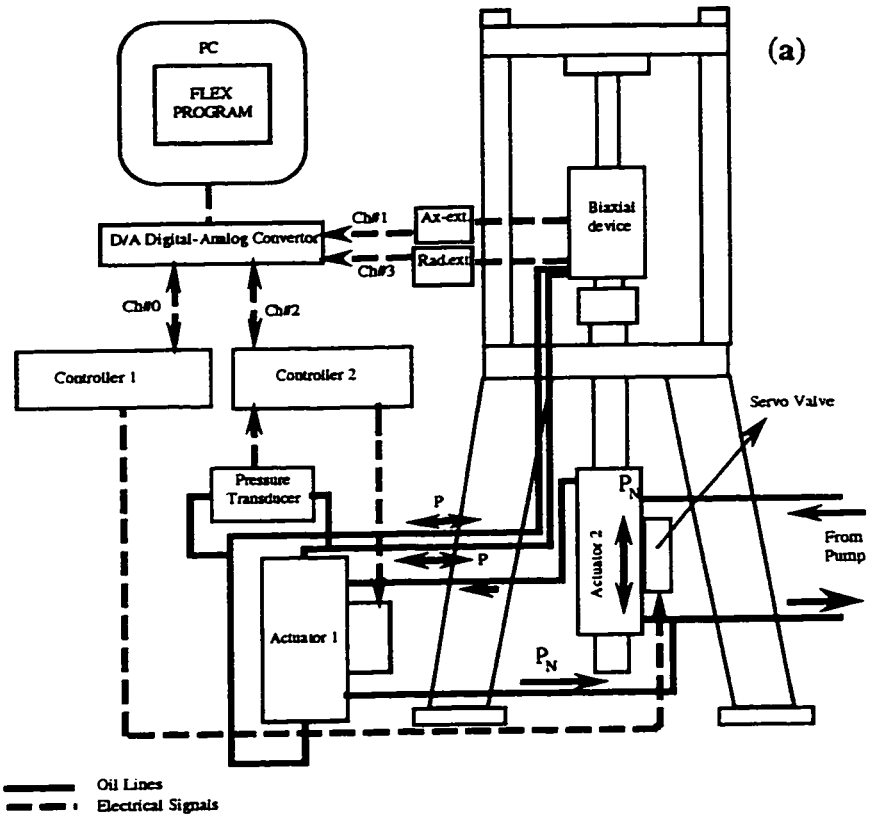

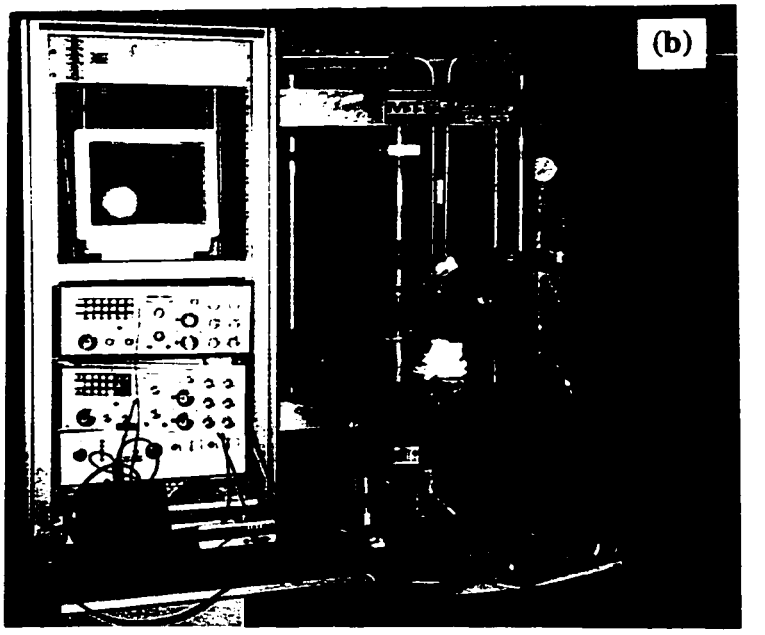

Fig 3.2 Biaxial fatigue system: a) schematic, and b) assembly.

desired biaxial strain ratios λ were achieved using the computer Flex software.

The gripping assembly for the biaxial tubular specimen is shown in Fig 3.3.

3.4 Fatigue Tests

3.4.1 Uniaxial fatigue tests

The crack growth tests under uniaxial constant amplitude loading (CAL) were performed with a stress amplitude of 138 MPa (R=-1). Periodic compressive overload crack growth tests were performed with compressive overloads of -300 MPa, -360 MPa, and -430 MPa followed by numbers of small cycles n equal to 50, 200, 500, and 1000 [48]. Fig 3.4 illustrates the crack growth test load histories for uniaxial constant amplitude loading and a uniaxial load history containing periodic compressive overloads.

Fig 3.5 gives a schematic presentation of the uniaxial constant amplitude loading and periodic compressive overload histories.

Crack growth rates of short fatigue cracks were monitored by measuring the crack length as the number of cycles increased. All crack lengths were measured using an optical microscope and a JAVA system (Jandel Video Analysis Software) with an accuracy of 1μm. Fatigue life tests were performed under strain control for both uniaxial constant amplitude loading and load histories containing periodic overloads. The number of small cycles per block was adjusted to keep the overload damage at about 20% of the total damage.

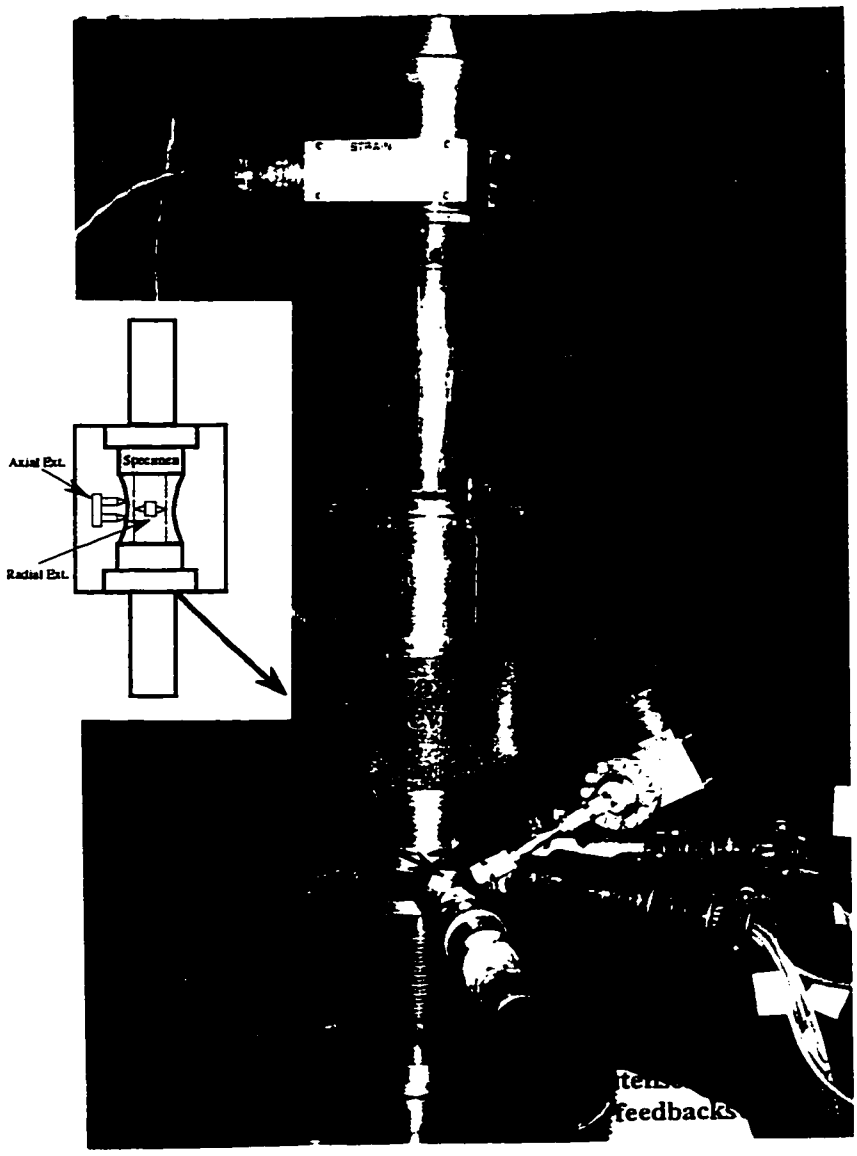

Fig 3.3 Gripping assembly for a biaxial tubular specimen.

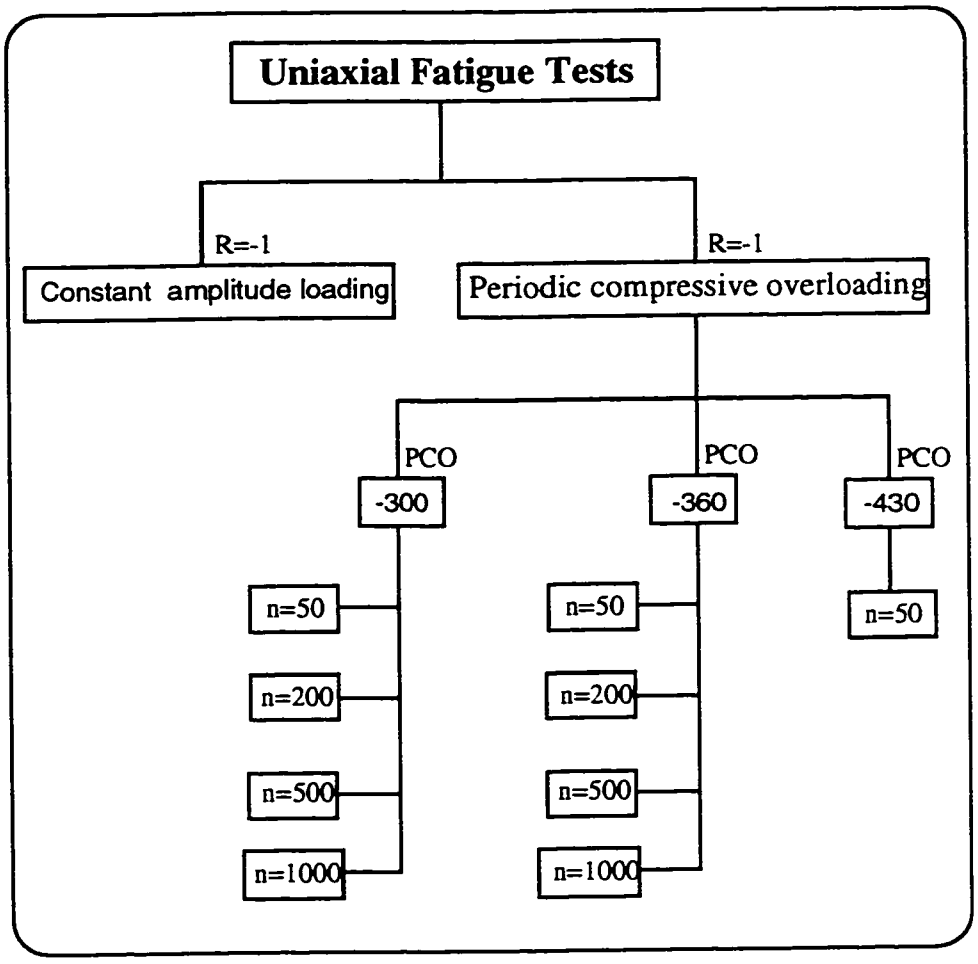

Fig 3.4 Uniaxial fatigue tests under constant amplitude loading and load histories containing periodic compressive overloads.

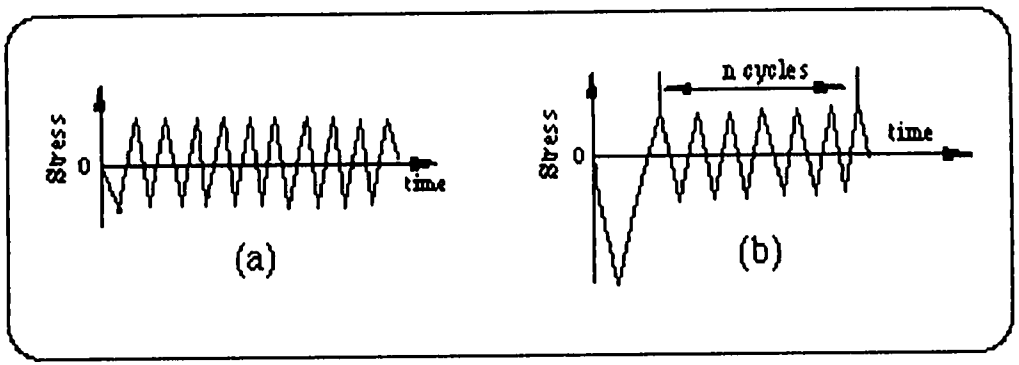

Fig 3.5 Uniaxial crack growth test histories: a) constant amplitude loading, and b) a block load history containing a periodic compressive overload.

Table 3.1 presents the strain histories for uniaxial fatigue life tests under constant amplitude straining and periodic compressive overstraining (PCO).

Table 3.1 Uniaxial fatigue life tests.

Load history	Small cycles ε_{ampl} (%)	No. of cycles between two overloads (n)	λ	Overload strain ε_{pco} (%)
CAL.	±0.50	...	-v	...
CAL	±0.30	...	-v	...
CAL	±0.22	...	-v	...
CAL	±0.19	...	-v	...
CAL	±0.15	...	-v	...
CAL	±0.135	...	-v	...
CAL	±0.133	...	-v	...
Overstrain test	0.20	30	-v	±0.3
Overstrain test	0.13	60	-v	±0.3
Overstrain test	0.10	50	-v	±0.3
Overstrain test	0.08	280	-v	±0.3
Overstrain test	0.07	600	-v	±0.3
Overstrain test	0.052	4000	-v	±0.3
Overstrain test	0.04	600	-v	±0.3

Figs 3.6a-b illustrate the constant amplitude uniaxial strain history (CAL) and the uniaxial block loading history containing periodic compressive overstrains (PCO). Table 3.1 presents the strain histories for uniaxial fatigue life tests under constant amplitude straining and periodic compressive overstraining (PCO).

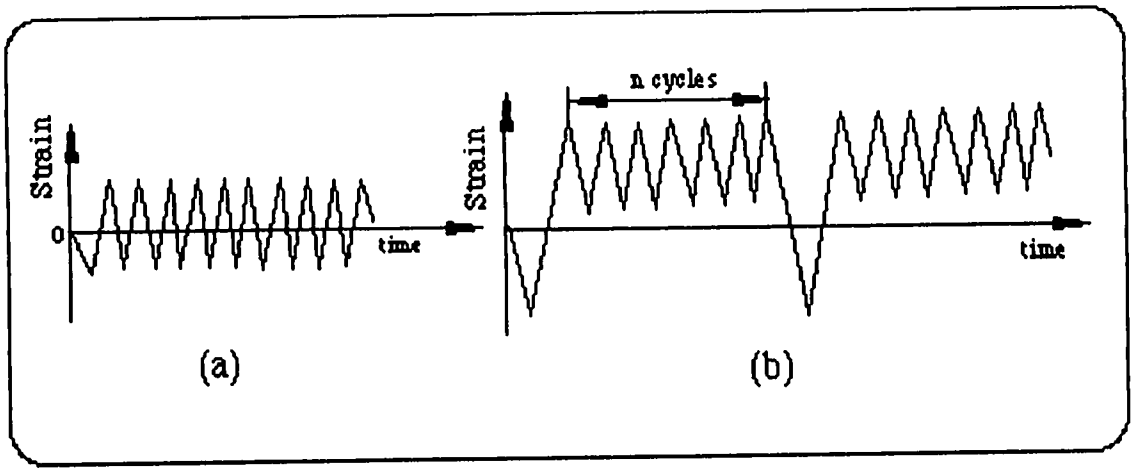

Fig 3.6 Uniaxial fatigue life histories:

a)constant amplitude loading, and b) periodic compressive overload history.

3.4.2 Biaxial (shear) tests

3.4.2.1 Shear loading with an in-phase periodic compressive overstrain

A series of thin-walled tubular specimens were cyclically loaded in the axial direction in the load frame while pressure was alternately applied to the inside and outside of the specimen during each cycle.

Constant amplitude shear tests and shear tests with load histories containing periodic compressive overstrains (PCO) were performed in strain control at a frequency of 0.5 Hz, and zero mean strain (R=-1). The axial strain (ε_a) and transverse (hoop) strain (ε_h) were controlled to provide a 180° out-of-phase biaxial strain ratio of λ=-1 while the overstrain cycles were applied in-phase to produce a stress normal to the crack surface. Figs 3.7a-3.7b present respectively the load histories used for biaxial fatigue tests under constant amplitude loading and the histories having blocks of a periodic compressive overload followed by n small shear cycles. Biaxial (shear) fatigue crack growth and life (λ=-1) tests were performed for the strain histories given in Table 3.2.

3.4.2.2 Shear loading with a 180° out-of-phase periodic compressive overstrain

Constant amplitude biaxial fatigue tests and tests having a constant amplitude biaxial loading followed by 180° out-of-phase periodic compressive overstrains (PCO) were performed in strain control at a frequency of 0.5 Hz, and zero mean stress (R=-1). The axial strain (ε_a) and transverse (hoop) strain (ε_h) were controlled to provide a 180° out-of-phase biaxial strain ratio of λ=-1.

Table 3.2 Shear fatigue crack growth and life histories.

Load history	Small cycles ε_a or ε_h (%)	γ_{ampl} (%)	n small cycles	R	$\lambda=\varepsilon_h/\varepsilon_a$	ε_{pco} (%)
CAL.	±0.08	0.16	...	-1	-1	...
CAL.	±0.10	0.20	...	-1	-1	...
CAL.	±0.15	0.30	...	-1	-1	...
CAL.	±0.20	0.40	...	-1	-1	...
CAL	±0.30	0.60	...	-1	-1	...
CAL	±0.50	1.0	...	-1	-1	...
PCO	±0.08	0.16	600	-1	-1	-0.3
PCO	±0.10	0.20	199	-1	-1	-0.3
PCO	±0.15	0.30	19	-1	-1	-0.3
PCO	±0.29	0.58	10	-1	-1	-0.3
CAL*	(-0.3)-(0.08)	...	...	-3.75	+1	...
CAL*	(-0.3)-(0.10)	...	...	-3	+1	...
CAL*	(-0.3)-(0.15)	...	...	-2	+1	...
CAL*	(-0.3)-(0.29)	...	...	-1.03	+1	...

*- The first value is the minimum strain and the second value is the maximum strain. These are fatigue tests used to evaluate the fatigue life for continuous application of overstrain cycles. They are used to calculate the damage due to overstrain cycles in PCO tests.

The number of small cycles per block was adjusted to keep the overload damage at about 20% of the total damage.

Fig 3.7c presents the load histories used for biaxial shear fatigue tests under strain histories having blocks of 180° out-of-phase periodic compressive overload followed by n small cycles.

Biaxial (shear) fatigue life and growth (λ=-1) tests were performed for different load histories which are tabulated in Table 3.3.

Table 3.3. Shear loading with the 180° out-of-phase periodic compressive overstrains.

Load history	Small cycles ε_a or ε_h (%)	γ_{ampl} (%)	n small cycles	R	$\lambda=\varepsilon_h/\varepsilon_a$	ε_{pco} (%)
PCO	0.08	0.16	600	-1	-1	-0.3
PCO	0.10	0.20	199	-1	-1	-0.3
PCO	0.15	0.30	19	-1	-1	-0.3
PCO	0.29	0.58	10	-1	-1	-0.3

Biaxial shear fatigue life and crack growth tests were also performed with the same magnitude of i) in-phase and ii) 180° out-of-phase periodic compressive overstrains at various small strain amplitudes. The number of small cycles per block was adjusted to keep the overload damage at about 20% of the total damage.

Shear crack length was measured using an optical microscope at the same interval as depth measurements were performed using the confocal scanning laser microscope.

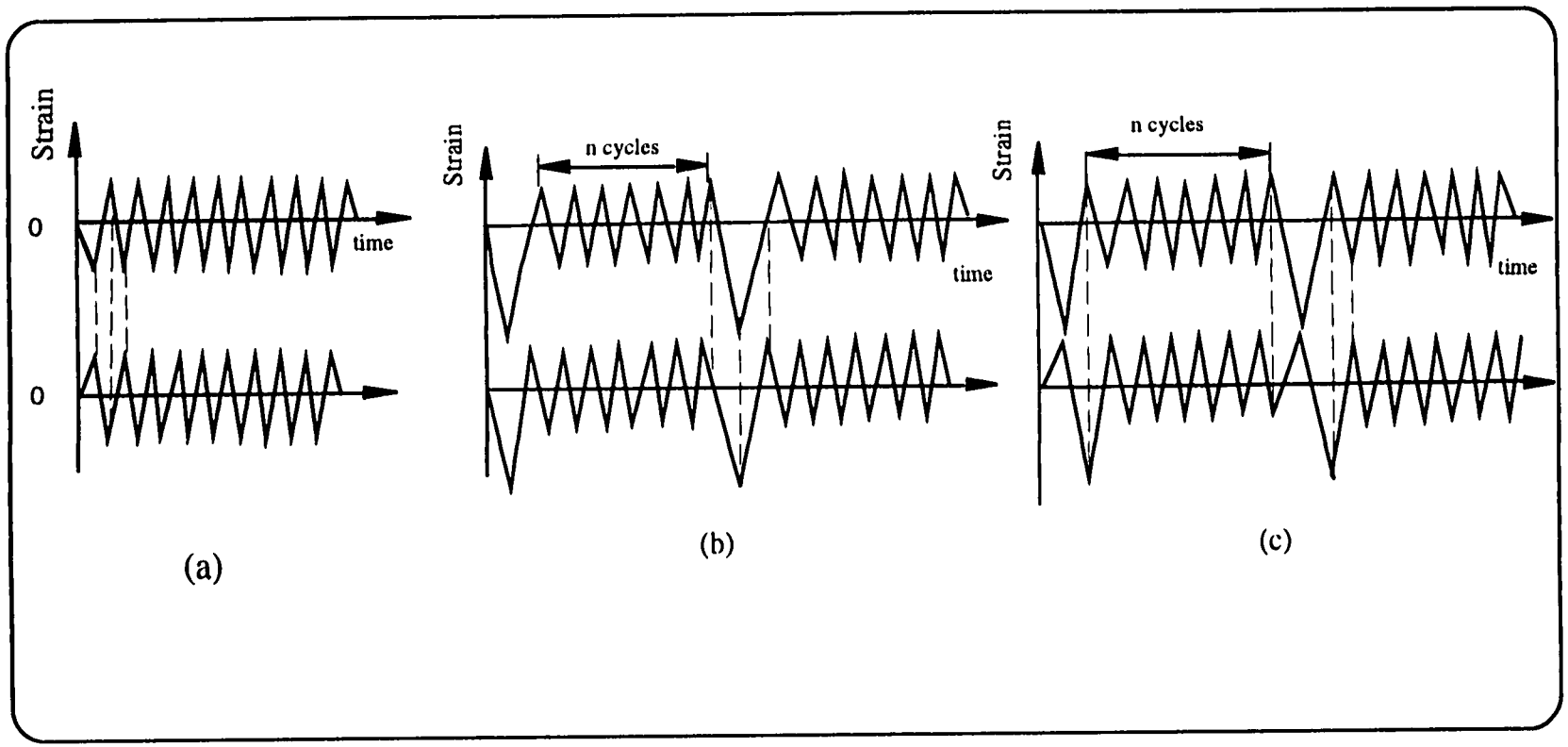

Fig 3.7 Shear fatigue crack growth block histories :

a) Shear constant amplitude straining,

b) in-phase periodic compressive overstrain shear history, and

c) 180 out-of-phase periodic compressive overstrain shear history.

3.4.3 Equibiaxial fatigue (λ=+1) tests

Constant amplitude equibiaxial fatigue tests and equibiaxial tests having a constant amplitude biaxial loading followed by the in-phase periodic compressive overstrains (PCO) of-0.3% were performed in strain control at a frequency of 0.5 Hz. The axial strain (ε_a) and transverse (hoop) strain (ε_h) were controlled to provide an in-phase biaxial strain ratio of λ=+1.

Figure 3.8 presents the load histories used for equibiaxial fatigue tests under constant amplitude loading and for the histories having blocks of a periodic compressive overload followed by n small cycles.

Equibiaxial fatigue life and growth (λ=+1) tests were performed for the load histories which are tabulated in Table 3.4.

Table 3.4 Equibiaxial fatigue Strain histories.

Load history	Range of ε_a or ε_h (%)	n small cycles	R	$\lambda=\varepsilon_h/\varepsilon_a$	ε_{pco} (%)
CAL	0.20	---	-1	+1	---
CAL	0.27	---	-1	+1	---
CAL	0.30	---	-1	+1	---
CAL	0.40	---	-1	+1	---
CAL	0.44	---	-1	+1	---
CAL	1.0	---	-1	+1	---
PCO	0.08	1000	R>0	+1	-0.3
PCO	0.10	300	R>0	+1	-0.3
PCO	0.14	250	R>0	+1	-0.3
PCO	0.20	100	R>0	+1	-0.3

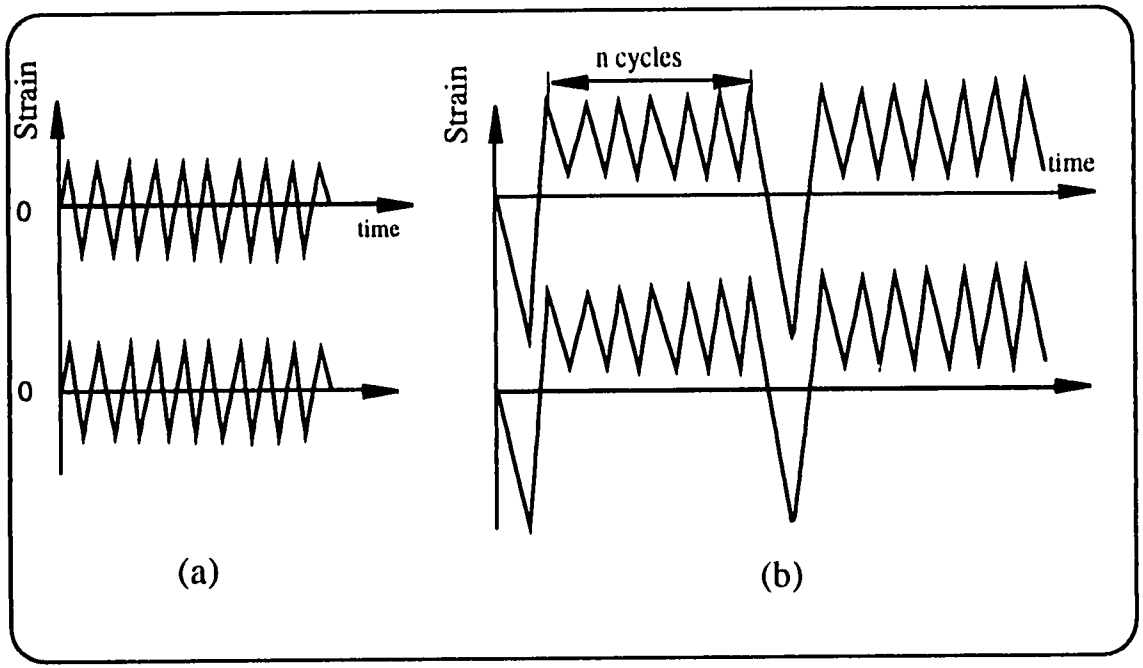

Fig 3.8 Equibiaxial fatigue crack growth block histories:

a) constant amplitude straining and

b) strain histories containing periodic compressive overstrain cycles.

3.4.4 Biaxial fatigue (λ=-0.625) tests

Constant amplitude biaxial fatigue tests with a strain ratio of λ=-0.625 and biaxial tests having a constant amplitude biaxial loading and load histories containing in-phase periodic compressive overstrains (PCO) were performed in strain control at a frequency of 0.5 Hz. The axial strain (ε_a) and transverse (hoop) strain (ε_h) were controlled to provide an in-phase biaxial strain ratio of λ=-0.625. Fig 3.9 presents the strain histories used for biaxial fatigue tests at λ=-0.625 under constant amplitude loading and for the histories having blocks of a periodic compressive overload followed by n small cycles.

Biaxial fatigue life and crack growth at λ=-0.625 tests were performed for the strain histories which are tabulated in Table 3.5.

Table 3.5 Biaxial fatigue strain histories (λ=-0.625).

Load history	Small cycles $\Delta\varepsilon_a$ (%)	Small cycles $\Delta\varepsilon_h$ (%)	n small cycles	R	$\lambda=\varepsilon_h/\varepsilon_a$	ε_{pco} (%)
CAL	0.256	0.16	---	-1	-0.625	---
CAL	0.32	0.20	---	-1	-0.625	---
CAL	0.412	0.26	---	-1	-0.625	---
CAL	0.48	0.30	---	-1	-0.625	---
PCO	0.08	0.05	3500	R>0	0.625	---
PCO	0.12	0.07	1000	R>0	0.625	---
PCO	0.16	0.10	500	R>0	0.625	-0.3
PCO	0.24	0.15	300	R>0	0.625	-0.3
PCO	0.29	0.18	200	R>0	0.625	-0.3
PCO	0.25	0.22	70	R>0	0.625	-0.3

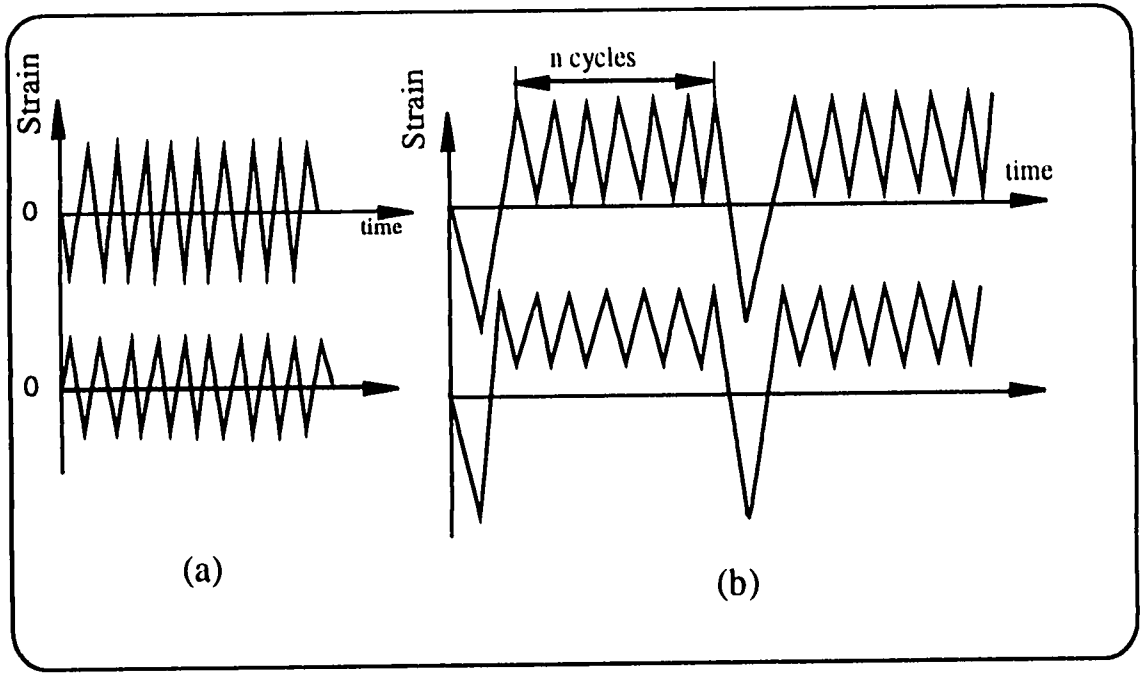

Fig 3.9 Biaxial fatigue (λ=–0.625) crack growth block histories:

a) constant amplitude straining and

b) strain histories containing periodic compressive overstrain cycles.

3.5 Crack Measurement Techniques

3.5.1 Crack depth measurement technique

3.5.1.1 Confocal scanning laser microscopy (CSLM) technique

Fig 3.10 illustrates the reflected-light optical path in a CSLM assembly. Initially, the laser beam passes through a spatial filter, beam expander, and beam splitter and is then deflected by a scanning mirror SM1 rotating about the Z-axis. Lenses L1 and L2 comprise a unitary telescope, which focuses the rasting beam on the centre of a second scanning mirror SM2, rotating about the X-axis. A second unitary telescope, containing lenses L3 and L4 focuses the scanning beam back to the axis at the entrance pupil of the objective lens, which in turn focuses the incoming beam on the specimen. Light reflected from this spot is collected by the microscope objective and passes back through the scan system, where it is descanned. The returning beam is partially reflected by the beam splitter into the detection arm of the microscope, where it is focused on a 50 μm diameter pinhole by the detector lens. Light passing through the pinhole is detected by a 28 mm diameter detector which is a photomultiplier tube providing peak spectral sensitivity at a wavelength of 460nm. The detector gain was chosen to prevent saturation of the detector with light and to provide full use of the dynamic range of the frame grabber (0-255 pixels). The scan system is computer controlled to carry out a raster scan of the focused spot across the specimen, and the reflected-light image is collected on a pixel-by-pixel basis as the scan proceeds. Since the pinhole is placed at the focal point of the detector lens (10 cm focal length), only light that forms a parallel beam before entering the detector lens will pass through the pinhole and be detected. Light reflected from specimen planes that are closer to the microscope objective than its focal plane will form a diverging beam that will focus behind the pinhole, so most of that light will strike its edges and will not be detected.

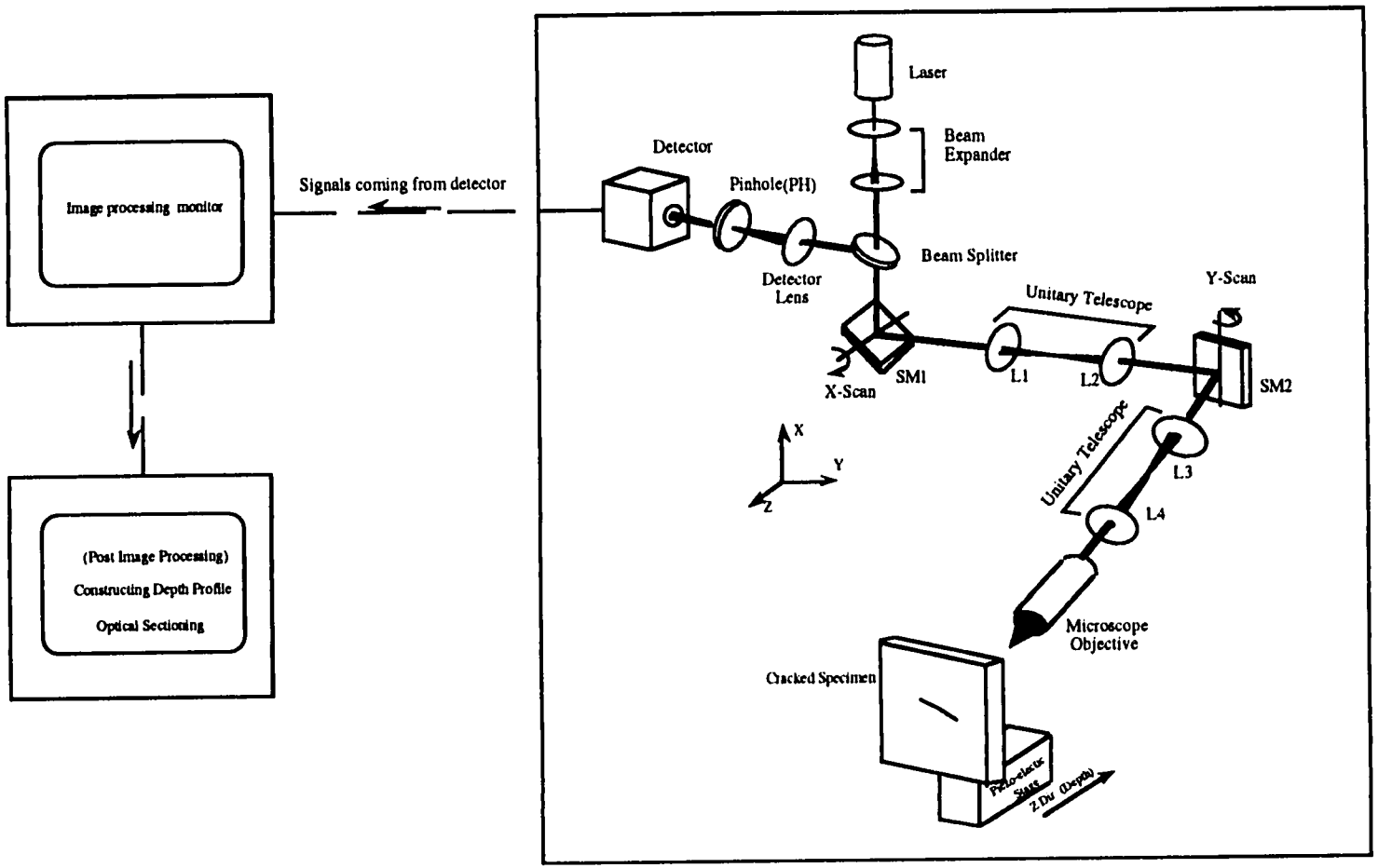

Fig 10 Confocal Scanning Laser Microscopy Technique (CSLM) Assembly.

Similarly, light from any plane in the specimen below the focal plane will be focused in front of the pinhole and will strike its edges as a diverging beam. Thus the pinhole, which is confocal with the focus spot of the laser beam at the specimen, rejects light from above or below the plane of focus in the specimen. It is this action that allows the confocal microscope to perform optical sectioning. This is particularly important when imaging through a scattering medium, because it allows the microscope to detect light reflected from the focal plane, while rejecting light scattered by the medium above the focal plane and it also enables the microscope to measure depth. When reflected light from the focal plane reaches the pinhole, the detector sends a clear image to a monitor. On the other hand reflected light from outside the focal plane does not reach the pinhole and the image produced by the detector is dark.

Using an Argon-Krypton laser beam source (wavelength 488nm), power of 0.25mW and an objective numerical aperture of 0.9, resolutions of 0.25 μm and 0.50 μm in the X-Y plane and depth (Z direction) respectively were obtained. The accuracy of the CSLM system depends on the scanning mirrors (SM1 and SM2) which can be positioned to within ±10μradians. Errors occur due to vibration and mirror instability in this system do not exceed ±(0.25-0.50μm). Lens aberration was minimized by using the double lenses L1/L2 and L3/L4.

3.5.1.1.1 Uniaxial fatigue tests

In the present study, fatigue cracks in uniaxial specimens were initially loaded gradually using a simple tensile machine equipped with a load cell and a load indicator. This opened the fatigue crack. The laser beam was centred on the cracked area by direct observation through the attached optical microscope. The specimen was tilted to the angle which gave the greatest crack depth with respect to the laser beam using a rotating level and

then scanned by the beam. Images from different crack depths at that angle were obtained by changing the specimen height using a piezo-electric monitored stage. Then a laser beam was centered on the crack by direct observation through an attached optical microscope. The specimen was scanned by the laser beam which was then reflected to a detector. Images from different levels of crack depth were obtained by changing the specimen height using a piezo-electric stage. A set of confocal image slices at depth steps of 1μm were acquired. Post image processing was later used to combine all the images. Crack depths at different points along the crack length were measured by taking transverse optical slices of the crack profile. Figure 3.11 illustrates the specimen mounted under CSLM using a tensile machine (tensiometer) equipped with a load-cell and an indicator.

3.5.1.1.2 Biaxial fatigue tests

Using a pressurizing device, specimens, which had experienced biaxial stressing, were internally pressurized to open the crack mouth under a confocal scanning laser microscope (CSLM) system and crack depth opening measurements were done as described for uniaxial tests. The pressurizing device for a biaxial tubular specimen is shown in Fig 3.12. Optical sectioning using post-image-processed crack data provided the crack depth and the crack mouth width at every point along the crack length for each internal pressure. A progressively increasing pressure gave rise to an increase in crack opening displacement and in crack depth. The crack opening stress was taken as the stress level at which the crack depth stopped increasing with increasing applied stress.

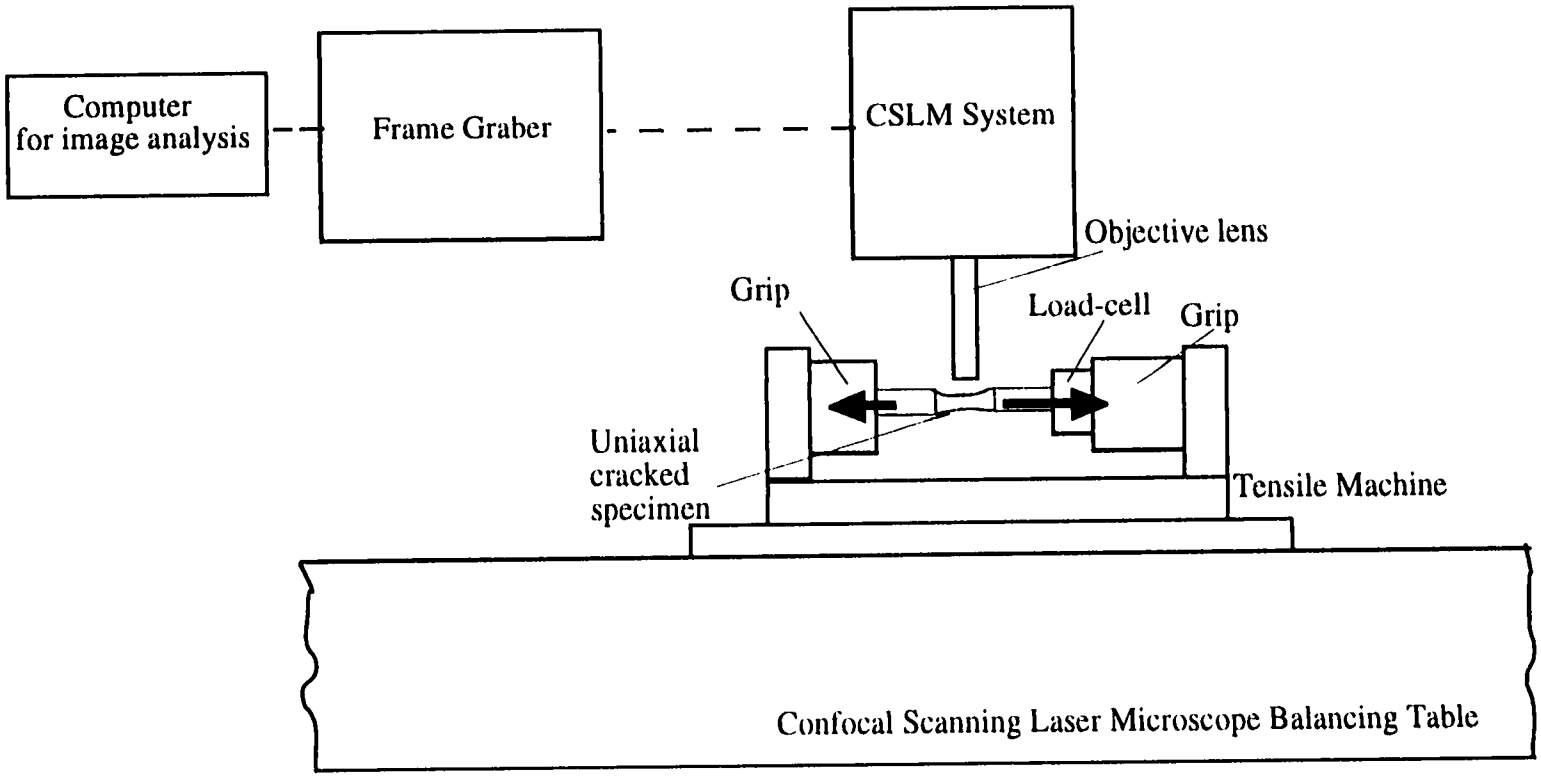

Fig 3.11 Uniaxial fatigue specimen mounted under CSLM using a Tensiometer equipped with a load-cell and computer.

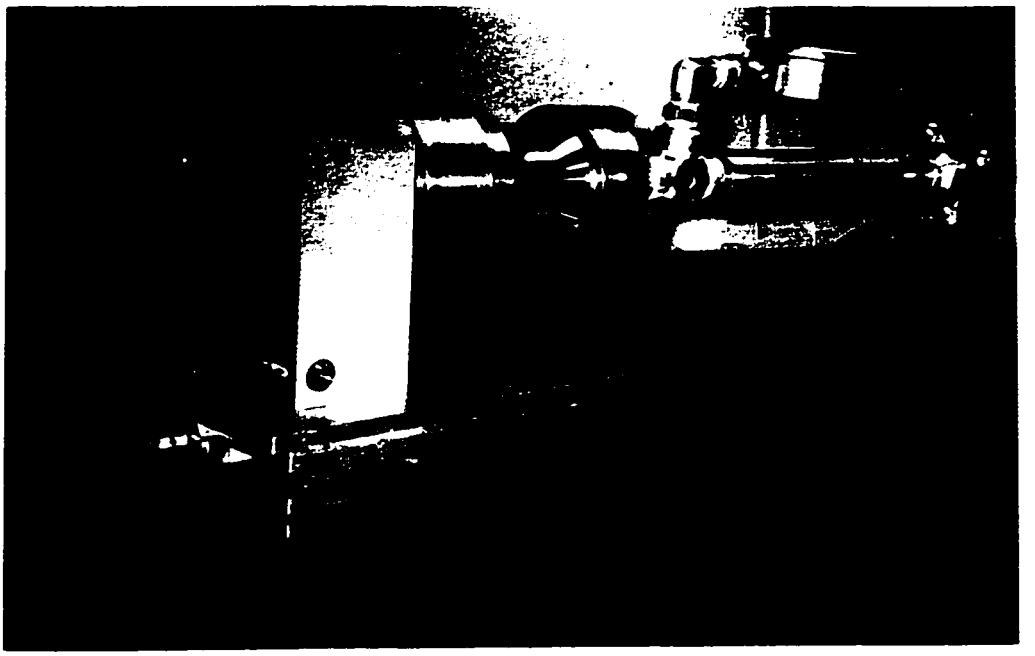

Fig 3.12 The pressurizing device for biaxial tubular specimens.

3.5.2 Crack depth measurements using surface layer removal technique (SLRT)

The crack lengths were first measured and then the edge of specimen was indexed using an optical microscope (as a reference point for measurements). The initial thickness of the specimen was measured using an Olympus type SA105A microscope equipped with fiber optics with an accuracy of 1μm. Metal from the specimen surface was removed by polishing the surface using 0.25μm diamond paste. The specimen was then cleaned with acetone and the new crack length and specimen thickness were recorded. This process was continued until no surface crack could be observed. The difference between the initial specimen thickness and that at which no crack could be detected was taken as the crack depth. During this procedure a slight shift of crack position relative to the marked area indicated that crack growth into the interior of the material occurred on a plane inclined to the surface.

3.6 Fracture Surface Asperity Height Measurements

A fractographic examination of the fracture surface of short fatigue cracks was carried out after breaking the notched 1045 Steel specimens in liquid nitrogen. The fracture surface and the variation in the height of asperities on the fracture surface were observed using a confocal scanning laser microscope. First, the laser beam was centered on the area of the fracture surface adjoining the crack tip by direct observation through an attached optical microscope. The fracture surface of an area of $1mm^2$ at the crack tip was scanned by the laser beam and reflected to the detector. In order to make a three dimensional profile of fracture surface asperities, a piezo-electric stage, was used. The piezo-electic stage controls the distance between specimen and microscope. This provides successive images of level contours of the asperities from their peaks to their valleys. All images were combined to create an image of the configuration of the fracture surface profile. Taking different slices

through this profile and determining an average value of fracture surface asperity height in each slice, revealed that the asperity height is dramatically influenced by the magnitude of the compressive overload.

In this study the fracture surface asperity heights of 30 specimens under both constant amplitude loading and load histories containing periodic compressive overload cycles were measured. The CSLM measurements of the fracture surfaces of small cracks revealed that there was little variation of asperity heights across the fracture surfaces. The maximum variation of asperity height in an area of 600μm × 600μm did not exceed 10%. The fracture surface asperity heights reported in the results section of this study are the average values of asperity height measured on a 600μm × 600μm area of the fracture surface.

3.7 Crack Growth Measurements

3.7.1 Uniaxial fatigue crack growth tests

Crack length and depth for uniaxial loading crack growth tests were obtained as the number of cycles increased using CSLM for Stage I cracks and a 500X optical microscope for Stage II cracks.

Shear crack growth tests under load histories presented in Table 3.2 and Table 3.3, were performed by measuring the crack depth and crack length at intervals of 1000-5000 cycles.

Under both shear loading (λ=-1) and biaxial loading with λ=-0.625, many microcracks initiated and grew into the specimens. In each specimen, about 10 microcracks were marked and the depth and length of these microcracks were measured at 1000-5000 cycle intervals from initiation to failure. The average of the crack growth rates of these ten

microcracks was computed and will be presented in the next chapter. The variation of crack growth rates within the ten microcracks measured in a specimen did not exceed 15%.

Increasing the magnitude of the periodic compressive overload resulted in faster crack growth up to an overload of -430 MPa. Increasing the magnitude of the compressive overload above -430 MPa did not result in further increases in crack growth rate. In this study, the saturation of the crack growth rate at a periodic compressive overload level of -430 MPa was shown by CSLM image processing to correspond to closure free crack growth.

3.7.2 Biaxial shear loading tests

Crack growth rate data were obtained from biaxial specimens subjected to constant amplitude straining and to strain histories containing in-phase periodic compressive overstrains with a peak magnitude of -0.3% after every n small strain cycles.
Crack opening stress measurements and crack depth measurements for biaxial shear fatigue cracks (λ=-1) made using confocal scanning laser microscopy (CSLM) image processing of the crack profile, showed that, for the periodic compressive overloads used, cracks were fully open at zero internal pressure. Therefore, there was no crack face interference. Crack depths used for calculating crack growth rate were taken at the deepest point at the shear crack profile.

3.8 Crack Opening Stress Measurements

3.8.1 Uniaxial tests

Crack opening stresses were measured optically during a load history consisting of a repeated blocks of a large compressive overload followed by constant amplitude small cycles. The small cycles had a positive high R-ratio. A periodic compressive overload magnitude of -430 MPa was applied.

The crack tip region was examined throughout a stress cycle using a 900X microscope at various numbers of small cycles after the compressive overload, and crack opening was recorded. The crack opening measurement procedure under uniaxial loading for 1045 steel specimen was described by MacDougall and Topper [52].

3.8.2 Biaxial tests

Using a pressurizing device attached to the CSLM system, the crack mouth on a tubular specimen was opened and image processing was carried out for a variety of stress levels. Optical sectioning from a post-image-processed crack provided crack depth and crack mouth width at every point along the crack length for each load level. The crack opening stress was taken as the stress level at which the crack depth stopped increasing with increases in applied stress.

Biaxial crack opening stress were also measured using CSLM during strain histories having a periodic compressive overstrain of -0.3% followed by small constant amplitude cycles. For three biaxial strain ratios of -1, -0.625, and +1, crack opening measurements were done for 5, 20 and n/3 cycles after the compressive overloads.

CHAPTER 4

Crack Shape and Crack Growth Results under Uniaxial and Biaxial Fatigue Loading

4.1 Crack Shape and Profile Results using the CSLM Technique

Introduction

The most common methods used to determine the size of small fatigue cracks are optical or scanning electron microscopy of the crack or its replicated surface. Normally, information is provided only about the intersection of the crack with the surface. In some cases, crack depth has been measured by progressively removing surface layers. For example, in their paper on the propagation of short fatigue cracks Wagner et al [53] reported crack depths after successively electropolishing a Ti-8.6 Al alloy. In other instances electrical potential (EP) techniques have been used to study the formation and growth of small cracks. Gangloff [54] continuously monitored crack depth via DC electrical potential measurements, with the calibration model accounting for the shape as well as for variations in the depth of the elliptical surface cracks. The accuracy of crack depth measurement using this technique has been reported to be 0.5-1mm and ±0.15mm in nickel-based alloys [54] and X65 steel [55], respectively. London et al [56] utilized a method that monitored surface acoustic waves to quantify the depth and closure characteristics of microscopic surface fatigue cracks 70 to 250μm deep in AISI 4140 steel compact-tension specimens. Baxter et al [57] reported an electro-chemical method for detecting small fatigue cracks in both steel and aluminum alloys through the identification

of locations where cracks ruptured the oxide film on the surface. These rupture sites were imaged using photoelectron microscopy and fatigue cracks as short as 10μm in length were frequently detected.

This section introduces the technique and results obtained when applying Confocal Scanning Laser Microscopy (CSLM) to determine the crack depth profile of Stage I microstructurally short fatigue cracks. This technique (CSLM) provided quantitative data for fracture surface asperity characteristics, under constant amplitude and periodic compressive overloading conditions, and related them to crack growth rate and crack closure stress for short fatigue cracks in SAE 1045 Steel in the present study. CSLM allowed optical sectioning of the crack and the construction of accurate three dimensional images [58-59].

4.1.1 Optical sectioning for 3D construction of crack using CSLM

Fig 4.1 represents the crack depth corresponding to an optical section along a small crack. The slice shown in this figure correspond to the depth profile at point i along the crack length. These optical slices can be considered to be imaginary planes parallel to the X-Z plane (see Fig.4.1). Every imaginary X-Z plane shows the crack depth profile at a point along the crack length (Y-direction). The difference in height between the peak and the valley in the X-Z plot gives the crack depth at that slice. The peak value in each slice was considered to be the average of peaks at the crack mouth. Using images obtained at the successive static load levels of the pulling/pressurizing device, provided crack mouth displacement measurements in the X-direction.

Fig 4.2 is a plot of the crack shape of several short fatigue cracks showing that the cracks developed an approximately semi-elliptical front. Each datum point on this semi-ellipse corresponds to an optical slice along the crack length obtained from several images at that point.

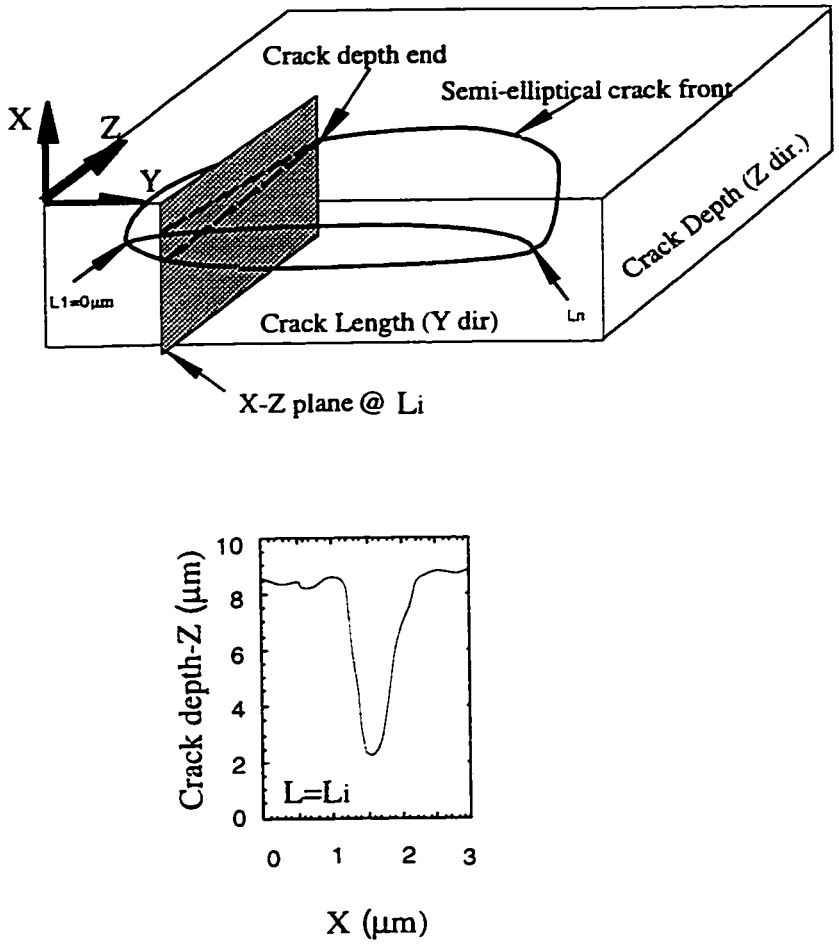

Fig. 4.1 An optical section obtained from the 3D crack profile along the crack length.

4.1.2 Measurements of crack depth along the maximum shear plane and crack opening stress

Crack opening stress and the corresponding maximum depth of shear cracks in the thickness direction were measured. Fatigued tubular specimens were pressurized internally using a hydraulic device in the confocal scanning laser microscope. Hoop and longitudinal stresses due to a progressive increase in the static internal pressure opened the crack along the maximum shear plane and three dimensional images of the crack were acquired.

As the progressively increasing static internal pressure was applied, the crack opened and the crack depth increased with internal pressure until it was fully open. Fig 4.3 shows a family of curves of maximum crack depth versus the hoop stress due to internal pressure.

The crack opening stress was defined as the static hoop stress at which the crack depth reached its maximum value, a_{eff}, (crack fully opened) during a progressive increase in internal pressure. The maxima of the curves (in Fig 4.3) give the crack depths at various numbers of cycles for a 0.3% shear strain amplitude. Each datum in this figure corresponds to the deepest point along the 80 μm crack length, obtained from a set of confocal images, at a given applied pressure. Optical sectioning of post-image-processed crack data provided the crack depth at a series of points along the crack length for each stress level.

The difference between the depth values (a_{eff}-a_0) measured before (when internal pressure is zero) and after the application of a sufficient internal pressure to fully open the crack corresponds to the length of initial physical contact of the crack faces.

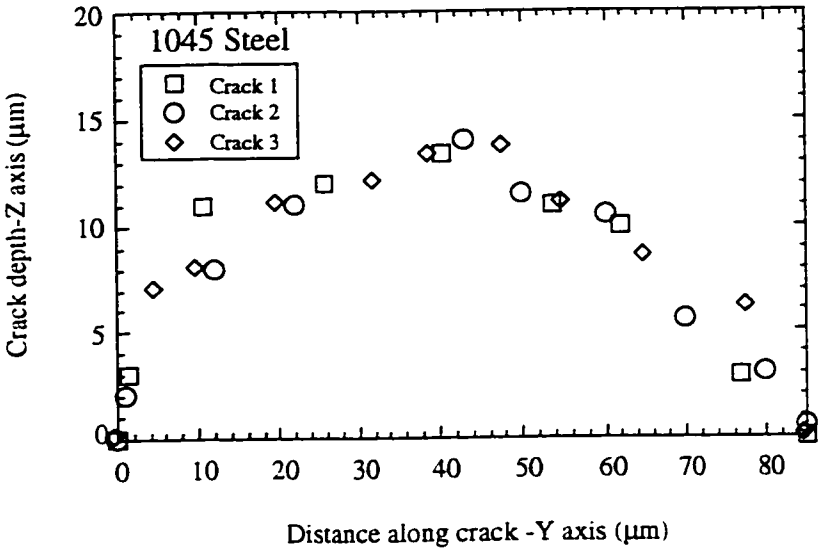

Fig 4.2 Profile of crack depth.

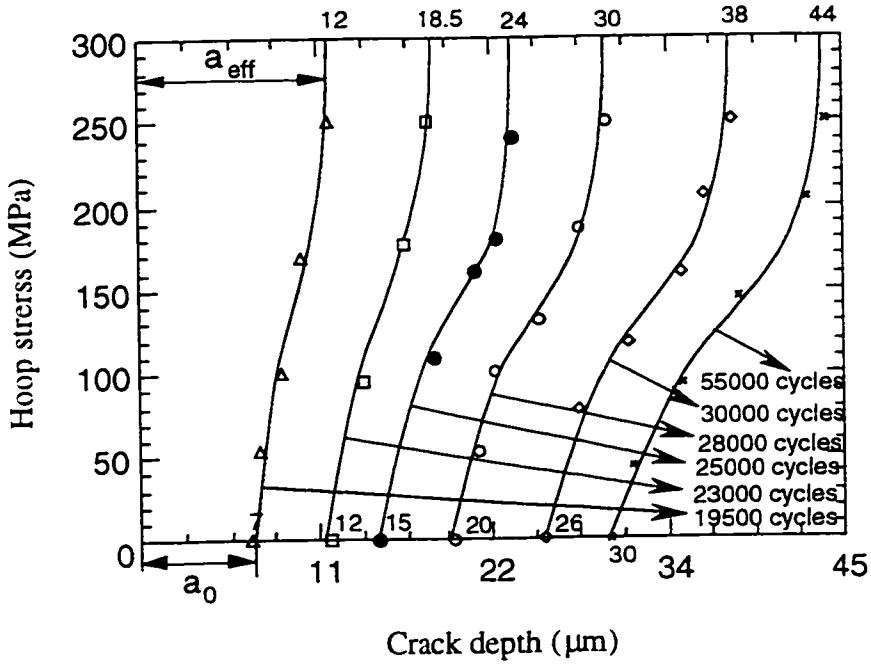

Fig 4.3 Crack depth measurements versus static hoop stress as the number of cycles increases.

4.2 Crack Growth under Constant Amplitude loading

4.2.1 Crack initiation and growth

4.2.1.1 Uniaxial fatigue loading ($\lambda=-\nu$)

Under a uniaxial loading condition, cracks first initiated and grew into the specimen on the maximum shear plane at 45° to the specimen surface (Stage I growth). After growing through one or two grains into the specimen (in the depth direction) in Stage I, the crack plane (in the depth direction) rotated to become normal to the axis of loading (Stage II growth). The plane of crack growth in Stage II was observed from the fracture surface of the specimen after failure. Fig 4.4 illustrates the plane and direction of initial growth of a crack under uniaxial loading.

4.2.1.1.1 Crack aspect ratio and crack depth profile

The ratio of crack depth to half crack length (a/c) was obtained in 1045 Steel for short fatigue crack lengths of the order of 125-250 μm using CSLM. The technique used in this measurement was described extensively in previous chapter. Aspect ratios (a/c) of cracks which experienced fatigue loading just above the fatigue limit stress were found to be approximately 0.8. Using the CSLM technique, the crack depth profile (in Stage I crack growth) was also found to be semi-elliptical in shape.

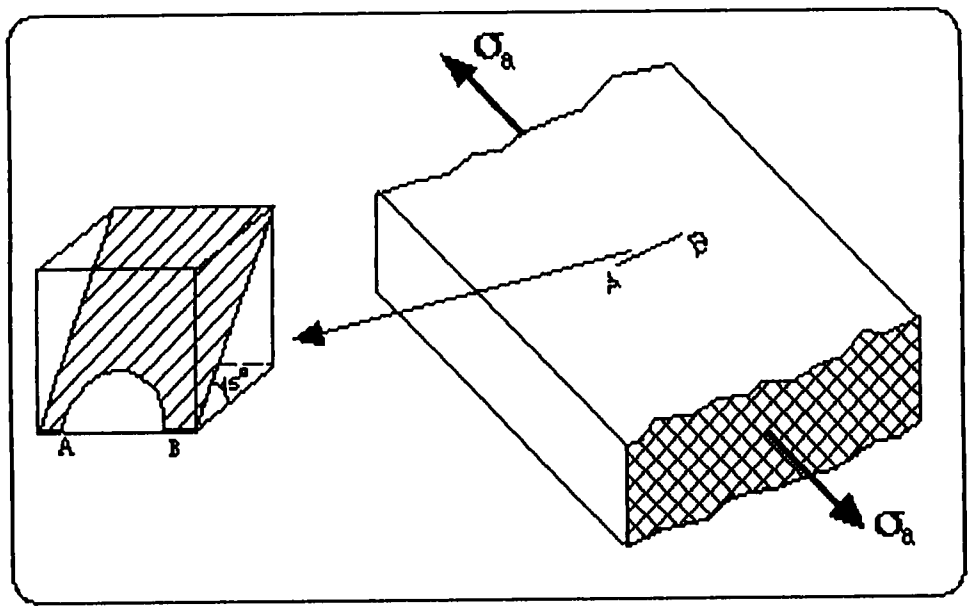

Fig 4.4 Plane of crack initiation and initial growth under uniaxial loading (λ=$-\nu$).

4.2.1.2 Biaxial shear cracks (λ=-1)

In 180° out-of-phase biaxial loading (λ=-1) tests on tubular specimens, shear cracks initially nucleated on an active slip band system which coincided with the maximum shear planes at ±45 degrees to the axial direction of the specimen. Microcracks (shear planes) propagated into the surface of the specimen while their length remained unchanged. Figure 4.5 shows the plane of maximum shear strain and the direction of initial growth of shear cracks. The shear strain (γ) is equal to the difference of axial and hoop strains (ε_a-ε_h).

Microcracks of 3 μm initiated along the plane of maximum cyclic shear strain at fractions of specimen fatigue life (N/N_f) of 0.05, 0.11, 0.095, and 0.09 at shear strain amplitudes of 0.3%, 0.4%, 0.6%, and 1.0%, respectively.

The propagation of microcracks which initiated along slip bands (on the maximum shear plane) can be characterized as R-system crack behavior using the terminology introduced first by Marco and Starkey [60]. In this system, cracks start at many points on a specimen and progress toward the interior of the material (depth direction). The number of microcracks increased as cycling progressed. Once a crack initiated, its surface length did not increase much until the specimen reached about 90% of its fatigue life. However cracks grew into the specimen as the number of cycles increased. For the first 90% of the fatigue life, the microcracks grew along the maximum shear plane in the depth direction while the surface crack length remained nearly unchanged. These microcracks were uniformly distributed on the surface of specimen. At 60%-70% of the fatigue life, linking up of a few microcracks was observed (Fig 4.6a). At 90%-95% of the fatigue life when the shape ratio of crack depth to half crack length reached 1, the microcracks began to grow in the length as well as in the depth direction and began linking up on shear planes (Fig 4.6b).

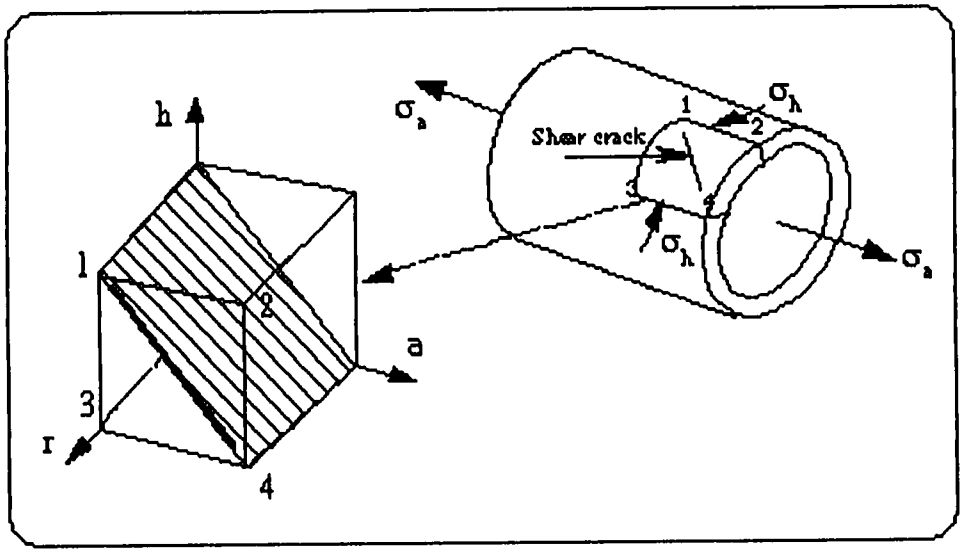

Fig 4.5 Plane of crack initiation and initial growth under shear fatigue straining (λ=−1).

This linking up of microcracks led to failure shortly thereafter (Fig 4.6c). At higher shear strain amplitudes, microcracks appeared to be more open and more distinct than at lower strain amplitudes.

4.2.1.3. Equibiaxial fatigue cracks (λ=+1)

In equibiaxial (in-phase biaxial) fatigue tests on tubular specimens, cracks initiated and grew along the specimen surface on the two maximum shear planes parallel and vertical to the specimen axis and propagated into the specimen on planes at 45° to the specimen axis. Fig 4.7 shows the plane of crack initiation and initial growth of an equibiaxial fatigue crack (λ=+1). About two thirds of the equibiaxial fatigue cracks initiated in the axial direction of tubular specimen. The greater number of cracks in this direction which coincides with the direction of rolling is attributed to elongated sulfide inclusions parallel to the rolling direction. Equibiaxial cracks initiated on the planes of maximum shear strain at fractions of specimen fatigue life (N/ N_f) of 0.074, 0.088, 0.086, 0.083, and 0.085 at biaxial strain amplitudes of 0.10%, 0.135%, 0.15%, 0.22% and 0.30% respectively.

Vertical equibiaxial cracks initiated at several points on the tubular specimen and propagated along and into the specimen. In most tests, failure defined by oil leaking through the specimen thickness occurred when the crack length exceeded 2 mm. Fig 4.8 shows photos of initial growth and failure of equibiaxial fatigue cracks.

4.2.1.4 Fatigue loading under a biaxial strain ratio of λ=-0.625

In 180° out-of-phase biaxial loading (λ=-0.625) tests, on thin-walled tubular smooth specimens, crack initiation and early damage development were observed along planes of maximum shear strain at about 40°-45° to the axial direction of the tubular specimen. Microcracks initiated at various positions in the gage length of the specimen.

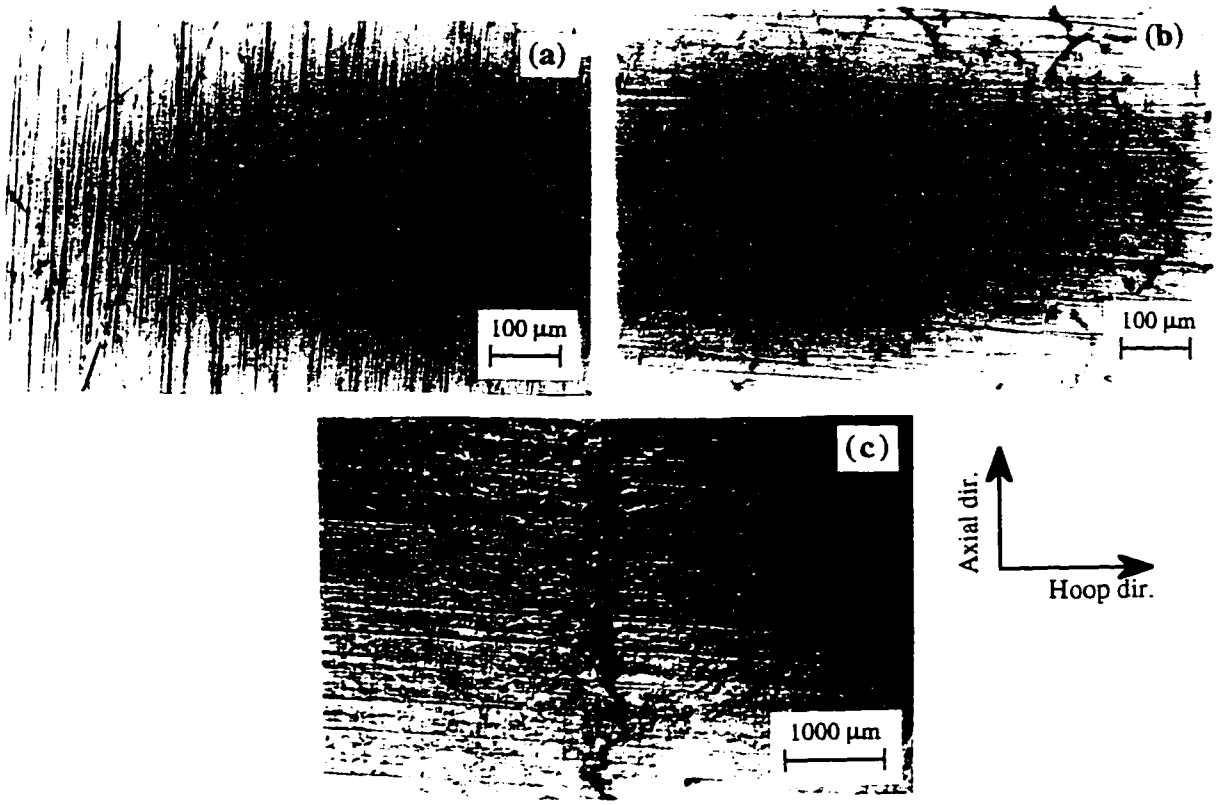

Fig 4.6 Crack growth under shear loading a) linking up of a few shear microcracks at 60-70% of the fatigue life, b) linking up of many shear microcracks at 90-95% of the fatigue life, and c) failure after a rapid linking of shear microcracks.

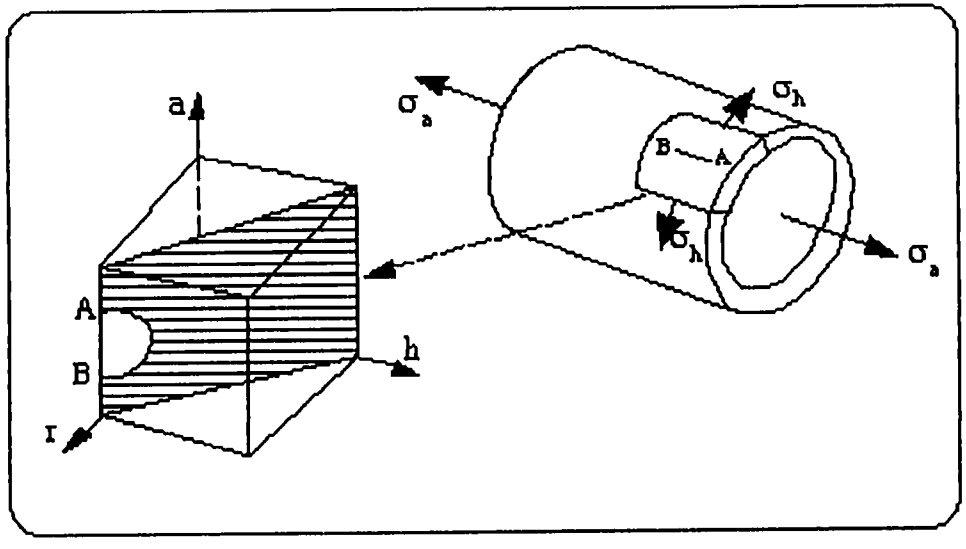

Fig 4.7 Plane of crack initiation and initial growth under equibiaxial loading (λ=+1).

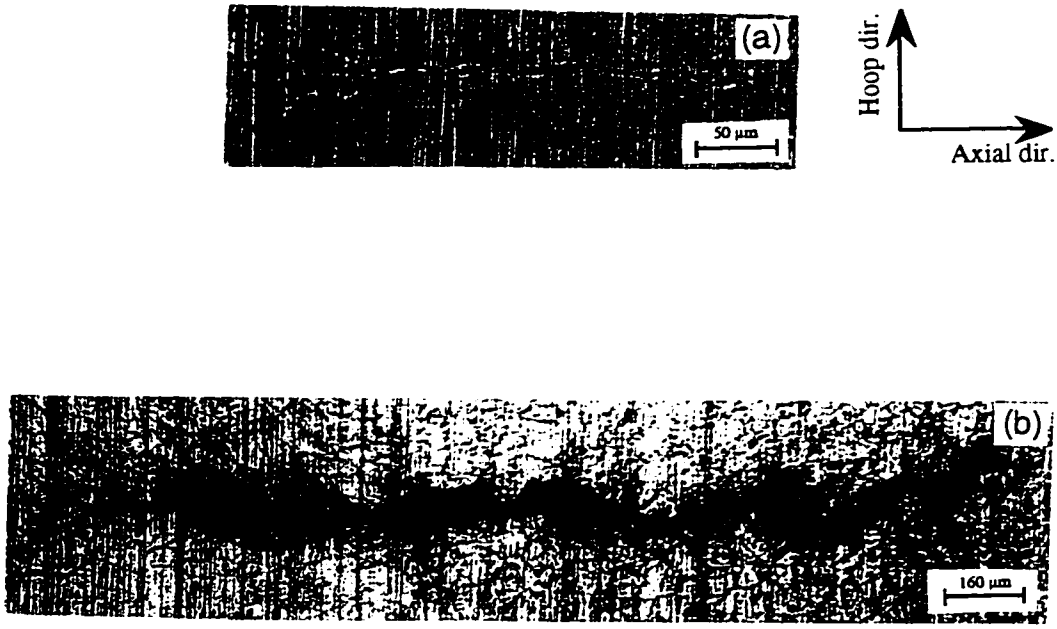

Fig 4.8 Micrographs of a) initial growth and b) failure under equibiaxial fatigue loading.

The behaviour of microcracks for this strain ratio was similar to microcracks initiated under pure shear loading. Initiation of cracks (3 μm) under a biaxial strain ratio of -0.625 occupied a fraction of specimen life (N/N_f) of 0.088, 0.074, 0.078, and 0.068 at axial and hoop strain amplitude pairs of (0.128%, -0.08%), (0.16%, -0.10%), (0.20%, -0.125%), (0.24%, -0.15%), and (0.29%, -0.18%) respectively.

As the number of cycles increased the number of microcracks increased and they became more distinct. At this biaxial strain ratio of -0.625 microcrack initiation and coalescence occupied up to 80% of fatigue life. The growth of microcracks for this strain ratio occurred into the specimen while the length of each individual microcrack on the surface of specimen was nearly unchanged. Fatigue failure occurred by a rapid linking up on microcracks at the end of a test. Typically during failure inclined microcracks linked up in the circumferential direction of a specimen to form a 2.0 mm to 5.0 mm crack.

4.2.2. Biaxial crack growth

4.2.2.1. Biaxial shear cracks (λ=-1)

After a crack initiated it became more distinct as the number of cycles increased, but there was no significant increase in the surface crack length. The crack depth along the initiation plane measured from a defined initiation depth of 3 μm on the slip plane (which coincided with the maximum shear plane) increased. Figure 4.9 gives the crack depth measurements on this plane with number of cycles. The crack growth rate in the depth direction increases and the number of cycles to crack initiation decrease as the magnitude of the shear strain amplitude increases.

The variation of aspect ratio (a/c) with crack depth for different shear strain amplitudes as the shear microcracks grew in the depth direction, with almost no increase in surface crack length (up to 90% of fatigue life), is given in Fig 4.10.

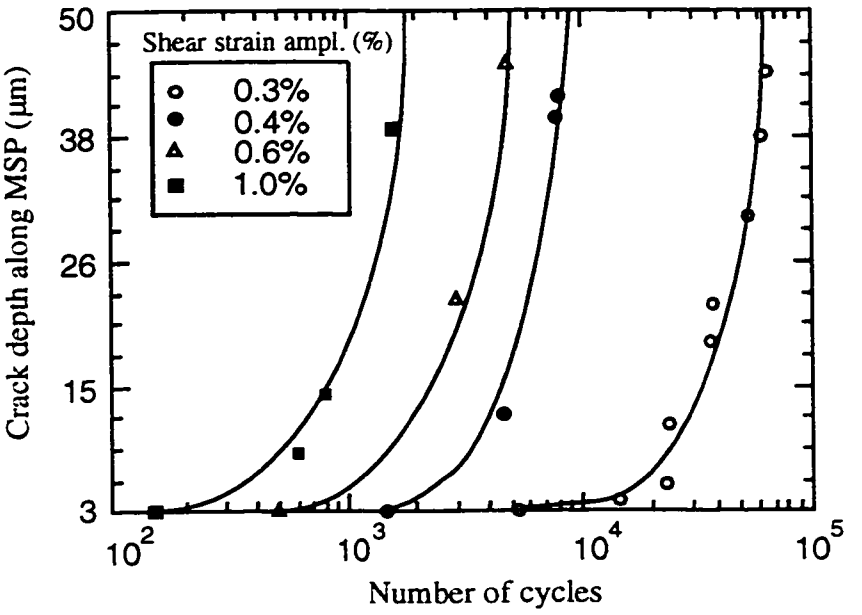

Fig 4.9 Crack growth results along the crack plane as the number of cycles changes.

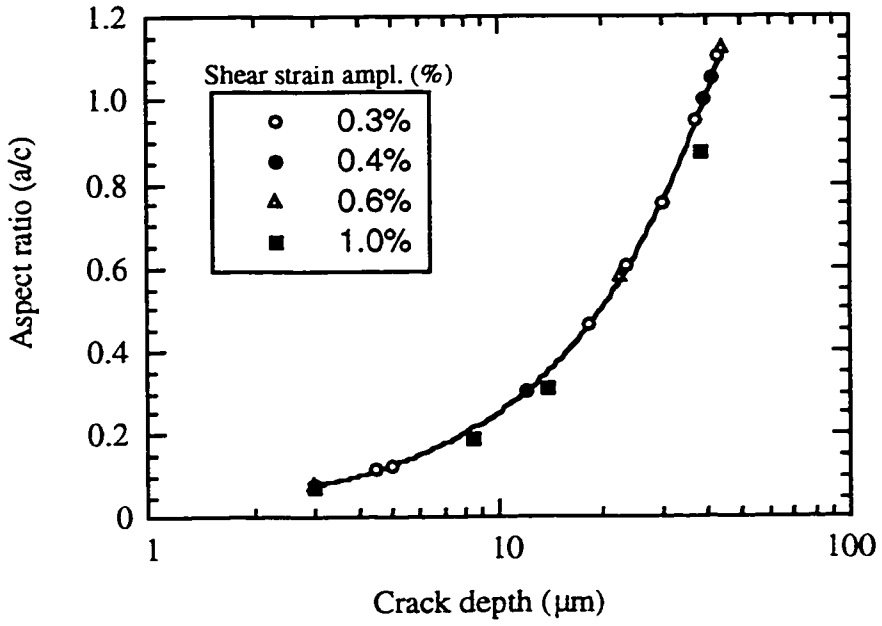

Fig 4.10 Crack aspect ratio versus the crack depth

It was found that at about 90% of the fatigue life the aspect ratio a/c reached unity (semi-circular), and the shear cracks started growing in the length direction as well as into the material. The propagation of microcracks along the plane of crack initiation occupied 90-95% of the fatigue life. This portion of life was followed by a rapid linking of microcracks leading to failure. Figure 4.11 shows crack depth versus cycles data for constant amplitude tests of the tubular 1045 steel specimen under shear loading from initiation to failure. The solid part of the curves corresponds to crack growth on the plane of maximum shear strain and the dashed part of the curves corresponds to the period of rapid linking up of microcracks (shear planes) at the end of a test.

4.2.2.2 Equibiaxial fatigue cracks (λ=+1)

The growth mechanism of cracks created under in-phase biaxial fatigue loading (λ=+1) is different from that for 180° out-of-phase biaxial fatigue loading (λ=-1). In equibiaxial fatigue loading, once a crack initiated (3 μm in depth), its surface length and depth increased as the number of cycles increased. Failure occurred when the surface single crack length exceeded 2 mm. For this strain ratio no microcrack formation and coalescence were observed. Fig 4.12 presents the crack depth measurement results on the plane of maximum shear strain as the number of cycles increase. These results show that as the magnitude of the strain amplitude increases, cracks grow faster into the specimen surface. The variation of aspect ratio (a/c) with crack depth for equibiaxial fatigue cracks (λ=+1) is given in Fig 4.13. In biaxial shear loading (λ=-1), the initiation and initial growth of cracks on planes of maximum shear strain occupied up to 90% of the fatigue life, and then failure occurred by a rapid linking of cracks on shear planes (see Fig 4.14a). However, in equibiaxial fatigue loading (λ=+1), once a crack initiated, it grew in the length and depth directions until failure took place (see Fig 4.14b).

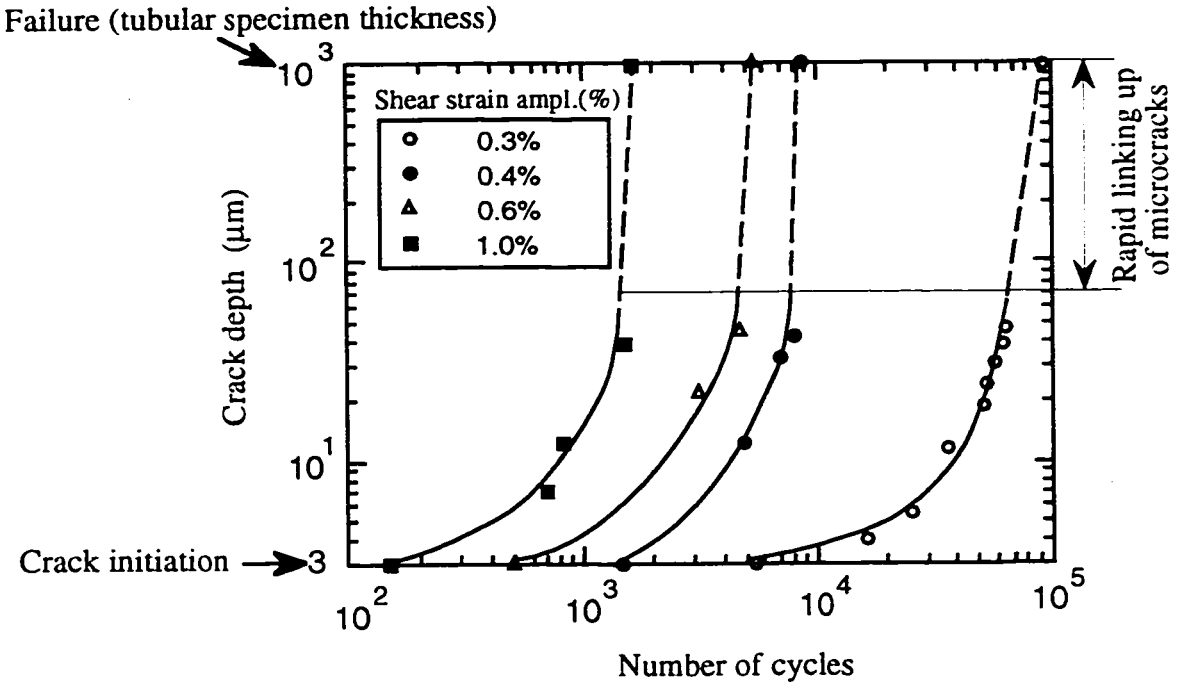

Fig 4.11 Shear crack growth results from initiation to failure.

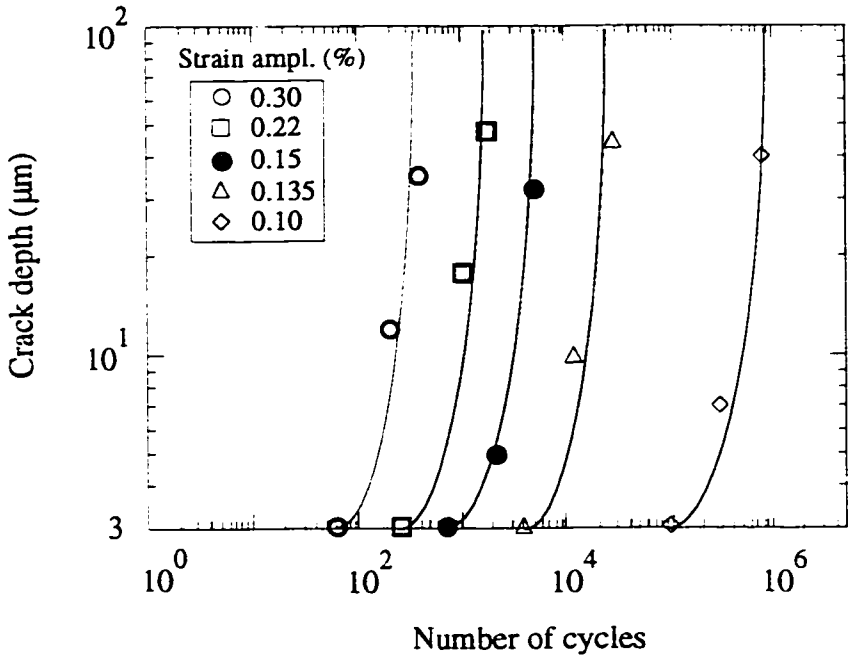

Fig 4.12 Early crack growth results under equibiaxial CAL fatigue loading.

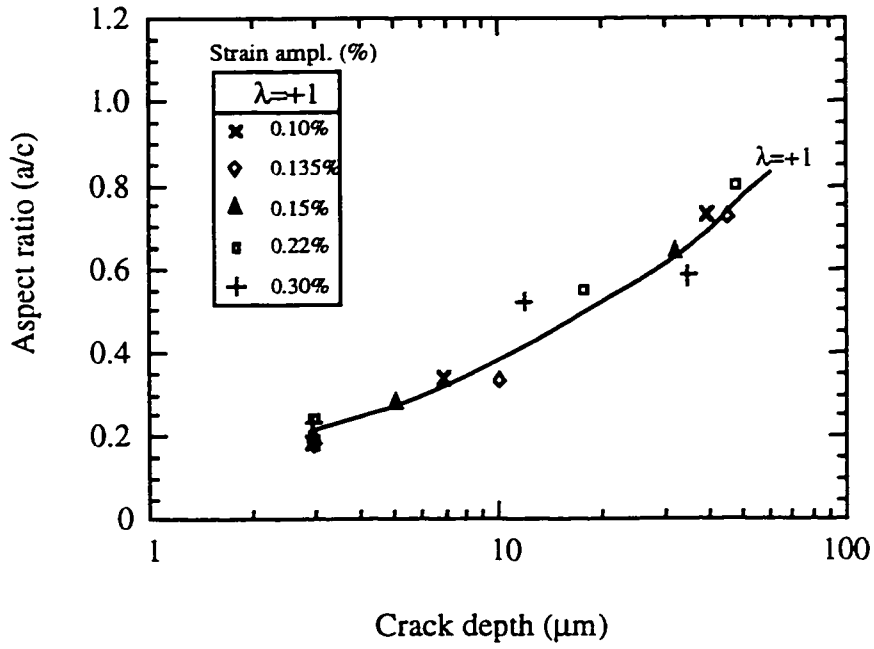

Fig 4.13 Crack aspect ratio versus the crack depth for λ=+1.

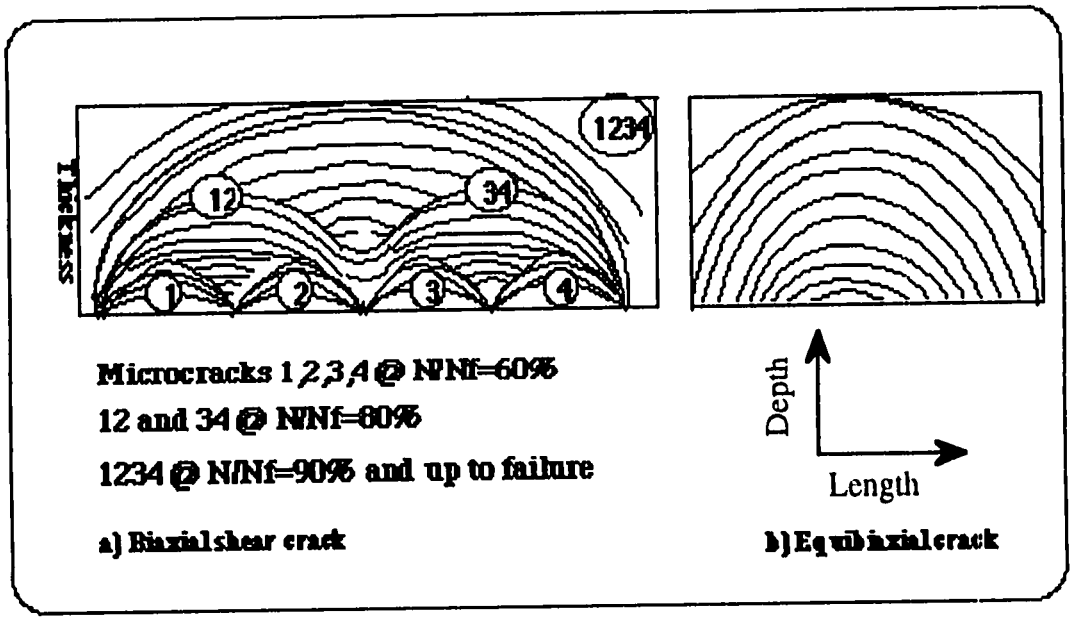

Fig 4.14 Schematic presentation of biaxial fatigue crack growth mechanism:

a) biaxial shear cracks, and

b) equibiaxial fatigue crack.

4.3 Biaxial Crack Growth under Periodic Compressive Overstrain Histories

Introduction

Many investigations [41,43,48,61,62] have shown that, for both short and long fatigue cracks, fatigue loading spectra with periodic compressive overloads of near yield stress magnitude have a detrimental effect on both crack initiation and propagation. At near threshold stress intensities, these effects are thought to be due to a flattening of crack tip asperities by the high compressive stress which leads to a reduction in crack closure and an acceleration in crack growth. The results of Topper and Yu [43] showed increased propagation rates and decreased threshold stress intensities with the application of periodic compressive overloads for various metals. Their findings also revealed crack opening stress levels below zero for large compressive overloads. Similarly, Zaiken and Ritchie [63] proposed two mechanisms responsible for the decreased opening stress level: (i) the flattening of fracture surface asperities and (ii) residual stresses ahead of the crack tip.

4.3.1 Uniaxial fatigue loading ($\lambda=-\nu$)

An examination of the growth of short fatigue cracks under uniaxial constant amplitude loading and during load histories having periodic compressive overloads of various magnitudes revealed that the fracture surface near the crack tip and the crack growth rate changed dramatically with the magnitude of the compressive overload. The height of the surface irregularities reduced as the compressive overload increased progressively flattening fracture surface asperities near the crack tip. This resulted in a reduced crack closure stress and a higher crack growth rate.

Confocal Scanning Laser Microscopy (CSLM) image processing of the fracture surface in an area immediately behind the fatigue crack tip was used to measure the height

of asperities for constant amplitude loading and for periodic compressive overloads of -300, -360, and -430 MPa (followed by 50 small fatigue cycles). Asperity height decreased from 28 μm in constant amplitude loading to 18, 13, and 8 μm for -300, -360, and -430 MPa overloads, respectively. A complementary investigation using a Scanning Electron Microscope (SEM) revealed compression-induced abrasion marks. The abrasion marks corresponded to the region close to the crack tip location when the compressive overloads were applied.

The results indicated that the fatigue crack growth rates obtained from a loading spectrum with periodic compressive overloads were always higher than for constant amplitude loading. Fig 4.15 shows crack depth versus number of cycle plots for cracks for various magnitudes of the compressive overloads.

4.3.1.1 Fracture surface roughness

An investigation of the fracture surface of short fatigue cracks using CSLM image processing and SEM systems revealed the height variation of fracture surface asperities along the crack front and through the specimen thickness for different loading conditions. The average height of asperities using CSLM image processing of the fracture surface in an area immediately behind the crack tip for various loading conditions of constant amplitude and periodic compressive overloading was measured.

The height of plastically crushed asperities after the application of compressive overloads was determined for each magnitude of overload. The average height of asperities in notched 1045 steel specimens for constant amplitude loading and for various levels of periodic compressive overloading is plotted versus the compressive overload stress divided by the yield stress in Fig 4.16.

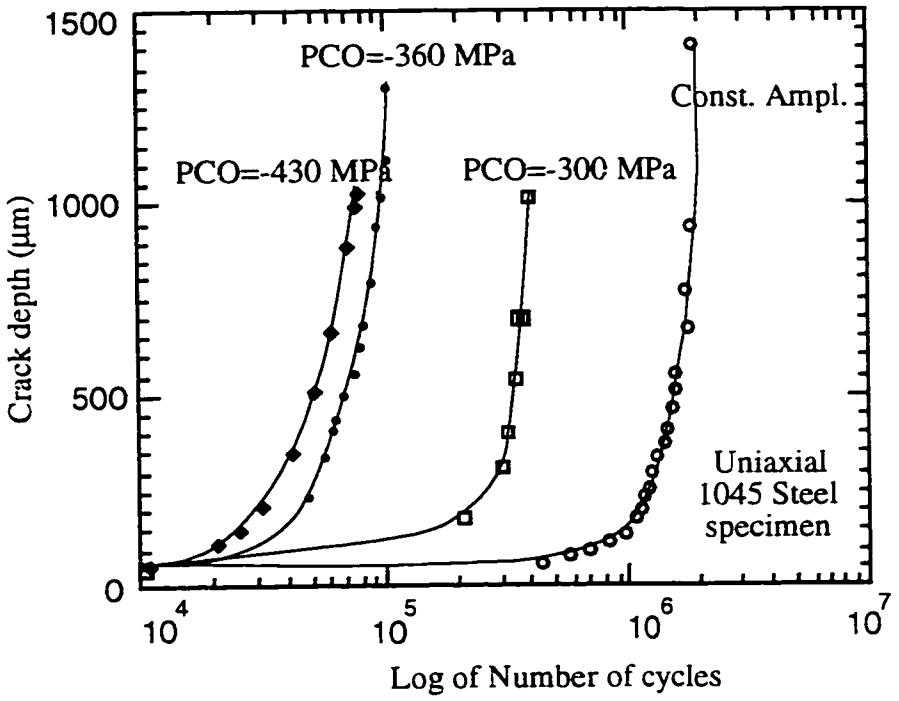

Fig 4.15 Crack growth behavior under constant and periodic compressive overloads of -300, -360, and -430 MPa.

The figure shows a trend of decreasing asperity height as the magnitude of the compressive overload increases (-300, -360, and -430 MPa). The height of fracture surface irregularities near the crack tip decreased (from 28, to 18, 13, and 8 μm, respectively) as compressive overload stresses increased (from constant amplitude loading to -300, -360, and -430 MPa, respectively).

The decrease of height as the magnitude of the compressive overload increases, indicates that compressive overloads flatten fracture surface asperities. A complementary investigation using a SEM showed compression-induced abrasion marks in an area immediately behind the crack tip. Fig 4.17b is a scanning electron micrograph of an asperity immediately behind the crack tip showing the area flattened due to a compressive overload of -430 MPa. This is compared to the height of an asperity in constant amplitude loading and a stress amplitude of 138 MPa in Fig 4.17a.

Using CSLM, the decrease in the asperity height (fracture surface roughness) under constant amplitude loading was verified when the superimposed compressive overloads of -300, -360, and -430 MPa were applied. The height of fracture surface irregularities near the crack tip decreased (from 28, to 18, 13, and 8 μm, respectively) as compressive overload stresses increased (from constant amplitude loading to -300, -360, and -430 MPa, respectively). The overloads resulted in significant increases in crack growth rates.

Fracture surface profiles obtained using CSLM showed that a surface crack initiates and propagates into the specimen a distance of 175-320 μm on a plane inclined to the plane perpendicular to the applied stress. The plane of crack growth then shifts to the plane perpendicular to the direction of the applied stress. It is noteworthy that the height of the asperities (obtained by CSLM) during inclined crack growth (Stage I) is less than for horizontal crack growth (Stage II). This may explain why short fatigue cracks (Stage I) have a low closure stress.

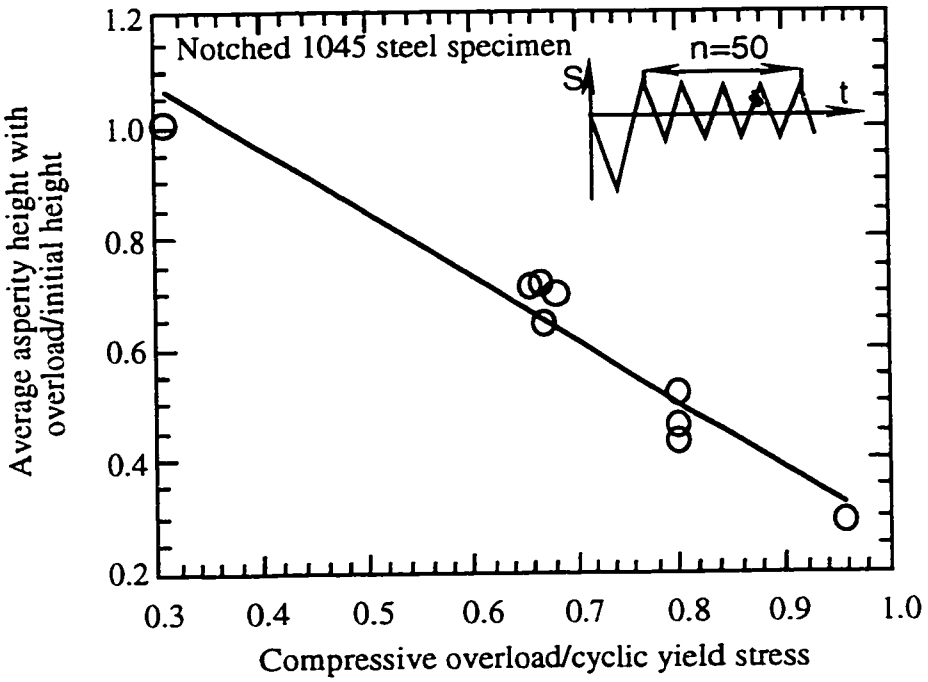

Fig 4.16 Average asperity height divided by initial asperity height versus compressive overloads.

A careful observation of the fracture surface of the specimen using a SEM verified that the fracture surface roughness height during Stage I fatigue crack growth was much less than that in Stage II crack growth.

4.3.1.2 Discussion

Uniaxial results show that the crack growth rate of short fatigue cracks in 1045 steel increases dramatically as the magnitude of compressive overload increases. A compressive overload led to a flattening of roughness asperities and therefore a reduction in closure stress. In this regard, Henkener et al [64] reported that the crack growth rate increased as the magnitude of a compressive overload increased. The increased compressive overload led to an increase in the range of the effective intensity factor. Herman et al [65] and Hertzberg et al [66] also showed that a low closure stress (due to compressive loads) is associated with the crushing of asperities in the crack wake.

The crack growth behavior of short fatigue cracks under three periodic compressive overloads (Fig 4.15) shows that the increase in crack growth rate from -300 MPa to -360 MPa compressive overload is much higher than that for an interval from -360 to -430 MPa compressive overload. For a 1mm increase in crack length in this figure, a test at a -300 MPa overload requires 8000 blocks (50×8000=400,000 cycles) while the tests with -360 and -430 MPa overloads correspond to about 1800 and 1500 blocks respectively. In this regard, Kemper et al [46] and Tack and Beevers [47] observed a similar saturation effect in which increases in compressive overload beyond a certain level did not result in additional increases in crack growth rate.

The influence of the number of small cycles following an intermittent compressive overload was studied. A higher crack growth rate is associated with a smaller number of cycles between two compressive overloads [48].

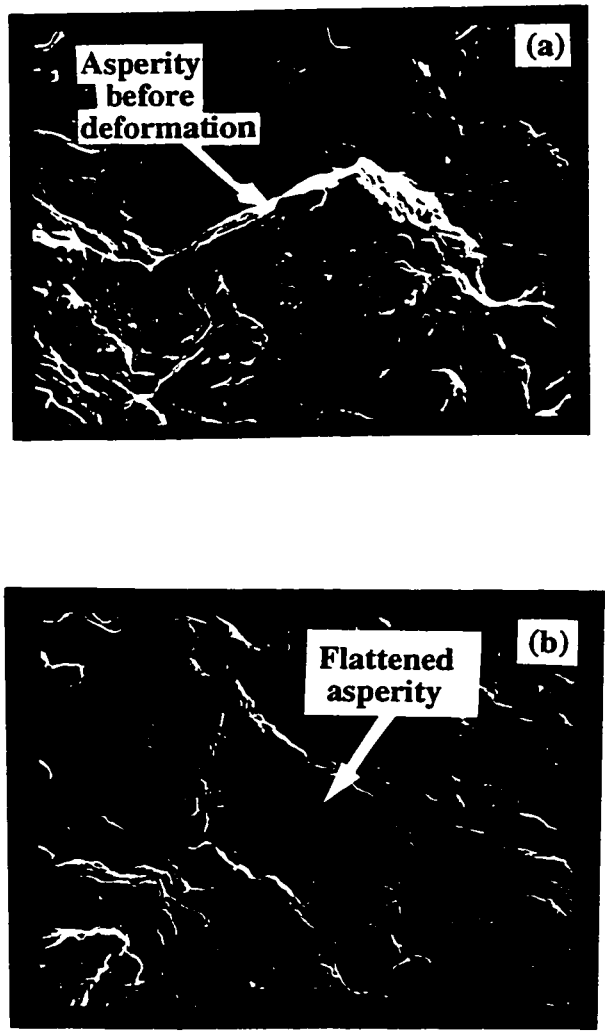

Fig 4.17 A Scanning Electron Micrograph of an asperity for a) constant amplitude loading, and b) block load history containing a periodic compressive overload of -430 MPa

Pompetzki et al [67] investigated the effects of overloads on fatigue damage in smooth specimens of SAE 1045 steel. They conducted three sets of fatigue tests, in which the number of cycles between the intermittent overload was varied. The results showed that fatigue resistance given by life curves decreased as the number of small cycles between overloads decreased. They also reported that compressive overloads decreased the crack opening stress and increased the effective stress and that as cycling at the lower stress level continued, the crack opening stress increased and the effective stress and damage per cycle decreased.

In this study, SEM fractography and a CSLM investigation of the crack fracture surface indicated that Stage I growth of short cracks in 1045 steel occurred in an inclined plane. The height of asperities on this plane (Stage I) was found to be less than that for Stage II. This may suggest that the first stage of short fatigue crack growth has a lower closure stress. This agrees with the results of Minakawa et al [68]. They showed that the closure level developed from zero closure as a function of the crack length for a Mod 9Cr-1Mo steel. The opening stress intensity factor rapidly built up in the first 200 μm of crack growth.

Crack Opening Results and Effective Crack Growth under Uniaxial Loading-Effective crack growth data were obtained using a method described by Dabayeh and Topper [69]. They suggested that closure free crack growth rate data could be obtained by measuring the crack growth rate during a periodic compressive overload test. They achieved closure free crack growth for the small cycles following the overload by choosing the frequency of overload application and the number of small cycles such that the measured crack opening stress was always below the minimum stress of the small cycles. In the uniaxial tests, at an overload of -430 MPa, the frequency of overload application was chosen such that crack opening stress remained below the minimum stress of the small cycles and fully effective fatigue data were obtained. For instance, crack opening stress,

measured for a uniaxial test with a load history containing periodic compressive overloads of -430 MPa followed by 50 small constant amplitude stress cycles with maximum and minimum stresses of 370 MPa and 167 MPa respectively, was found to be 2.50 MPa at the end of the block; well below the minimum stress. The crack opening results for 1045 steel under constant amplitude loading and periodic compressive overload histories used to calculate crack opening stresses in this thesis are those reported by MacDougall and Topper [52].

4.3.2 Shear biaxial fatigue loading ($\lambda=-1$)

4.3.2.1 Shear biaxial fatigue loading (in-phase overstraining)

Fig 4.18 illustrates a block loading history containing an in-phase periodic compressive overstrain and the crack plane for a shear biaxial fatigue loading.

The CSLM measurements and SEM examination of crack fracture surfaces, which had experienced in-phase periodic compressive overstrains, revealed that fracture surface asperities at the crack tip were severely flattened. An SEM fractograph of a specimen subjected to in-phase biaxial compressive overstrains of -0.3% followed by 19 small tension-compression cycles of ±0.15% strains is shown in Fig 4.19. A noticeable feature of the flattened asperities on the fracture surface of the in-phase PCO tests is the parallel abrasion lines. The deduction, that these lines are induced by the abrasion between crack flanks due to the compressive overstrain, is substantiated by the observation that parallel lines are formed in the same direction in all flattened areas. A reduced crack closure stress and a faster crack growth was associated with a decrease in the asperity height due to compressive overstrains.

Crack Opening Results and Effective Crack Growth under Shear Straining- Crack opening measurements for shear tests with the strain histories containing n small cycles and in-phase periodic compressive overstrains of -0.3% (yield point magnitude)

were measured. Using CSLM image processing technique revealed that shear cracks were fully open at zero internal oil pressure in tubular specimens. Therefore crack growth rates obtained were closure free and fatigue lives were fully effective. It was found that the shear cracks stay open for values of n small cycles less than 50 after a periodic compressive overstrain.

Figure 4.20 illustrates the crack growth of shear cracks under in-phase biaxial shear loading histories of i) in-phase compressive overstrain cycles only (IPCO), ii) in-phase periodic compressive overstrain (IPCO) of -0.3% followed by n=19 small cycles, and iii) a constant shear strain amplitude (CSSA) of 0.3%.

4.3.2.2 Shear biaxial fatigue loading (180° out-of-phase overstraining)

The detrimental effects of periodic compressive overstrains on the biaxial shear crack growth and fatigue life were diminished when compressive overstrains were applied with a 180° delay in time as shown in Fig 4.21. Figure 4.22 illustrates the crack growth of shear cracks under 180° out-of-phase biaxial shear loading histories of i) 180° out-of-phase compressive overstrain cycles only (PCO), ii) 180° out-of-phase periodic compressive overstrain (IPCO) of -0.3% followed by n=19 small cycles, and iii) a constant shear strain amplitude (CSSA) of 0.3%. A comparison of crack growth from Fig 4.20 and Fig 4.22 reveals that periodic compressive overstrains resulted in a faster crack growth and reduced fatigue life when they were applied in-phase. The fatigue life of a specimen under an in-phase PCO history was found to be 5.7 times shorter than the one under 180° out-of-phase compressive overstrain cycles at the same alternating small strain cycles. An SEM fractograph of a specimen subjected to 180° out-of-phase biaxial compressive overstrains of -0.3% followed by 19 small amplitude strain cycles of 0.15% is shown in Fig 4.23.

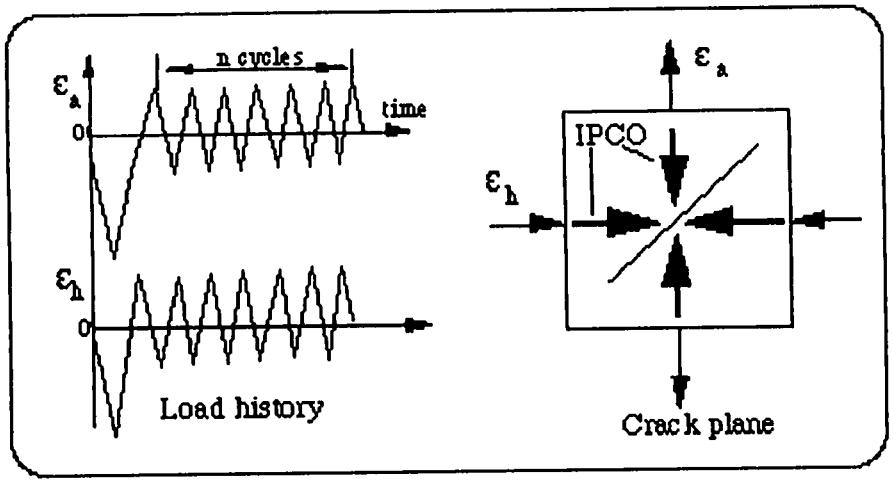

Fig 4.18 Load history and crack plane for an in-phase periodic compressive overstrain (IPCO) followed by **n** small cycles (180° out-of-phase)

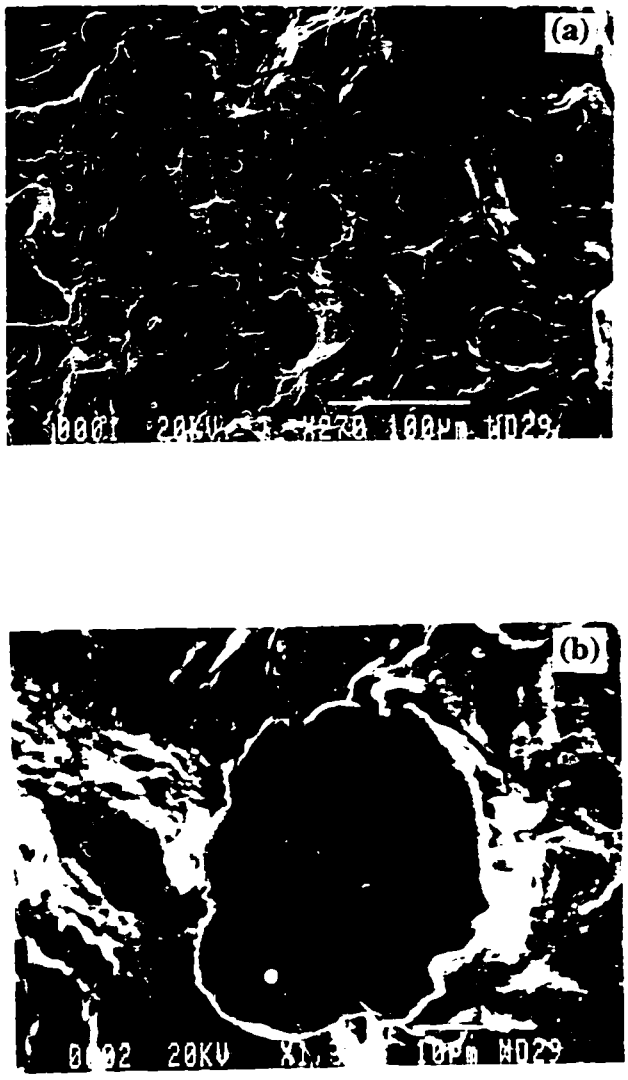

Fig 4.19 a) Flattened fracture surface asperity due to the in-phase PCO shear loading, and b) a magnified flattened asperity showing the parallel abrasion lines.

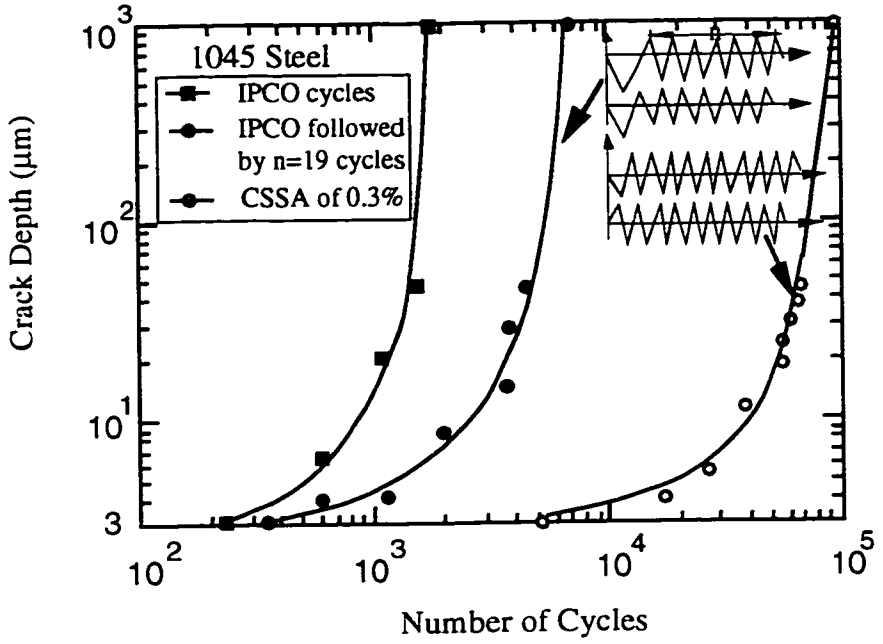

Fig 4.20 Crack depth versus number of cycles for CSSA and an in-phase PCO (IPCO)test when the number of small cycles between overstrains is 19.

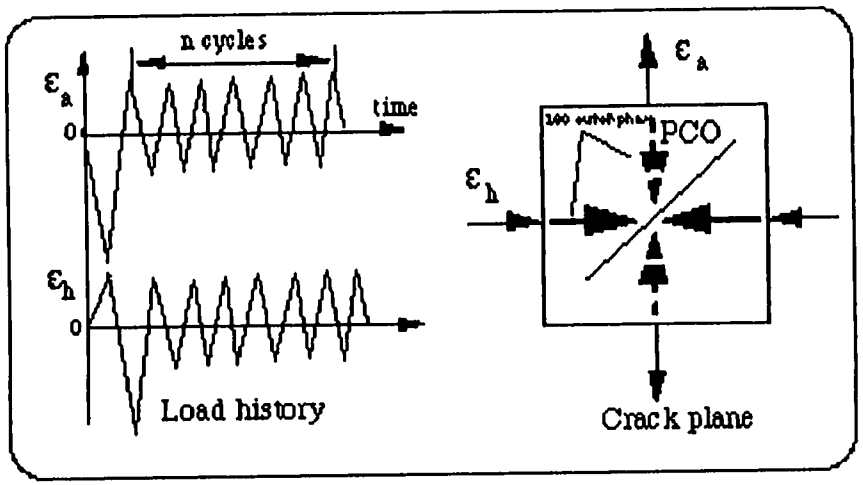

Fig 4.21 Load history and crack plane for a 180° out-of-phase compressive overstrain followed by n small cycles (180° out-of-phase).

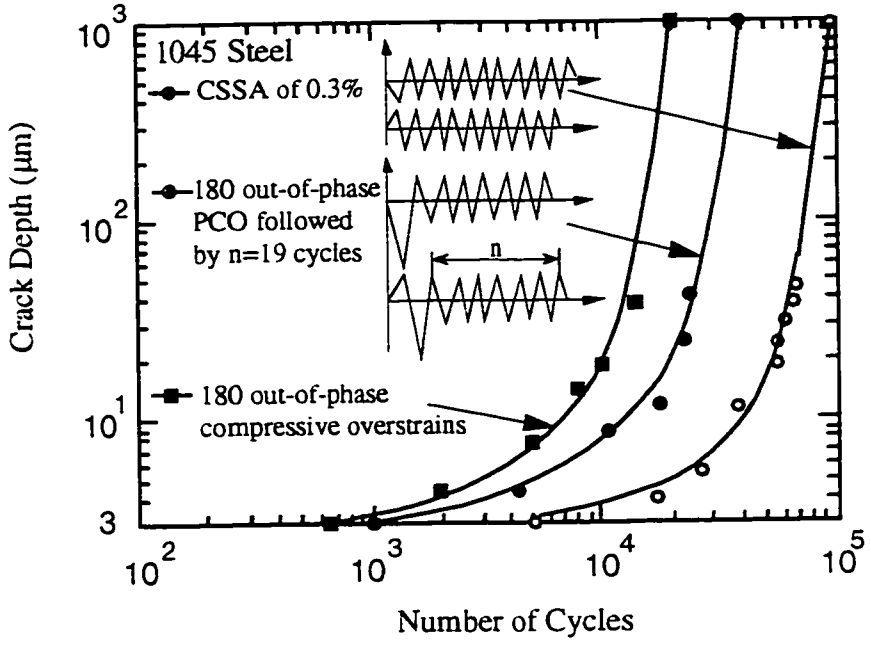

Fig 4.22 Crack depth versus number of cycles for CSSA and 180° out-of-phase PCO test when the number of small cycles between overstrains is 19.

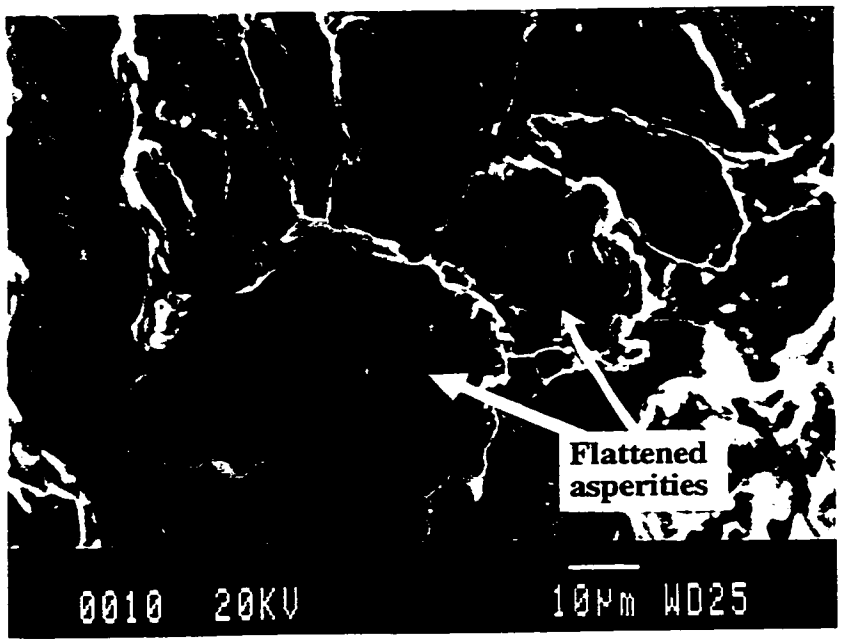

Fig 4.23 Plastically crushed fracture surface asperity under 180° out-of-phase PCO shear loading.

4.3.3 Equibiaxial fatigue loading (λ=+1)

Fig 4.24 illustrates a block loading history containing an in-phase periodic compressive overstrain followed by a number of small cycles in equibiaxial fatigue and the loading in the crack plane.

The CSLM measurements of and SEM examination of a fracture surface, which had experienced in-phase periodic compressive overstrains, revealed that fracture surface asperities at the crack surface were severely flattened. An SEM fractograph of a specimen subjected to in-phase equibiaxial compressive overstrains of -0.3% followed by 19 small amplitude strain cycles of 0.15% is shown in Fig 4.25.

Fig 4.26 shows a significant increase in the crack growth of equibiaxial cracks (λ=+1) when in-phase periodic compressive overstrain cycles are applied after every n small in-phase cycles. Application of PCO cycles decreases the number of cycles required for crack initiation and reduces the fatigue life. The detrimental effects on the fatigue crack growth and life are mainly due to the crushing of fracture surface asperities by compressive overstrains.

Crack Opening Results and Effective Crack Growth under Equibiaxial Straining- Crack opening measurements for equibiaxial fatigue tests with strain histories containing in-phase periodic compressive overstrains of -0.3% followed by n small positive high R-ratio cycles showed that the equibiaxial cracks were fully open at zero stress at the end of all small cycle blocks for values of n less than 50.

The pressurizing device opened the crack via internal pressure but could not compress the specimen so that crack opening stresses in compression could not be measured. Therefore, all small strain cycles with positive strain ratios were open throughout the strain cycle. Data from this will be used later in the thesis for effective strain and effective ΔK data.

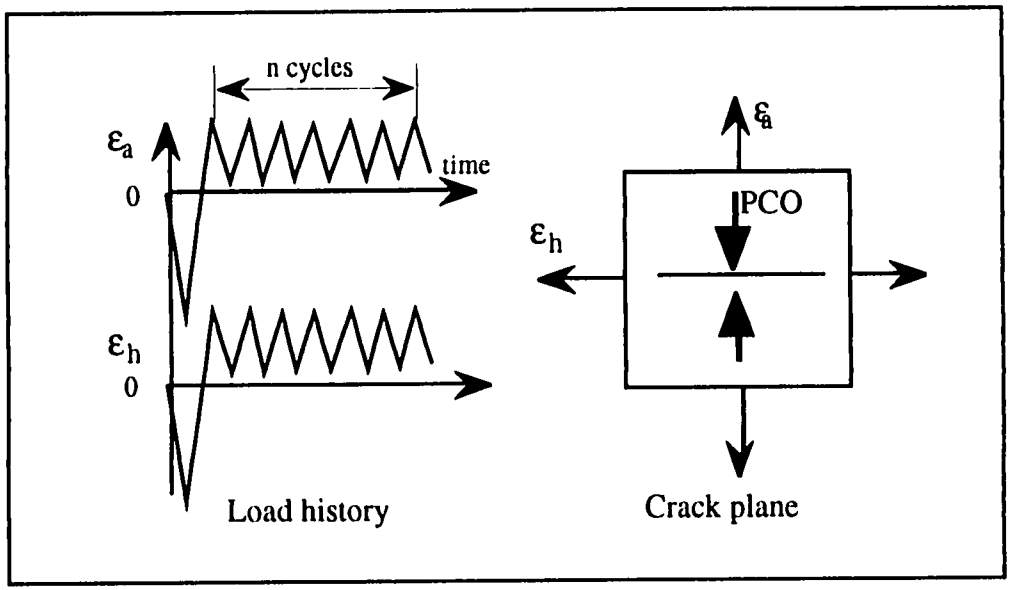

Fig 4.24 Load history and crack plane for an in-phase compressive overstrain followed by n in-phase small cycles.

Fig 4.25 Plastically crushed fracture surface asperity under an in-phase PCO equibiaxial fatigue loading.

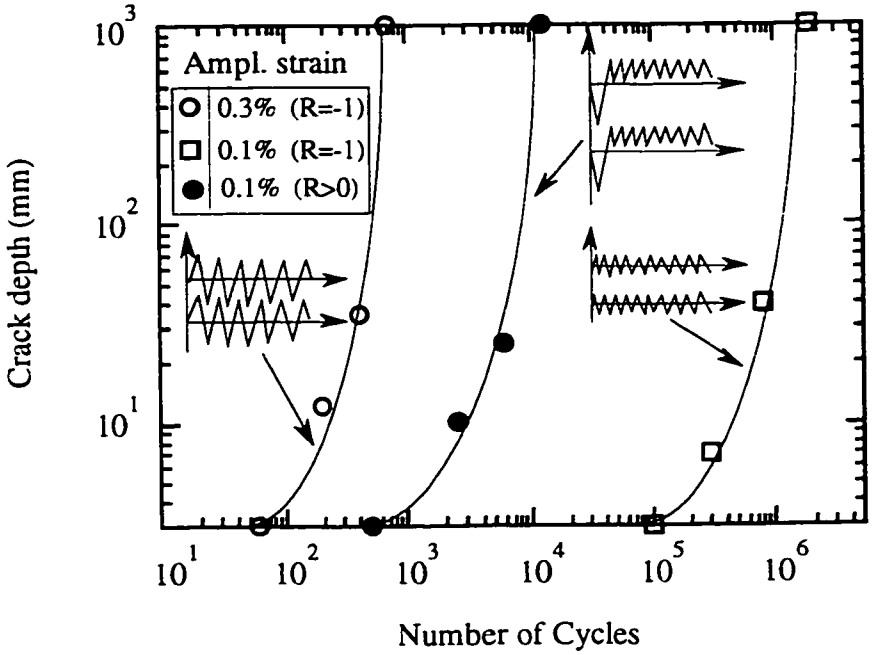

Fig 4.26 Crack growth results from initiation to failure under equibiaxial CAL and PCO fatigue loading.

4.3.4 Fatigue loading under a biaxial strain ratio of $\lambda=-0.625$

Fig 4.27 illustrates a block loading history containing an in-phase periodic compressive overstrain and the crack plane during a biaxial fatigue loading of $\lambda=-0.625$. The CSLM measurements and SEM examinations of fracture surfaces, which had experienced in-phase periodic compressive overstrains, revealed that fracture surface asperities at the crack tip were severely flattened. An SEM fractograph of a specimen subjected to in-phase biaxial compressive overstrains of -0.3% followed by 50 small strain cycles of $\pm 0.145\%$ axial strain and $\pm 0.09\%$ hoop strain is shown in Fig 4.28. A reduced crack closure stress and a faster crack growth was associated with a decrease in the asperity height due to compressive overstrains.

Fig 4.29 presents the crack depth measurement results versus the number of cycles of biaxial fatigue tests ($\lambda=-0.625$) under load histories containing periodic compressive overstrain cycles. In-phase periodic compressive overstrains reduced the closure stress by decreasing the fracture surface roughness. This resulted in a faster crack growth.

Crack Opening Results and Effective Crack Growth under a Biaxial Strain ratio of -0.625- Crack opening measurements for tests with a biaxial strain ratio of -0.625 containing n small cycles and in-phase periodic compressive overstrains of -0.3% (yield point magnitude) were measured. The CSLM image processing technique revealed that the cracks were open at zero stress in the tubuiar specimens for values of n less than 50 cycles and consequently all positive strain ratio small cycles in these tests are open throughout the small strain cycle and their strain range is effective.

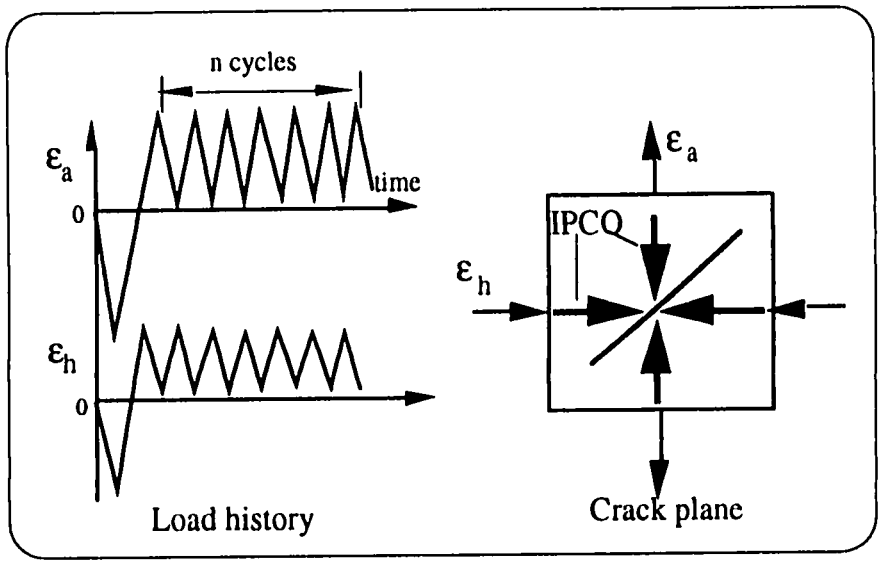

Fig 4.27 Load history and Crack plane for an in-phase periodic compressive overstrain (IPCO) followed by **n** small cycles (180° out-of-phase) with the biaxiality ratio of -0.625.

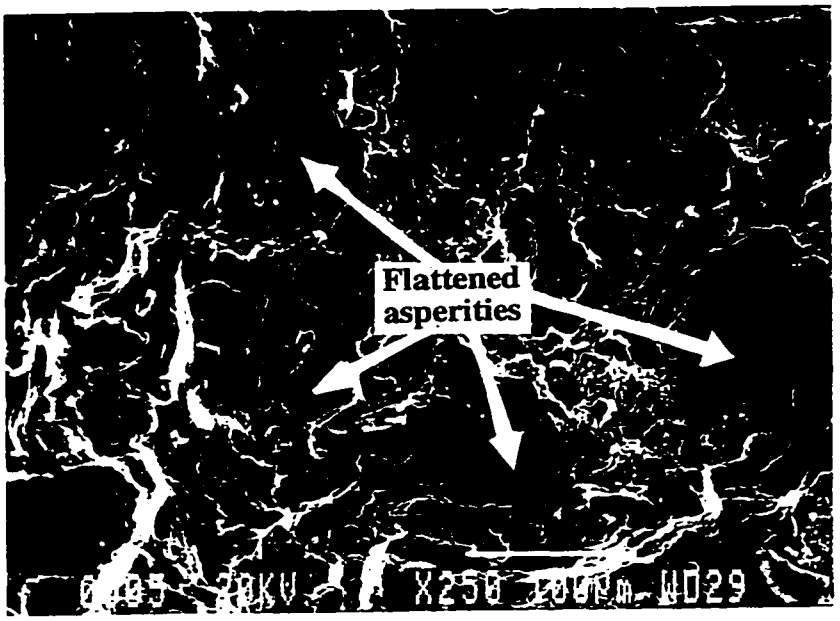

Fig 4.28 Plastically crushed fracture surface asperity under an in-phase PCO biaxial fatigue loading (λ=–0.625).

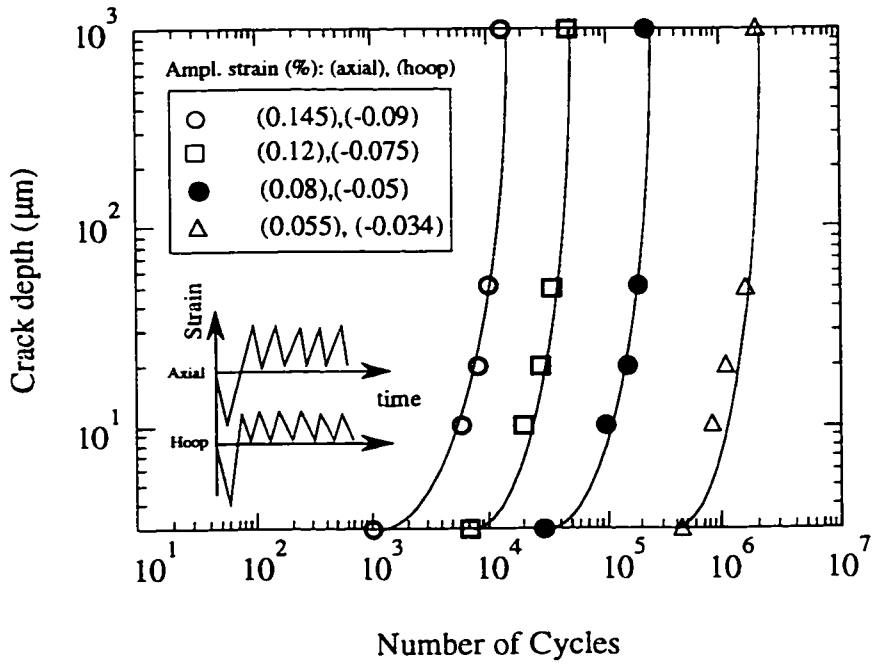

Fig 4.29 Crack growth results from initiation to failure under biaxial fatigue loading (biaxiality ratio of -0.625) containing periodic compressive overstrain of -0.3%.

4.4 Summary and Discussion

Crack growth of biaxial fatigue cracks under constant amplitude loading and a load history having a periodic compressive overstrain was investigated. Biaxial fatigue tests were carried out using thin-walled SAE 1045 steel tubular specimens subjected to axial load and internal-external pressure.

Four biaxial principal strain ratios (hoop strain/axial strain) were used λ=-1 (pure shear loading), λ=-ν (uniaxial loading), biaxial strain ratio of λ=-0.625, and λ=+1 (equibiaxial loading).

In the pure shear loading (λ=-1), surface cracks initially nucleated on slip bands at 45° to the axis of the specimen which coincides with the plane of maximum shear strain. Growth on the shear planes (microcracks) into the specimen occupied up to 90% of fatigue life during which time the surface length of the microcracks remained nearly constant. Microshear cracks started propagating in the length after 90% of fatigue life as soon as crack became semi-circular (a/c=1). Failure then occurred by a rapid linking of microcracks at the end of a test.

In uniaxial loading (λ=-ν), cracks initiated along the maximum shear plane at 45° to the surface of the specimen (Stage I growth) and failure then took place by Stage II growth perpendicular to the axis of the specimen.

In tests with the biaxial strain ratios of λ=-0.625, crack initiation and early damage development were observed along planes of maximum shear strain at about 40°-45° to the axial direction of the tubular specimen. Microcracks initiated at various positions in the gage length of the specimen. The behavior of microcracks for this strain ratio was similar to

microcracks initiated under pure shear loading. Fatigue failure occurred by a rapid linking up on microcracks at the end of a test.

In equibiaxial fatigue loading (λ=+1), cracks nucleated on the two maximum shear planes parallel and perpendicular to the specimen axis and propagated into the specimen on planes at 45° to the specimen surface. In equibiaxial fatigue loading, once a crack initiated, it grew in the length and depth directions until failure took place.

The CSLM measurements and an SEM examination of the growth of short fatigue cracks under uniaxial and biaxial constant amplitude loading and during load histories having periodic compressive overload of yield stress magnitude revealed that the crack growth increased dramatically with the magnitude of the compressive overload. The height of the fracture surface irregularities reduced as the compressive overload increased progressively, and flattened fracture surface asperities near the crack tip. This resulted in a reduced crack closure stress and a faster crack growth.

The plastic deformation of the fracture surface asperity, and its geometry change as the magnitude of periodic compressive overloads increases, will be discussed in the next chapter.

CHAPTER 5

The Effect of Periodic Compressive Overload (PCO) Histories on the Fracture Surface Asperity Shape

Introduction

In the previous chapter, the growth of short fatigue cracks under constant amplitude loading and load histories having periodic compressive overloads of various magnitudes was investigated. It was revealed [44,45,48,59] that the fracture surface near the crack tip and the crack growth increased dramatically with the magnitude of the compressive overload. The height of the surface irregularities reduced as the compressive overload increased progressively flattened fracture surface asperities near the crack tip. This resulted in a significantly reduced crack closure stress and a faster crack growth. If a crack is subjected to pure shear mode loading, its flanks are in contact. For roughness-induced crack closure, the key proposition is that sliding mode displacements lead to a mismatch of the fracture surfaces where asperities have been formed.

This chapter examines the influence of periodic compressive overloads on the fracture surface of short fatigue cracks, crack growth and closure under uniaxial and biaxial fatigue loading in SAE 1045 steel.

5.1 Closure Free Crack Growth

5.1.1 Uniaxial fatigue crack growth tests

Crack length and depth for uniaxial loading crack growth tests were obtained as the number of cycles increased using CSLM for Stage I cracks and a 500X optical microscope for Stage II cracks. The aspect ratio (crack depth/half crack length) of uniaxial small cracks (up to 550μm length) was found to be 0.80. Increasing the magnitude of the periodic compressive overload resulted in faster crack growth up to an overload of -430 MPa. Increasing the magnitude of the compressive overload above -430 MPa did not result in further increases in crack growth rate. Similarly, Kemper et al [46] and Tack and Beevers [47] reported a saturation in crack growth rate when the magnitude of a compressive overload increases beyond of a certain level. In this study, the saturation of the crack growth rate at a periodic compressive overload level of -430 MPa was shown by CSLM image processing to correspond to closure free crack growth.

5.1.2 Biaxial fatigue loading tests

Crack growth rate data were obtained from biaxial specimens subjected to constant amplitude straining and to the strain histories containing in-phase periodic compressive overstrains with a peak magnitude of -0.3% after every n small strain cycles.

Crack opening stress measurements and crack depth measurements for biaxial fatigue cracks (λ=-1, -0.625, +1) made using confocal scanning laser microscopy (CSLM) image processing of the crack profile, showed that, for the periodic compressive overloads used, the cracks were fully open at zero internal pressure. Therefore, there was no crack face interference. Crack depths used for calculating crack growth rate were taken at the deepest point at the shear crack profile.

5.2 Fracture Surface Asperities and Crack Closure

The SEM and CSLM observations of the fracture surface near the crack tip on the fatigued surface of both uniaxial and biaxial specimens, revealed that asperities were approximately cone-shaped during constant amplitude loading. When overloads were applied the height of the cone decreased and the apex widened but the base diameter did not change because each asperity is constrained by its neighbors [70]. Figure 5.1 illustrates schematically the original geometry of the asperities and the profile after the application of compressive overloads of near yield point magnitude.

For a uniaxial constant amplitude fatigue crack growth test of 138 MPa, the average heights of the asperities at the deepest point of a crack with a length of about 1000 μm before and after plastic deformation due to the various magnitude of periodic compressive overloads are given in Table 5.1. Table 5.1 also presents the average heights of the asperities before and after crushing due to the periodic compressive overstrain of -0.3% (=410 MPa) in an area of $1mm^2$ of the crack front of the biaxial shear cracks. The documented average height of asperities under CAL and PCO histories for both uniaxial and shear biaxial loading measured from a number of uniaxial flat and biaxial tubular specimens respectively are tabulated in this Table.

To simplify the analysis, the final shape of asperity was assumed to be a cylinder. To calculate the total true strain, the initial and final shape of the asperity was divided into j elements (see Fig 5.2). The height of every element (shown in Fig 5.2a) is considered to be 1 μm. The diameter of a cylindrical element (i+1) of the initial asperity shape was taken to be $d_{(i+1)} = d_i + 2h_i \tan\theta$ where 2θ is the asperity tip angle.

Table 5.1 Initial and final average heights of fracture surface roughness under uniaxial and biaxial shear loading.

Uniaxial loading			Biaxial shear loading		
load history (MPa)	Initial height h_0 (μm)	Final height[1] h_f (μm)	Strain history (%)	Initial height[1] h_0 (μm)	Final height[1] h_f (μm)
(±138,-300)*	28	18	(±0.08,-0.3)*	100	38
(±138,-300)*	30	20	(±0.08,-0.3)*	120	45
(±138,-300)*	33	20	(±0.08,-0.3)*	110	40
(±138,-300)*	29	20	(±0.10,-0.3)*	90	35
(±138,-360)*	28	13	(±0.10,-0.3)*	95	37
(±138,-360)*	32	14.5			
(±138,-360)*	35	12			
(±138,-430)*	30	8			

(1). Average height of fracture surface asperities in an area of $1mm^2$.

(*). The first value in the bracket is the amplitude of small cycles, and the second value is the magnitude of the periodic compressive overload/overstrain.

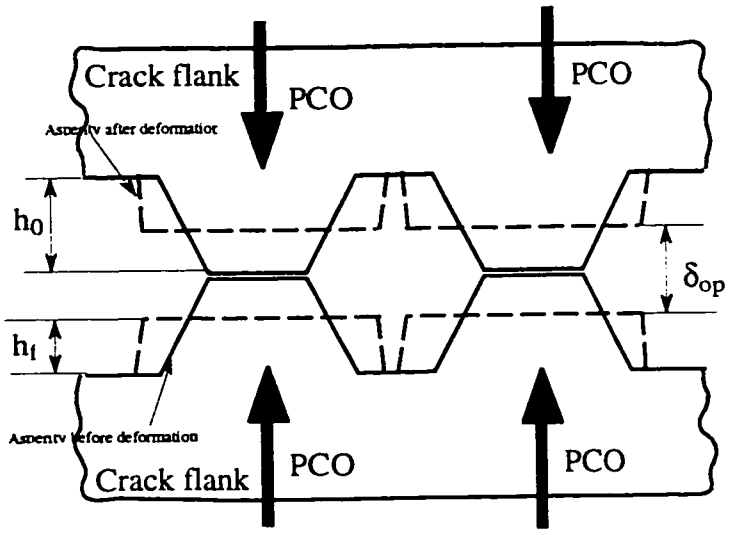

Fig 5.1 Schematic presentation of the fracture surface at the tip of crack under constant amplitude loading (solid line) and periodic compressive overload history (Dashed line).

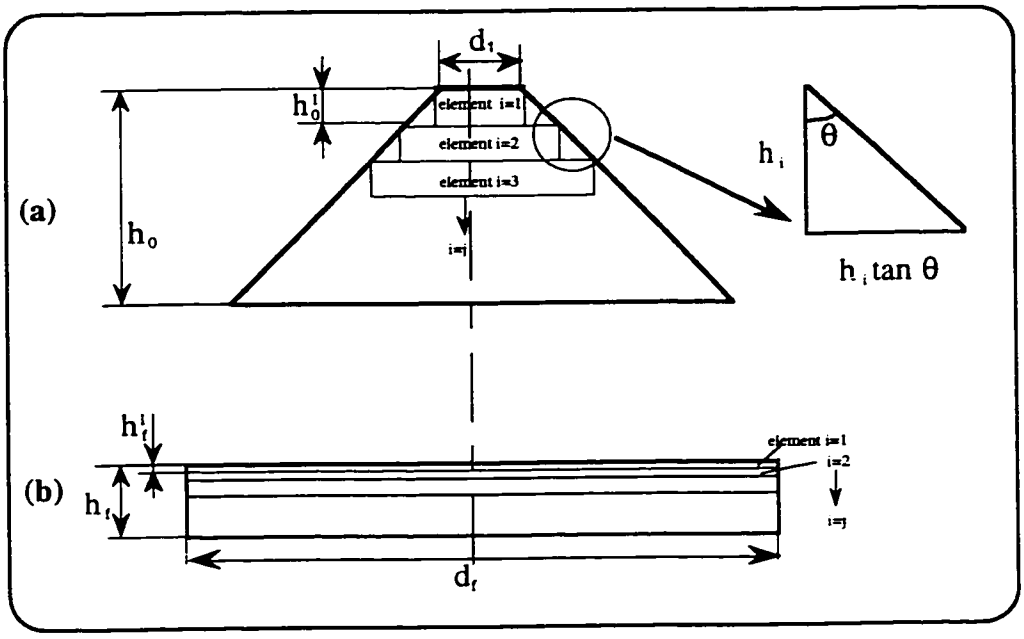

Fig 5.2 The geometry shape of a single asperity a) before and b) after the application of PCO.

For the asperity volume to be conserved, the volume of every element in the initial shape of the asperity has to be equal to the volume of the corresponding element in the final shape of the asperity. The true strain of the ith cylindrical element of the asperity is

$$\varepsilon_T^i = \text{Ln}\ \frac{h_0^i}{h_f^i} \tag{5.1}$$

where, h_0^i and h_f^i are the initial and final height of the element, respectively.
The results of calculations of the true strain of elements from the tip to the base of a single asperity are given in Fig 5.3. The variation in true strain from the tip to the base of the asperity as shown in Fig 5.3 can be described by an exponential function

$$\varepsilon_T = A \exp\left(-B\frac{x}{h_0}\right) \tag{5.2}$$

where A is the maximum lateral strain calculated as the natural logarithm of the ratio of the initial (A_i^1) to final contact area (A_f^1) of an asperity and the parameter B is a constant that describes the decay of total strain as x/h_0 increases. The constants A and B are given in Fig 5.3.

The value of ε_T decreases exponentially as shown in Fig 5.3. The application of periodic compressive overloads, plastically crushed asperities on the crack fracture surface. Flattened asperities on the crack flanks reduced interlocking asperity (closure), therefore, the crack closure stress decreased. This reduction in closure stress increased when the magnitude of the compressive overload increased. In a previous study [48], it was shown that asperity height changes versus magnitude of compressive overload in uniaxial loading is linearly related as $\rho = \frac{h_f}{h_o} = -0.66 + 2.95\left(\frac{\sigma_a}{|\sigma_{pco}|}\right)$.

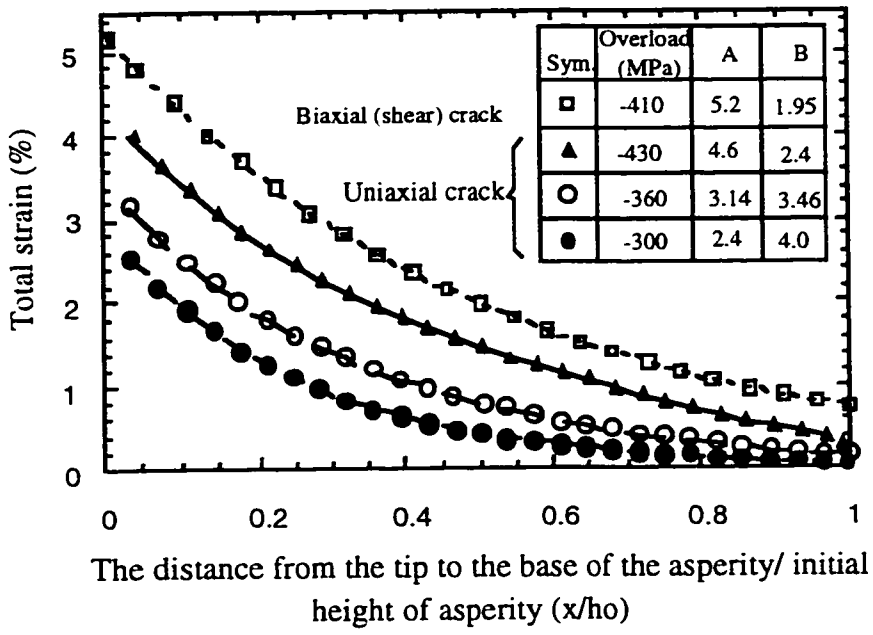

Fig 5.3 Exponential variation of strain versus x/h_0 under compressive overloads

In the PCO biaxial shear tests when the magnitude of in-phase compressive overstrain was -0.3%, the ratio ρ was found to be 0.364.

Crack opening stress results, obtained using CSLM image processing of the crack profile, revealed that cracks were open at zero static stress for the periodic compressive overload histories. The difference between the asperity heights before (h_0) and after (h_f) the application of the compressive overloads results in a gap between the two crack flanks. This gap is due to inelastic deformation of the asperities which can be defined geometrically as

$$\delta_{op} = \phi(2h_0 - 2h_f) = 2\phi\ h_0(1-\rho) \tag{5.3}$$

where $\phi = x/h_0$, $x = h_0 - h_f$, and therefore $(1-\rho) = \phi = 1.66 - 2.95\left(\frac{\sigma_a}{|\sigma_{pco}|}\right)$. Therefore, eqn (5.3) can be rewritten as

$$\delta_{op} = 2\phi^2\ h_0 \tag{5.4}$$

Substituting h_0 from eqn (5.2) in to the eqn (5.4) we have:

$$\delta_{op} = 2\phi^2 \left(\frac{B\,x}{Ln(A/\varepsilon_T)}\right) \tag{5.5}$$

It is found that the asperity induced crack closure has a more dominant effect near the threshold than in the Paris regime. Therefore, the role of flattened asperities in affecting fatigue crack growth is also expected to be significant for baseline ΔK values which fall in the near threshold regime. In a study analogous to the present study, Suresh [41] reported that the compressive overloads are likely to have a more dominant effect on near threshold fatigue crack growth than in the higher growth rate regimes of fatigue. Similarly, he

documented that the effect of flattened asperities and residual tensile stresses generated due to the compressive overload, particularly for short fatigue cracks, resulted in crack opening and crack growth acceleration.

5.3 Summary and Discussion

1. The confocal scanning laser microscopy (CSLM) and scanning electron microscopy (SEM) examinations of fracture surfaces revealed that the periodic compressive overstrains applied flattened mismatch asperities near the crack tip. The height of mismatch asperities on the crack fracture surface was reduced dramatically by the application of in-phase periodic compressive overstrains. The reduction in the height of these irregularities on the fracture surface was accompanied by the opening of the crack in the mouth and depth directions and an acceleration in the crack growth rate.

2. In spite of the number of geometric models [32-35] of roughness-induced crack closure presented under Mode I and Mode II fatigue loading under constant amplitude loading condition, there are a very few roughness-induced closure models [31,62] describing the behavior during periodic overload histories. The models that do exist lack quantitative information concerning the changes in fracture surface asperities.

In the present study, a geometric model of the plastic deformation of the fracture surface asperities at the crack tip (under periodic compressive overloads) was developed for both uniaxial and biaxial shear loading conditions. This model assumes that the volume of initially cone-shaped asperities is conserved during plastic deformation by the compressive overloads. The model correlates the magnitude of the periodic compressive stress, the fracture surface asperity height and the plastically flattened area based on the CSLM measurement of the fracture surface asperities with a high resolution and accuracy [71].

3. It was found that the fracture surface near the crack tip and the crack growth rate changed dramatically with the application of the compressive overloads. When the

magnitude of compressive overloads was increased, the height of the fracture surface irregularities was reduced as the increasing overload progressively flattened fracture surface asperities near the crack tip.

The model presented gives quantitative information concerning the geometry of fracture surface asperities under constant amplitude loading and the deformation during periodic compressive overload histories. This provides a better understanding of the effect of the crack face interference on the crack closure and growth rate.

CHAPTER 6

The Modeling of Biaxial Fatigue Crack Growth Rate and Life Prediction

6.1 Biaxial Fatigue Life Results and Parameters

6.1.1 A brief review of fatigue life parameters

Several life prediction models have been proposed to estimate fatigue life under different multiaxial loading conditions. Early researchers [5,23,72] proposed shear stress based theories for ductile materials and principal stress based theories for brittle materials in high cycle fatigue. In low cycle fatigue, equivalent strain [73-76], plastic strain energy [77] and critical plane approaches [8,24] have been used to correlate fatigue data for a variety of loading conditions.

The critical plane theory devotes specific attention to the orientation of small cracks in multiaxial fatigue. This theory asserts that the most damaged plane is the one having the maximum shear strain amplitude. This class of approaches for predicting fatigue life emphasizes the identification of critical planes on which various combinations of shear and normal stresses (strains) are assumed to govern fatigue behaviour. Fatigue analysis using the critical plane concept is based on the crack initiation plane and the early stages of crack

growth. These approaches intend to reflect observed cracking behaviour and appear to overcome a number of deficiencies of equivalent stress (strain) and energy approaches. The critical parameter is taken to be the maximum cyclic shear strain in the critical shear plane together with a function of the normal strain or stress on that plane. The use of this parameter is based on the premise that the normal stress or strain assists shear crack propagation by opening the crack, thereby reducing crack face asperity interaction.

6.1.2 Fatigue life results under CAL and PCO histories

Crack growth observations in the present study, revealed that fatigue crack initiation occurred in persistent slip bands. The direction of these persistent slip bands was coincident with the maximum shear strain direction and fatigue cracks always initiated on the maximum shear strain plane. This agrees with the theory that the fatigue crack initiation process is predominantly controlled by the maximum shear strain amplitude (γ_{max}).

Crack opening stress measurements for shear fatigue cracks (λ=-1) made using confocal scanning laser microscopy (CSLM) image processing of the crack profile, showed that the cracks were fully open at zero internal static pressure [44] when periodic compressive overstrains of -0.3% were applied in-phase. For biaxial fatigue tests with strain ratios of -0.625 and +1 and a -0.3% overstrain, the numbers of small strain cycles was kept small enough that after the small cycles in a block were applied the cracks were open at zero stress. Since the device used to open cracks in the CSLM via internal pressure could only apply tensile stresses no information on crack closure in compression could be obtained. However, since the cracks were open at zero stress, it is known that all positive stress ratio cycles are fully effective.

Similarly, in the uniaxial tests at an overload of -430 MPa, the frequencies of overload applications and the number of small cycles were chosen such that crack opening stress remained below the minimum stress of the small cycles and fully effective fatigue

data were obtained. At lower overload stresses the crack was not fully open during all the small cycles.

In the block loading histories containing periodic compressive overstrains, the total damage is equal to the sum of the damage due to the small cycles and the damage due to the overload cycles.

$$D_T = D_{SM} + D_{OL} \tag{6.1}$$

Subscripts (T), (SM) and (OL) denote respectively the total number of cycles in a block of the loading history, the number of small cycles and the number of overload cycles.
After accounting for the damaging effect of the overstrain cycles, the equivalent number of small cycles to cause failure in PCO histories is calculated as

$$N_{eq} = \frac{N_T\left(1-\frac{1}{n}\right)}{1-\left(\frac{N_T}{n\,N_{f\,OL}}\right)} \tag{6.2}$$

where n is the number of small cycles following a compressive overload in a block loading history, N_T is the total number of cycles, and $N_{f\,OL}$ is the number of overstrain cycles to failure. The derivation of the equivalent number of small cycles to failure is given in Appendix D.

Strain amplitude versus equivalent fatigue life data plotted in Fig 6.1a show that the fatigue strength is reduced by a factor that ranged from 1.24 at short lives to 3.37 at long lives when periodic compressive strains of -0.3% were applied in uniaxial tests. The corresponding reductions in the shear fatigue strength under shear tests vary from 1.40 at short lives to 1.70 at long lives (Fig 6.1b).

The equibiaxial fatigue strength was reduced by a factor that ranged from 1.65 at short lives to 2.5 at long lives when periodic compressive overstrains of -0.3% were applied (Fig 6.1c)

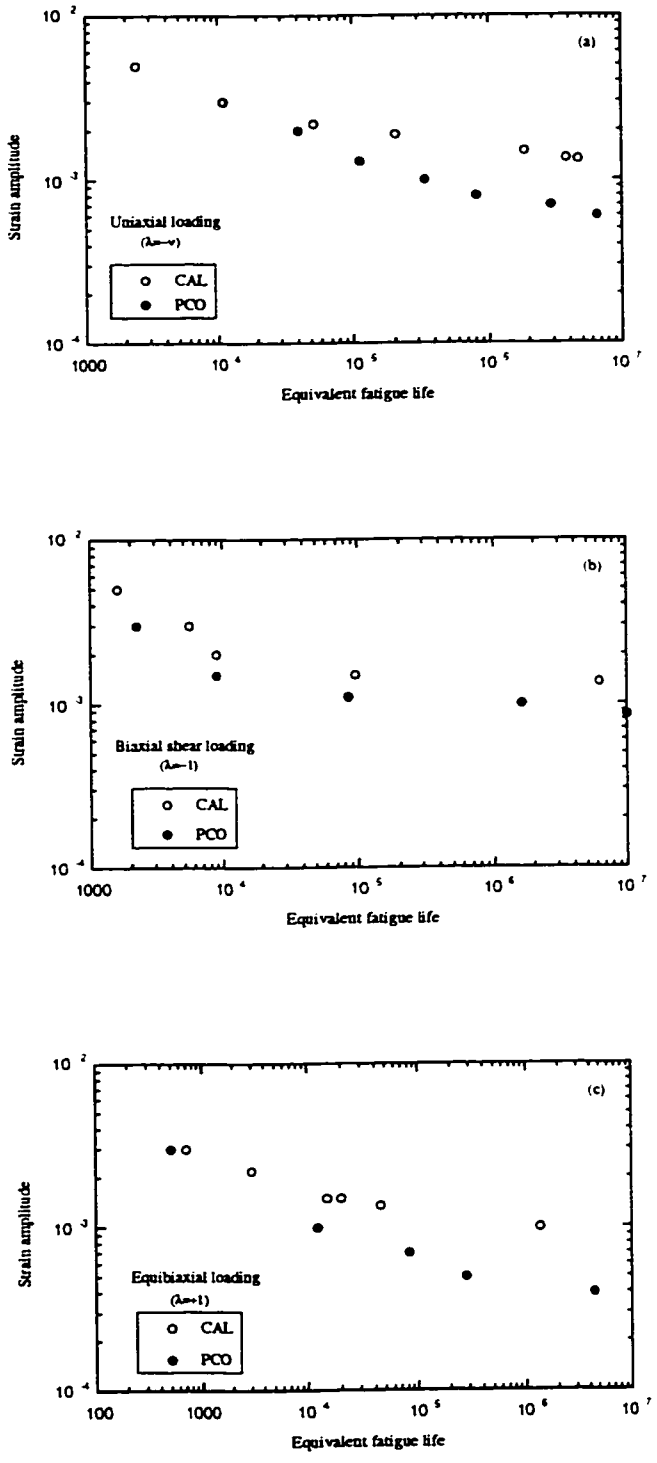

Fig 6.1 Fatigue life data under CAL and PCO histories: a) uniaxial loading, b) shear loading , and c) equibiaxial loading.

6.1.3 The correlation of fatigue data by various critical plane theories

Under both constant amplitude loading and load histories containing periodic compressive overloads, fatigue failure defined by oil leaking through the specimen thickness occurred when the crack length exceeded 2.0 mm. Fatigue life results under the four biaxial strain ratios of λ=-v, -0.625, -1, and +1 under constant amplitude loading (R=-1) were plotted based on i) the maximum shear strain approach, ii) the Brown and Miller parameter, iii) the Kandil et al. parameter, iv) the Fatemi and Socie parameter and v) the Glinka et al. parameter in Figs. 6.2a-6.6a.

The fatigue lives obtained under constant amplitude loading (with closure) and various biaxial strain ratios were collapsed successfully in one curve when they were evaluated based on the shear strain approach, the Brown and Miller parameter, the Kandil et al. parameter, and the Fatemi and Socie parameter. The Glinka et al. parameter showed a good correlation of fatigue life data under biaxial strain ratios of -1, -0.625, and +1, however, data obtained for λ=-v lay above the life data of the other strain ratios.

Effective fatigue life data obtained under periodic compressive overload histories and various biaxiality ratios were also plotted using i) the maximum shear strain approach, ii) the Brown and Miller parameter, iii) the Kandil et al. parameter, iv) the Fatemi and Socie parameter, and v) the Glinka et al. parameter and shown in Figs 6.2b-6.6b. Only those data for which crack closure measurements showed that the crack remained open throughout the stress cycle, are plotted.

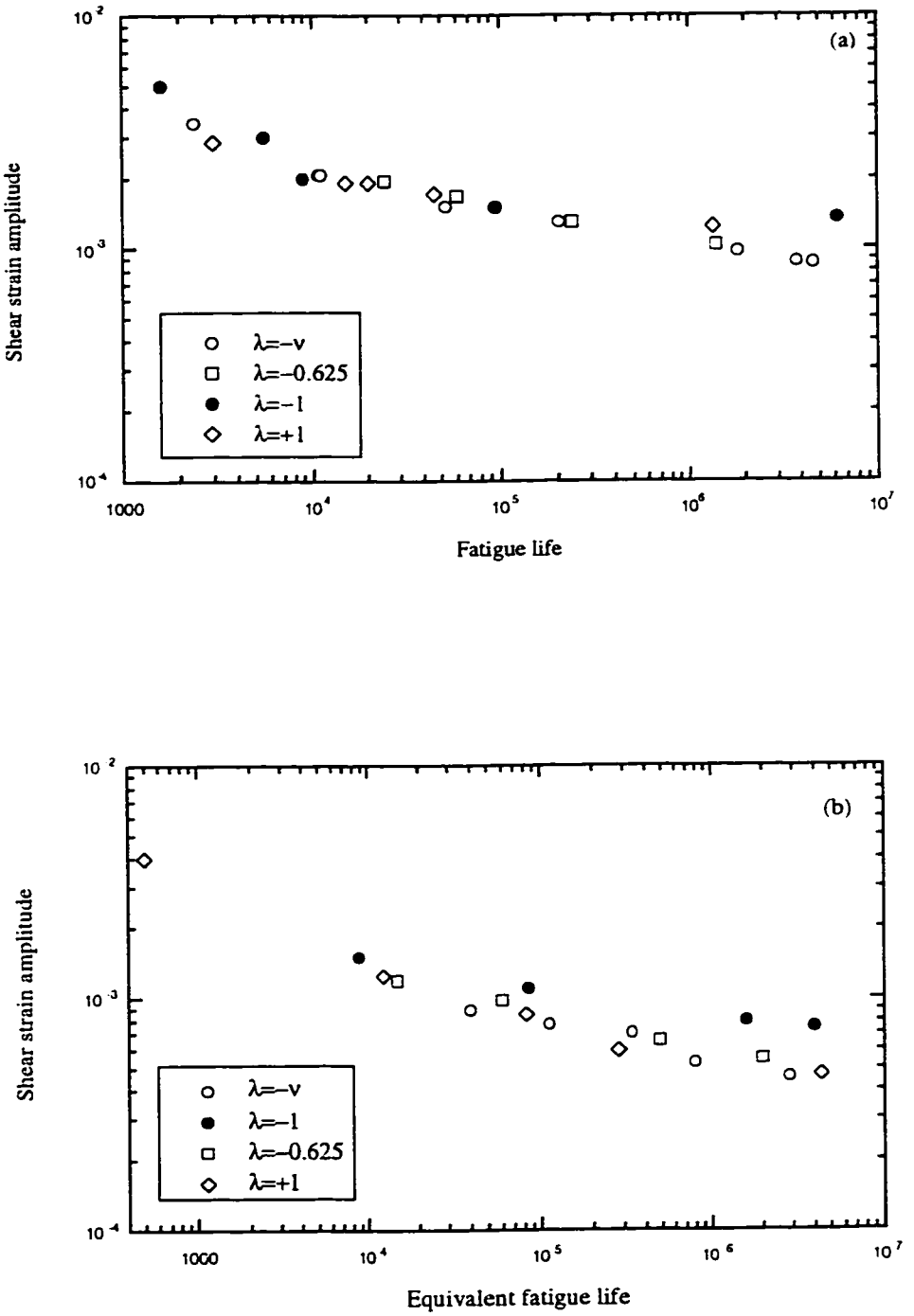

Fig 6.2 Fatigue life versus maximum shear strain amplitude for various strain ratios: a) constant amplitude loading, and b) strain histories containing PCO of yield point magnitude.

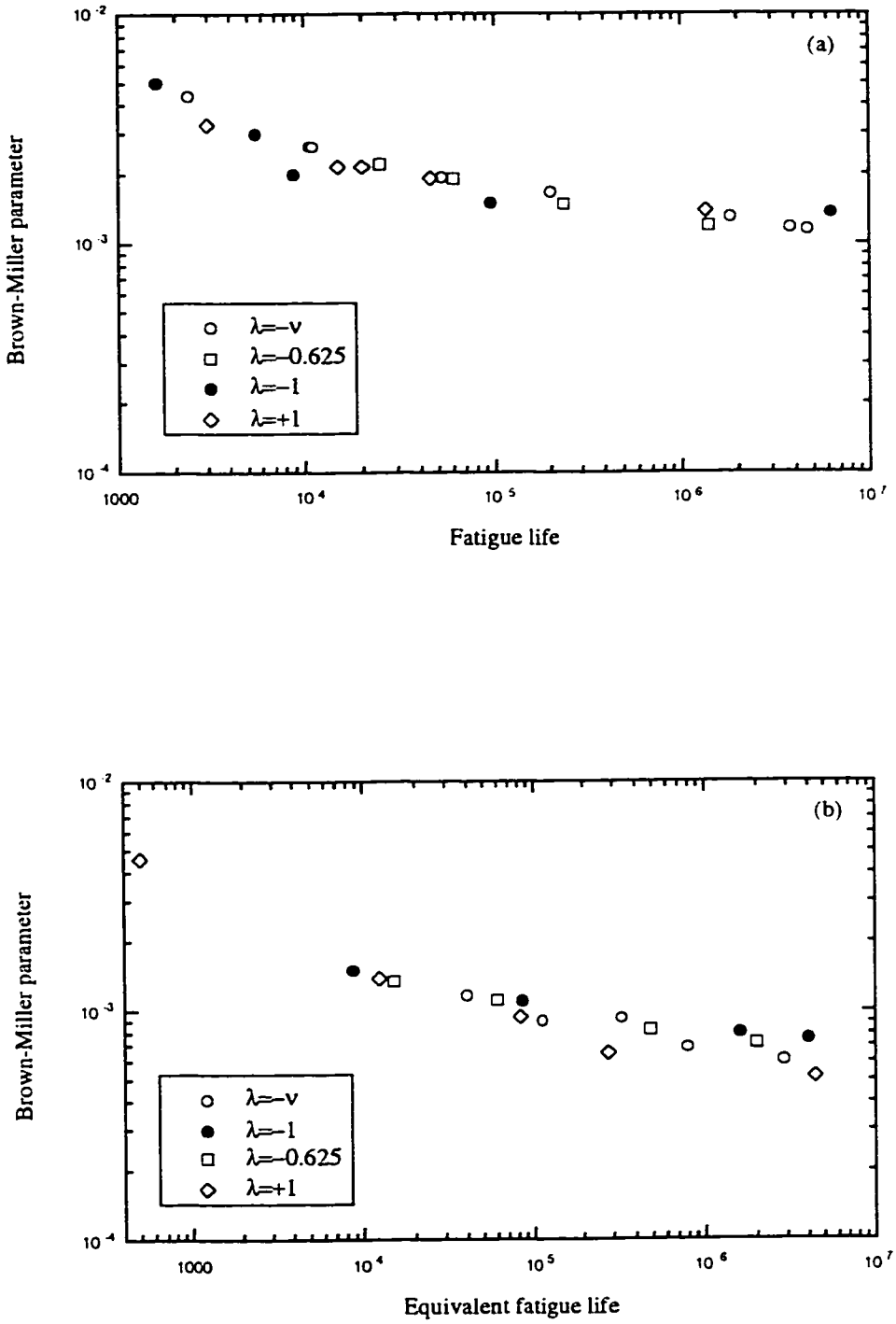

Fig 6.3 Fatigue life versus the Brown and Miller parameter for various strain ratios: a) constant amplitude loading, and b) strain histories containing PCO of yield point magnitude.

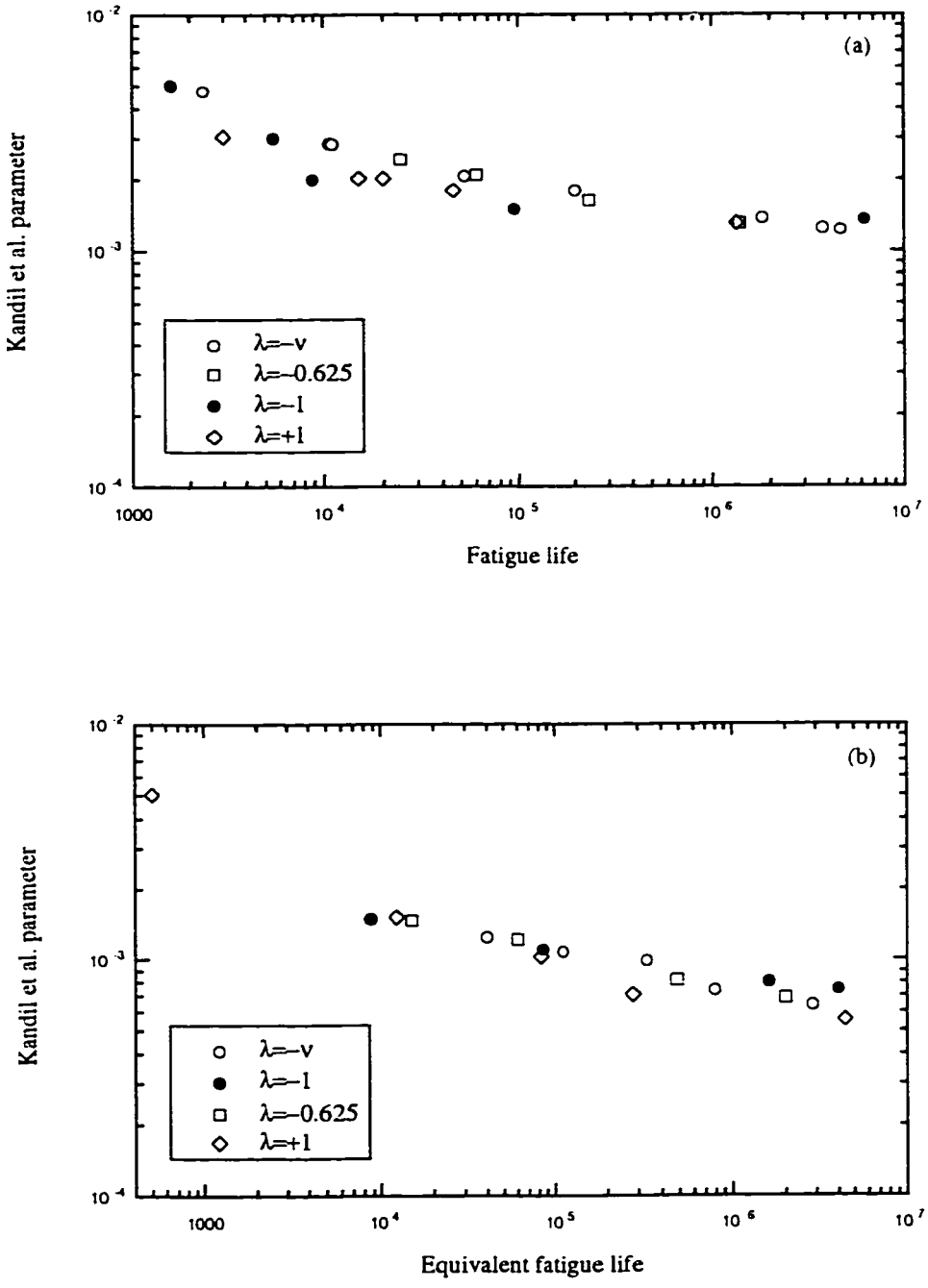

Fig 6.4 Fatigue life versus the Kandil et al. parameter for various strain ratios: a) constant amplitude loading, and b) strain histories containing PCO of yield point magnitude.

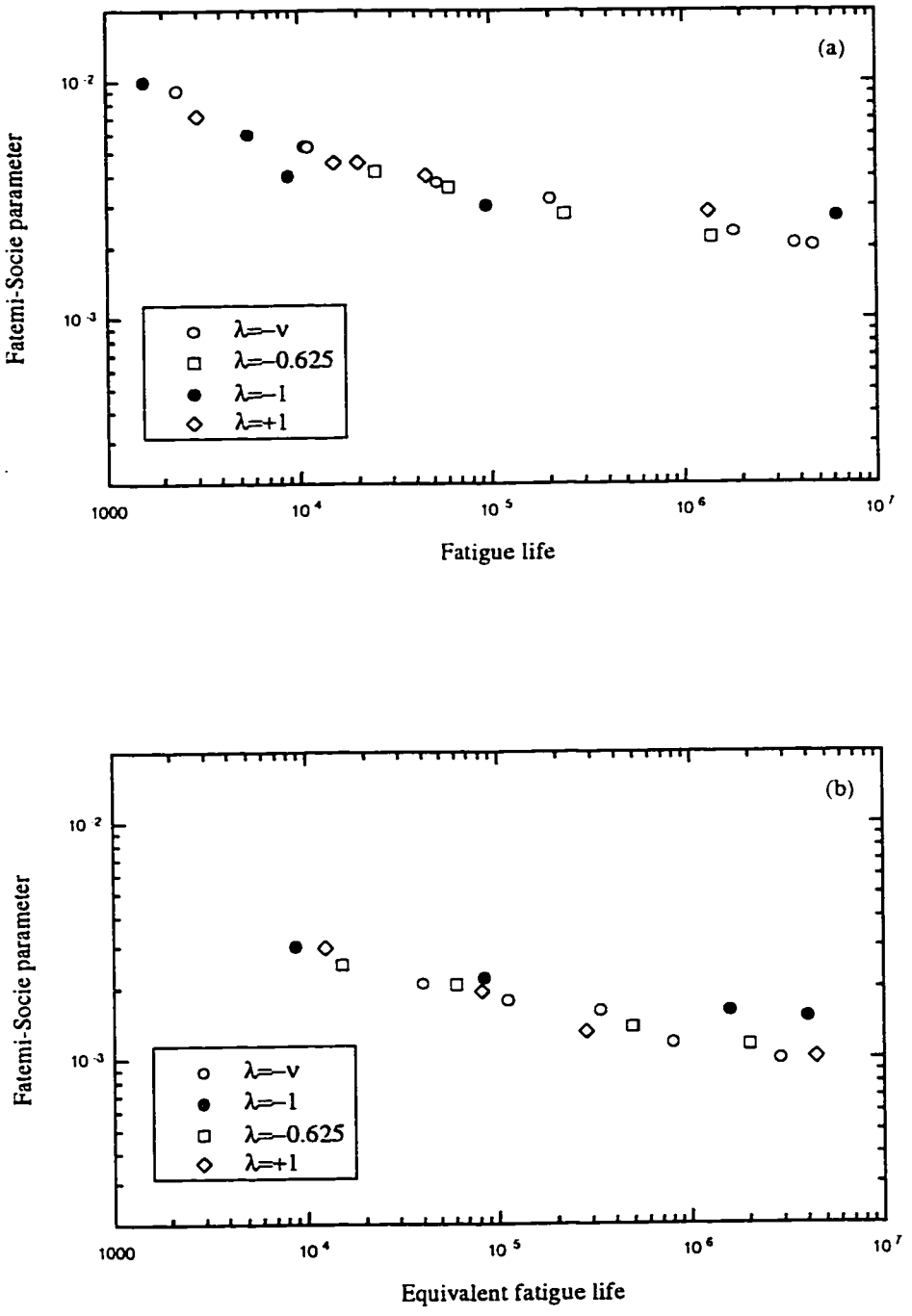

Fig 6.5 Fatigue life versus the Fatemi and Socie parameter for various strain ratios: a) constant amplitude loading, and b) strain histories containing PCO of yield point magnitude.

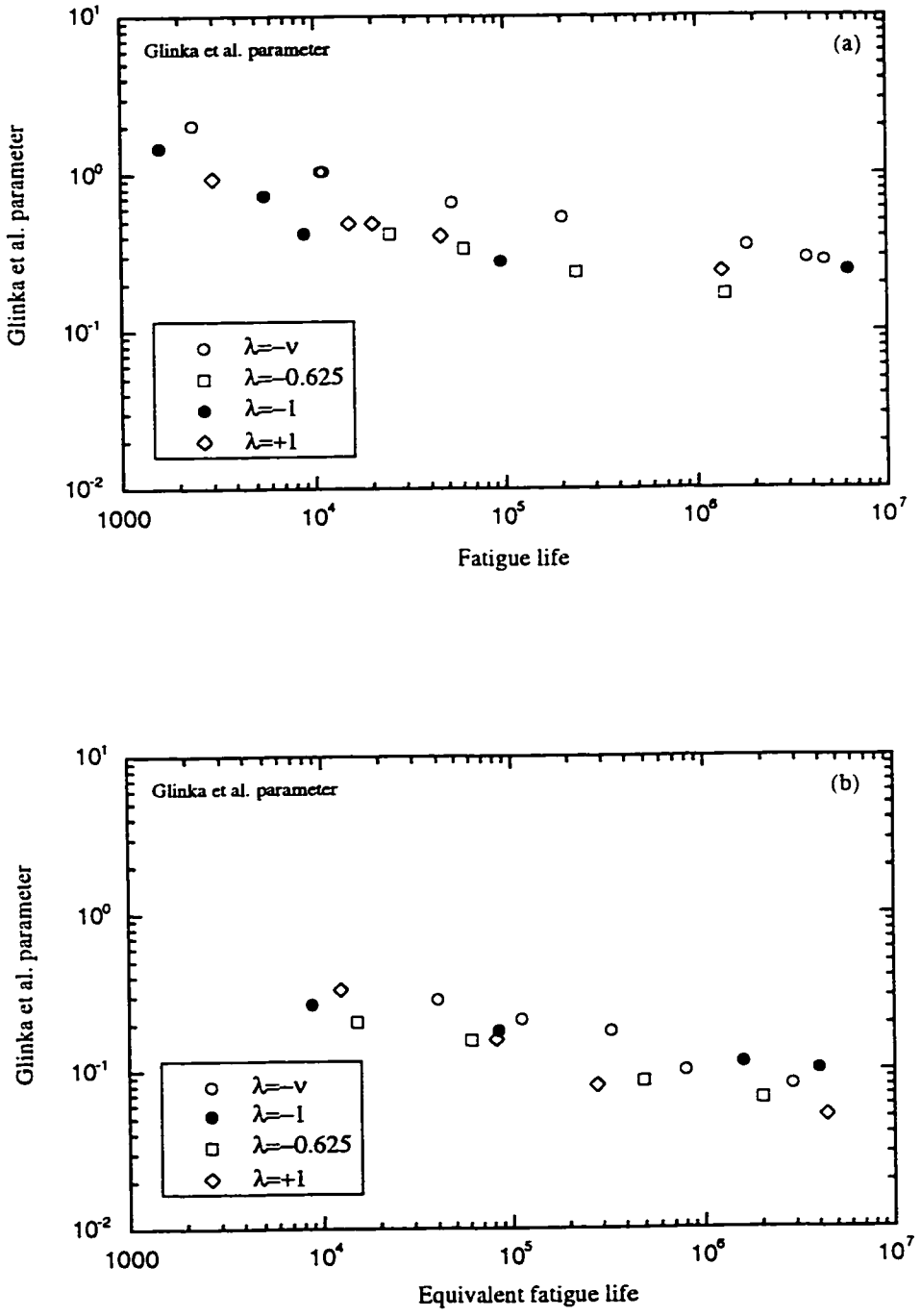

Fig 6.6 Fatigue life versus the Glinka et al. parameter for various strain ratios: a) constant amplitude loading, and b) strain histories containing PCO of yield point magnitude.

The effective life data for the four strain ratios of -v, -0.625, -1, and +1 are correlated reasonably well by the shear strain and the Brown and Miller approaches for lives less than 10^6 cycles but the Kandil et al. Parameter and the Fatemi and Socie parameter showed better correlations over the whole LCF plus HCF region. The Glinka et al. parameter correlated the effective life data under various strain ratios within a scatter bounds of ±3 in life.

6.2 Fully Effective Biaxial Fatigue Crack Growth Rate and Fatigue Life Prediction

Introduction

Observations of the formation and growth of small cracks made by the present author in previous studies [44,45,48] and other researchers [11,78], showed that materials exhibited prolonged Stage I propagation behaviour along maximum shear planes. Some investigations [20,79] have demonstrated a robust correlation of fatigue under various stress states based on the assumption that the peak normal stress to the plane of maximum range of shear strain directly affects the Stage I shear dominated propagation of small cracks. Socie et al. [80] and Berard et al. [81-82] have shown that the simple bulk stress and strain range parameters in the critical shear plane can correlate the propagation rate of small multiaxial cracks.

The strain based critical shear plane parameters that were used to correlate the fully effective life data under biaxial strain ratios of -v, -0.625, -1 and +1 will now be used as driving forces to describe the crack growth rates and predict the fatigue life.

6.2.1 Crack growth rate modeling

The Stress intensity factor is extensively used as a parameter to describe crack propagation under Mode I loading conditions. A few parameters have been proposed for the propagation of the crack during multiaxial loading [83]. However, these parameters only apply to linear elastic fracture mechanics. For small cracks, elastic-plastic fracture mechanics should be considered. Several researchers [80,84,85] have used correlations between fatigue crack growth rate and parameters expressed in terms of total strain and crack length. Imai and Matake [86] employed a strain based intensity factor by replacing the cyclic stress range with the product of cyclic strain range and elastic modulus.

Strain intensity factor range values [87] were calculated for a semi-elliptical surface crack under Mode I (uniaxial) loading using,

$$\Delta K_I = F_I\, Q\, E\, \Delta\varepsilon\sqrt{\pi a} \qquad (6.3a)$$

Similarly, the strain intensity factor range was calculated for a semi-elliptical surface crack under Mode II (shear) using eqn (6.3b)

$$\Delta K_{II} = F_{II} Q \Delta\, \gamma\, G\sqrt{\pi a} \qquad (6.3b)$$

where the ΔK_I and ΔK_{II} are the strain intensity factor range for uniaxial and shear loading, F_I and F_{II} are the shape factors (see Appendix A) for a semi-elliptical uniaxial crack, and shear crack, respectively, Q is the surface strain concentration factor [87], $\Delta\varepsilon$ and $\Delta\gamma$ are the cyclic normal and shear strain ranges (R=-1) respectively, E and G are the elastic and shear moduli respectively, and a is the crack depth on the plane of maximum shear strain. The strain concentration factor Q is a function of crack depth, a, and grain size, D, given by eqn (6.4)

$$Q = 1 + 5.3 \exp\left(-\alpha \frac{a}{D}\right) \tag{6.4}$$

where α/D is used as a constant which fits the measured fatigue limit strain $\Delta\varepsilon_{fl}$ to the maximum strain calculated from

$$\Delta\varepsilon_{th} = \frac{\Delta K_{th}}{F\,Q\,E\sqrt{\pi a}} \tag{6.5}$$

In eqn (6.5), for uniaxial loading and pure shear loading, the shape factor F corresponds to F_I and F_{II} respectively. Shape factors F_I and F_{II} are given in Appendix A.

The effective strain intensity factor range was modeled based on critical plane strain components. Critical plane approaches postulate that cracks initiate and propagate on the maximum shear strain plane and that the normal strain to this plane assists in the fatigue crack growth process. The components of this model consist of the maximum shear strain range and the normal strain range acting on that plane.

Equations (6.6a-6.6c) provide the effective strain intensity factor ranges based on the shear strain parameter, the Brown and Miller parameter, and the Kandil et al. parameter respectively.

$$\Delta K^{S}_{eff} = F_{II}\,Q\,G\,\Delta\gamma\sqrt{\pi a} \tag{6.6a}$$

$$\Delta K^{BM}_{eff} = Q\,G\,(F_{II}\,\Delta\gamma + 0.78F_I\,\Delta\varepsilon_n)\sqrt{\pi a} \tag{6.6b}$$

$$\Delta K^{K}_{eff} = Q\,G\left[F_{II}\,(\Delta\gamma)^{0.5} + 0.73\,F_I(\Delta\varepsilon_n)^{0.5}\right]^2\sqrt{\pi a} \tag{6.6c}$$

where shear modulus $G=E/2(1+\nu)$ and Poisson's ratio in this study is $\nu=0.3$.

The derivation of equations (6.6b) and (6.6c) are given in Appendix D.

6.2.2 Crack growth results under uniaxial and biaxial fatigue loading conditions

6.2.2.1 Crack growth under various strain ratios in terms of effective strain intensity

Crack length and depth for uniaxial loading crack growth tests were obtained as the number of cycles increased using CSLM for Stage I cracks and a 500X optical microscope for Stage II cracks. The aspect ratio (crack depth/half crack length) of uniaxial small cracks (up to 550μm length) was found to be 0.80. Increasing the magnitude of the periodic compressive overload resulted in faster crack growth up to an overload of -430 MPa. Increasing the magnitude of the compressive overload above -430 MPa did not result in further increases in crack growth rate. Similarly, Kemper et al. [46] and Tack and Beevers [47] reported a saturation in crack growth rate when the magnitude of a compressive overload increases beyond a certain level. In this study, the saturation of the crack growth rate at a periodic compressive overload level of -430 MPa was shown by CSLM image processing to correspond to closure free crack growth.

Crack growth rate data were obtained from biaxial specimens subjected to constant amplitude straining and to the strain histories containing in-phase periodic compressive overstrains with a peak magnitude of -0.3% after every n small strain cycles.

Crack opening stress measurements and crack depth measurements for biaxial fatigue cracks (λ=-ν, -1, -0.625, and +1), made using confocal scanning laser microscopy (CSLM) image processing of the crack profile, showed that, for the periodic compressive overloads and number of small cycles used, cracks were fully open at zero internal pressure. Therefore, there was no crack face interference for positive stress ratios of the small cycles. Crack depths used for calculating crack growth rate were taken at the deepest point of the shear crack profile.

The crack growth rate for the small cycles in the uniaxial and biaxial PCO test histories was obtained by subtracting the crack growth due to the compressive overstrain cycles from the growth per block due to the periodic compressive overloads followed by n small cycles and dividing by the number of small cycles per block.

$$\left(\frac{da}{dN}\right)_{Small} = \frac{n+1\left(\frac{da}{dN}\right)_{Total} - \left(\frac{da}{dN}\right)_{overload\ cycles}}{n} \qquad (6.7)$$

Equation (6.7) was first used for uniaxial fatigue loading of Al 2024-T351 by Dabayeh and Topper [69].

6.2.2.2 Effective strain intensity factor range versus crack growth rate

The crack growth rates for strain ratios of -v, -0.625, -1, and +1 were calculated using eqn (6.7) and are plotted in Figs.6.7a-6.7c versus the effective strain intensity factor range calculated from eqns (6.6a-6.6c). Fig.6.7 presents the effective ΔK_{eff}-da/dN curves for fatigue cracks under load histories containing in-phase periodic overstrains for ΔK_{eff} values based on the shear strain, the Brown and Miller and the Kandil et al. parameters. The ΔK_{eff}-da/dN curves plotted based on these critical plane parameters present approximately the same range of scatter. For all the parameters, the shear cracks (λ=-1) propagate slightly more rapidly than other strain ratios particularly at higher ΔK_{eff} values.

Brown and Miller [88] who tested AISI 316 steel specimens under uniaxial, shear, and equibiaxial loading conditions also found crack growth to be more rapid in shear. Tanaka et al. [89] found that the shear crack growth rate of SNCM8 was similar to the crack growth rate under tensile loading at low stress intensity factors, but, at higher stress intensities, the shear crack growth rate was faster than the corresponding crack growth rate under tensile loading.

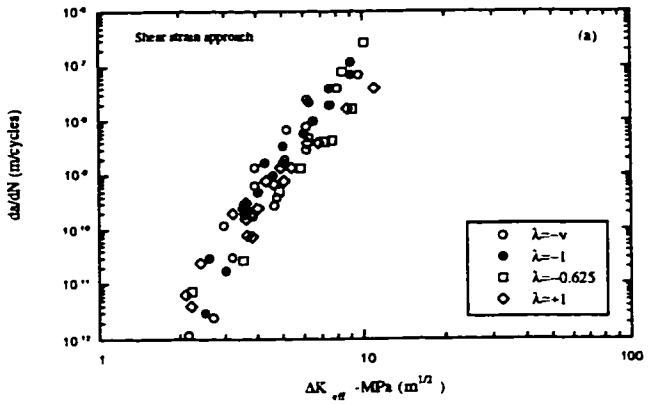

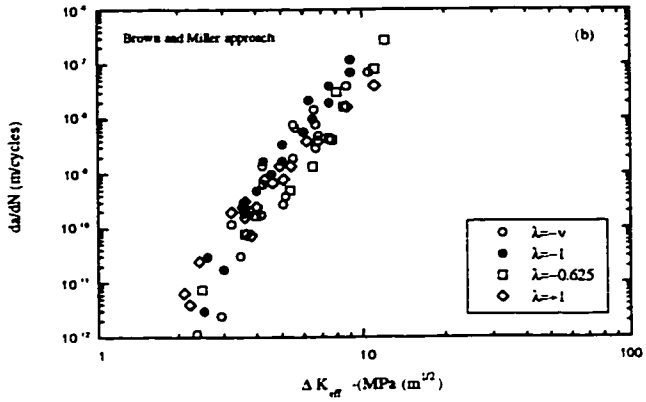

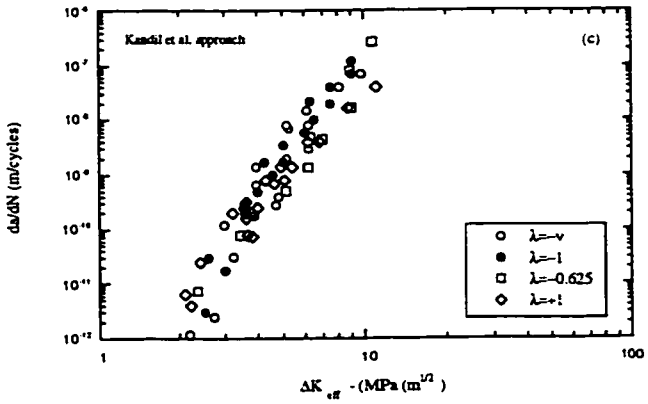

Fig 6.7 Crack growth rate versus effective strain intensity factor range based on: a) the shear strain parameter, the Brown and Miller parameter, and c) the Kandil et al. parameter.

6.3 Fatigue Life Prediction

Fatigue life predictions for biaxial strain ratios of -ν, -0.625, -1, and +1 were obtained by the numerical integration of da/dN-ΔK_{eff} curves. The limits of integration were from a slip band crack of a_i =3 μm to a crack depth of a_f=1000 μm (tubular specimen thickness) at failure.

$$N_f = \int_{a_i}^{a_f} \frac{da}{f(\Delta K_{eff})} \tag{6.8}$$

Fig 6.8 presents an algorithm for biaxial fatigue life prediction.

The fatigue life prediction program used the fitted curve of ΔK_{eff}-da/dN data (Fig 6.7). The fatigue life predictions obtained from ΔK_{eff}-da/dN data for the shear strain parameter for various strain ratios are presented in Fig 6.9. Predicted fatigue lives are plotted versus experimental fatigue lives using the shear strain parameter, the Brown and Miller parameter, and the Kandil et al. parameter in Fig 6.10. Correlations are within a factor of ±3 in life for all of the parameters. Only a few data points at lives greater than 10^6 cycles fall slightly outside the upper and lower limit bounds of ±3 in life shown by solid lines. This figure also shows that the predicted and observed lives are correlated within a factor of ±2 shown by dashed upper and lower bounds for lives up to 10^5 cycles. This suggests that these strain based critical plane approaches (the shear strain parameter, the Brown and Miller parameter, and the Kandil et al. parameter) give better correlations for low cycle than for high cycle fatigue.

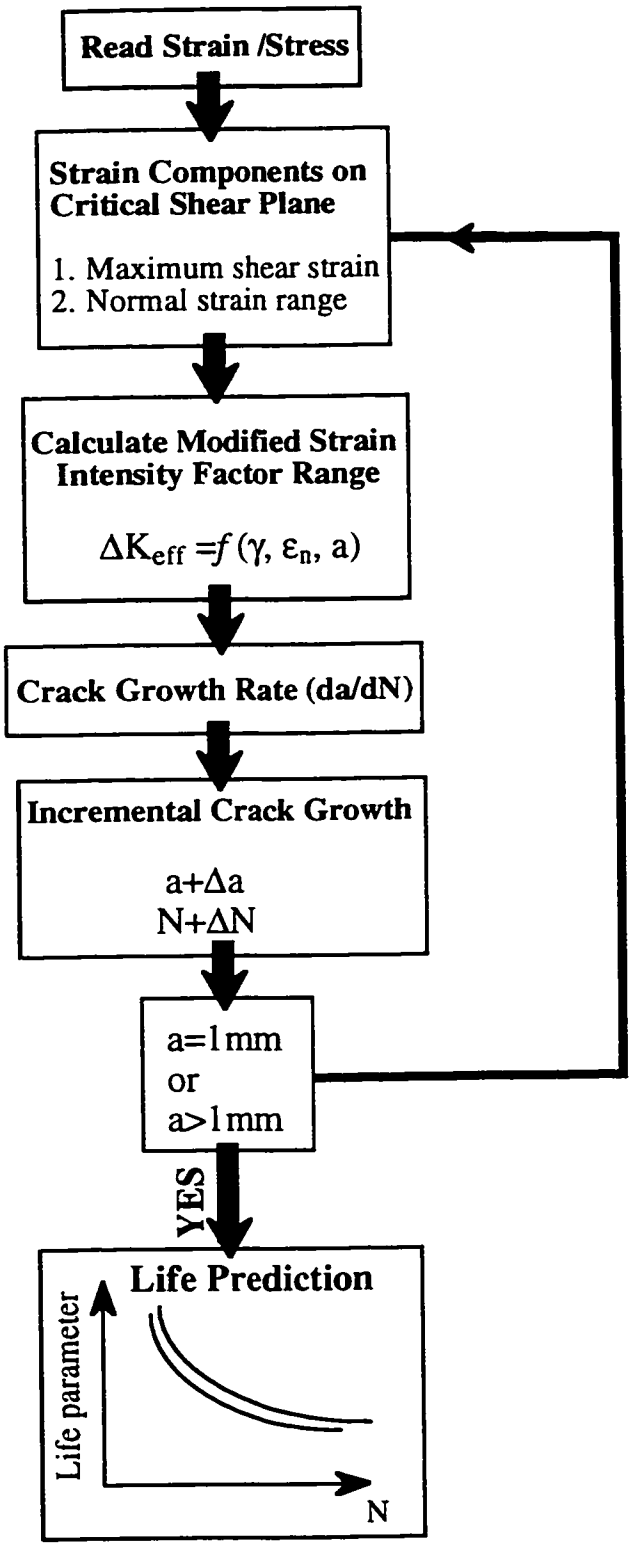

Fig 6.8 Fatigue life prediction algorithm.

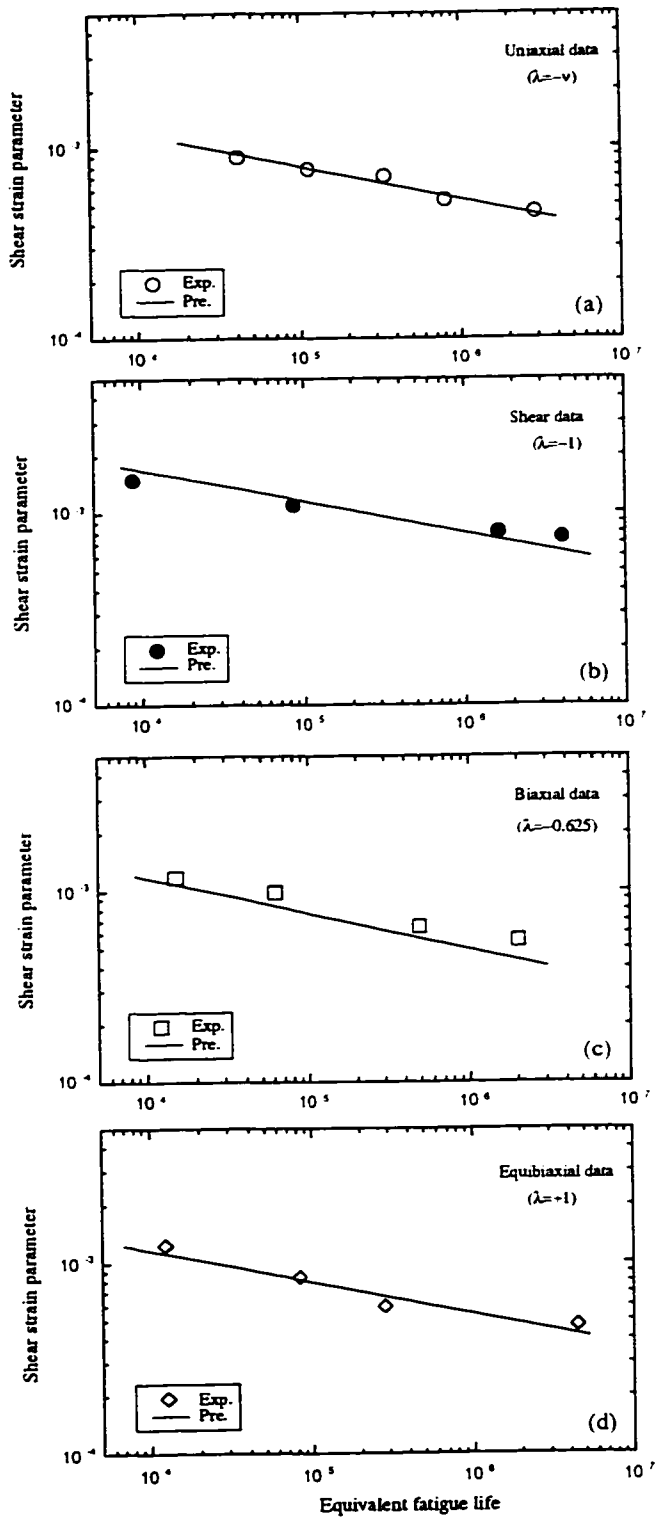

Fig 6.9 Fatigue life prediction based on the shear strain parameter for strain ratios of a) $\lambda=-\nu$, b) $\lambda=-1$, c) $\lambda=-0.625$, and d) $\lambda=+1$.

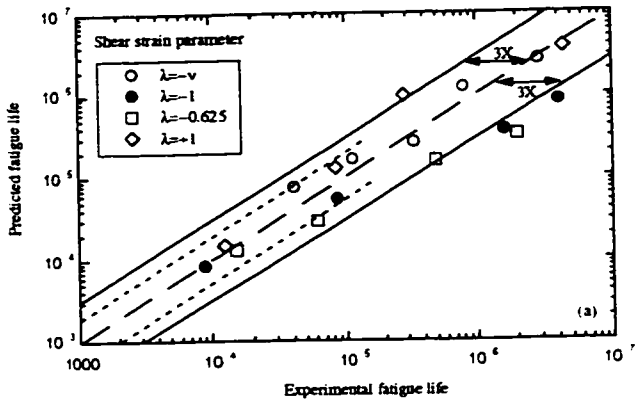

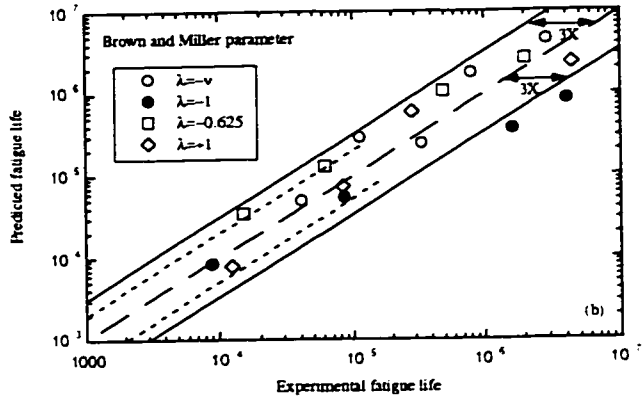

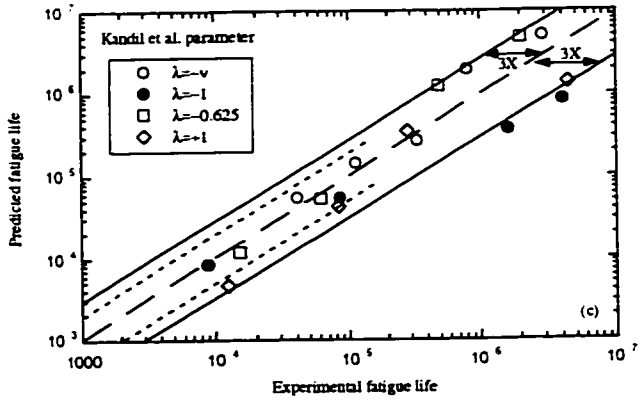

Fig 6.10 Predicted effective fatigue lives versus the experimental fatigue lives: a) the shear strain parameter, b) the Brown and Miller parameter, and c) the Kandil parameter.

6.4 Summary and Discussion

Most of the multiaxial life models [17-19] do not explain the physical phenomenon of crack initiation, crack growth, and failure mechanisms. However, the critical plane theory devotes specific attention to the orientation of small cracks in multiaxial fatigue. This theory asserts that the most critically damaged plane (crack initiation and early growth) is the one having the maximum shear strain amplitude. The use of this parameter is based on the premise that the normal stress or strain assists shear crack propagation by opening the crack, thereby reducing crack face asperity interaction. In this chapter an attempt was made to evaluate correlations of fatigue life data based on critical shear plane approaches for both constant amplitude loading and load histories containing periodic compressive overloads.

The fatigue lives obtained under constant amplitude loading (with closure) and various biaxial strain ratios were collapsed successfully onto one curve when they were evaluated based on the shear strain approach, the Brown and Miller parameter, the Kandil et al. parameter, and the Fatemi and Socie parameter. The Glinka et al. parameter showed a good correlation of fatigue life data under biaxial strain ratios of -1, -0.625, and +1 but data for a strain ratio of λ=-ν lay above the data for the other strain ratios.

Fully effective fatigue life data obtained for the periodic compressive overload tests were correlated reasonably well for strain ratios of -ν, -0.625, -1, and +1 by the shear strain and the Brown and Miller approaches for lives less than 10^6 cycles. The Kandil et al. parameter and the Fatemi and Socie parameter showed better correlations over the whole of the LCF and HCF regions. The Glinka et al. parameter correlated the effective life data within a scatter of ± 3.

The effective strain intensity factor range was modeled based on the critical plane parameters. The components of the strain intensity factor range model consist of the maximum shear strain range and the normal strain range acting on the critical plane.

The results of effective fatigue life predictions obtained from the various ΔK_{eff}-da/dN curves showed that the shear strain parameter, the Brown and Miller parameter, and the Kandil et al. parameter correlated the predicted and experimental effective life data within a factor of ± 2 for the low cycle fatigue regime, $10^3 < N \leq 10^5$, and a factor of ± 3 for high cycle fatigue regime, $N > 10^5$.

CHAPTER 7

Conclusions and Recommendations

Fatigue crack growth and closure mechanisms of SAE 1045 Steel under various biaxial loading conditions have been studied. The effect of periodic compressive overloads in reducing fracture surface asperity height, asperity induced crack closure and fatigue crack growth have been investigated and conclusions have already been presented in the summary at the end of each chapter.

The following presents a review of the major conclusions drawn from this study:

1. To achieve the objective of this study, a novel technique was developed in order to detect and characterize the short fatigue cracking behaviour from crack initiation in a slip band under uniaxial and various biaxial fatigue loading conditions. The confocal scanning laser microscopy (CSLM) image processing technique provided a quantitative study of crack length, crack depth, crack front shape and a 3D image of the crack profile with a high resolution and an accuracy about ± 0.50 μm. Fracture surface roughness height and shape measurements were performed using CSLM for constant amplitude and periodic compressive overloading conditions. This provided a quantitative study of the fracture

surface roughness changes due to periodic compressive overloads and related these changes to crack closure and crack growth.

2. Four biaxial principal strain ratios (hoop strain/axial strain) were used λ=-1 (pure shear loading), λ=-ν (uniaxial loading), biaxial strain ratio of λ=-0.625, and λ=+1 (equibiaxial loading).

In pure shear loading (λ=-1), surface cracks initially nucleated on slip bands at 45° to the axis of the specimen which coincides with the plane of maximum shear strain. Growth on the shear planes (microcracks) into the specimen occupied up to 90% of the fatigue life during which time the surface length of the microcracks remained nearly constant. It was found that at about 90% of the fatigue life the aspect ratio a/c reached unity (semi-circular), and the shear cracks started growing in the length direction as well as into the material. Failure then occurred by a rapid linking of microcracks at the end of a test.

In uniaxial loading (λ=-ν), cracks initiated along the maximum shear plane at 45° to the surface of the specimen (Stage I growth) and failure then took place by Stage II growth perpendicular to the axis of the specimen. No crack linking was observed in the uniaxial fatigue tests.

In tests with a biaxial strain ratio of λ=-0.625, crack initiation and early damage development were observed along planes of maximum shear strain at about 40°-45° to the axial direction of the tubular specimen. Microcracks initiated at various positions in the gage length of the specimen. The behavior of microcracks for this strain ratio was similar to that of the microcracks initiated under pure shear loading. Fatigue failure occurred by a rapid linking up of microcracks at the end of a test.

In equibiaxial fatigue loading (λ=+1), cracks nucleated on the two maximum shear planes parallel and perpendicular to the specimen axis and propagated into the specimen on planes at 45° to the specimen surface. In equibiaxial fatigue loading, once a crack initiated, it grew in the length and depth directions until failure took place.

3. Confocal scanning laser microscopy (CSLM) and scanning electron microscopy (SEM) examinations of fracture surfaces revealed that periodic compressive overstrains flattened mismatch asperities near the crack tip. The height of the mismatch asperities on the crack fracture surface was reduced dramatically by the application of in-phase periodic compressive overstrains. The reduction in the height of these irregularities on the fracture surface was accompanied by the opening of the crack in the mouth and depth directions and an acceleration in the crack growth rate.

In the present study, a geometric model of the plastic deformation of the fracture surface asperities at the crack tip (under periodic compressive overloads) was developed for both uniaxial and biaxial shear loading conditions. This model assumes that the volume of initially cone-shaped asperities is conserved during plastic deformation by the compressive overloads. The model correlates the magnitude of the periodic compressive stress, the fracture surface asperity height and the plastically flattened area based on the CSLM measurement of the fracture surface asperities with a high resolution and accuracy.

4. The fatigue lives obtained under constant amplitude loading (with closure) and various biaxial strain ratios were collapsed successfully into one curve when they were evaluated based on the shear strain parameter, the Brown and Miller parameter, the Kandil et al. parameter, and the the Fatemi and Socie parameter. The Glinka et al. parameter showed a good correlation of fatigue life data under biaxial strain ratios of -1, -0.625, and +1, but with this parameter fatigue life data obtained under a strain ratio of λ=-v lay above the life data of the other strain ratios.

Fully effective fatigue life data obtained under periodic compressive overloads showed that effective strain-life data for the various strain ratios can be correlated reasonably well by the shear strain and the Brown and Miller approaches for lives up to 10^5 cycles. The Kandil et al. and the Fatemi and Socie parameters showed better correlations of effective fatigue life results over the whole life range (LCF and HCF regimes). The Glinka et al. parameter correlated the effective life data for the various strain ratios within a scatter of ± 3.

The effective strain intensity factor range was modeled based on the critical plane parameters. The components of the strain intensity factor range model consist of the maximum shear strain range and the normal strain range acting on the critical plane.

The results of effective fatigue life predictions obtained from the various ΔK_{eff}-da/dN curves showed that the shear strain parameter, the Brown and Miller parameter, and the Kandil et al. parameter correlated the predicted and experimental effective life data within a factor of ± 2 for the low cycle fatigue regime, $10^3 < N \leq 10^5$, and a factor of ± 3 for the high cycle fatigue regime, $N > 10^5$.

APPENDIX A

Fatigue Crack Shape Factor

Irwin [90] derived a K-factor for an embedded elliptical crack under uniform tension based on the stress field around an ellipsoidal cavity proposed by Green and Sneddon [91]

$$K = \frac{\sigma\sqrt{\pi a}}{\Phi}\,\Psi \qquad \text{(A-1)}$$

where Φ is the elliptic integral

$$\Phi = \int_0^{\pi/2}\left[1-\left(1-\left(\frac{a}{c}\right)^2\right)\mathrm{Sin}^2\varphi\right]^{1/2} d\varphi \qquad \text{(A-2)}$$

where φ is the angle in the parametric equation of an ellipse (see Fig A-1), the parameter Ψ is a function of aspect ratio (a/c) and angle φ and expressed as

$$\Psi = \left(\mathrm{Sin}^2\varphi + \left(\frac{a}{c}\right)^2 \mathrm{Cos}^2\varphi\right)^{1/4} \qquad \text{(A-3)}$$

Kassir and Sih [92] solved for the K-factor for a flat elliptical crack subjected to a shear loading

$$K_{Shear} = \frac{\tau\sqrt{\pi a}}{I\,\Psi}(1-\nu)\left(1-\left(\frac{a}{c}\right)^2\right)\mathrm{Sin}\,\varphi \qquad \text{(A-4)}$$

where the parameter I is a function of aspect ratio and Poisson's ratio and is expressed as

$$I = \left[\left(1-\left(\frac{a}{c}\right)^2\right)-\nu\right]\Phi + \nu\left(\frac{a}{c}\right)^2 L \qquad \text{(A-5)}$$

where L for shear loading is

$$L = \int_0^{\pi/2} \left[1 - \left(1 - \left(\frac{a}{c} \right)^2 \right) \mathrm{Sin}^2 \varphi \right]^{-1/2} d\varphi \qquad \text{(A-6)}$$

Geometry factors F_I for cracks under Mode I loading and the geometry factor F_{II} for a crack under Mode II loading were obtained respectively from eqn (A-1) and eqn (A-4) as

$$F_I = \frac{\Psi}{\Phi} \qquad \text{(A-7a)}$$

$$F_{II} = \frac{(1-\nu)}{I\,\Psi} \left(1 - \left(\frac{a}{c} \right)^2 \right) \mathrm{Sin}\, \varphi \qquad \text{(A-7b)}$$

Socie et al. [80] and Sehitoglu et al. [93] used the same analysis for the strain intensity factor range of small cracks under tension, torsion and mixed mode loading conditions.

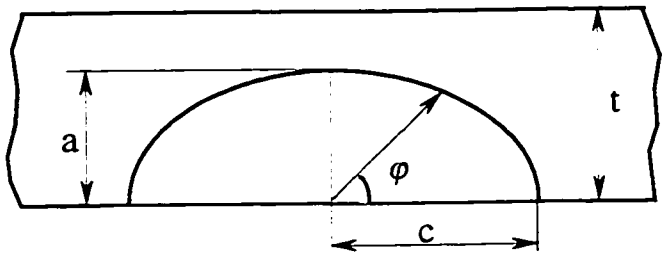

Fig A-1 Geometry of semi-elliptical crack.

The variation of geometry factors F_I and F_{II} with the aspect ratio (a/c) under tensile and shear Modes, respectively, are represented in Fig A-2.

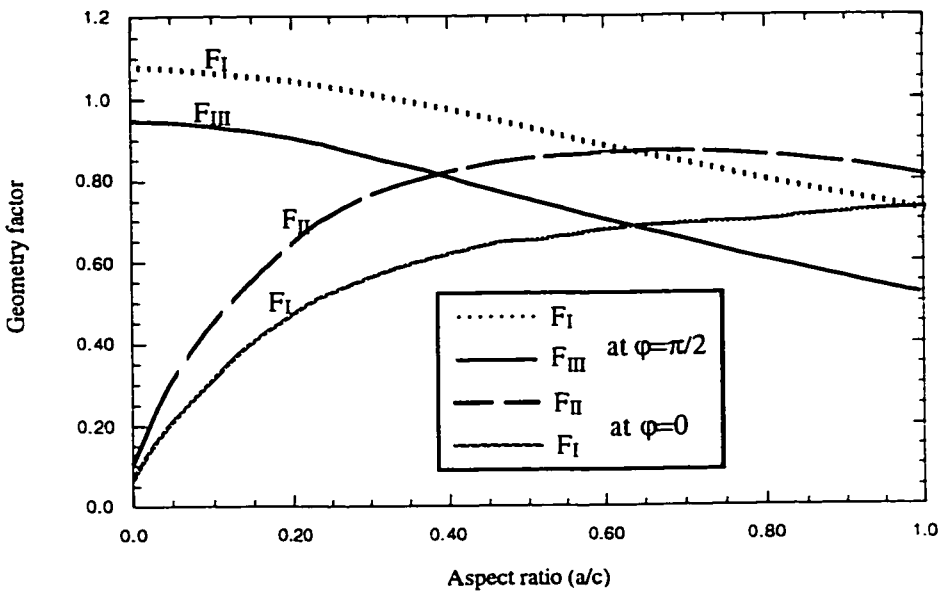

Fig A-2 Variation of geometry factors F_I and F_{II} as a function of aspect ratio (a/c) [80,93].

The state of strain is represented in figures A-3a and A-3b for shear loading (λ=-1) and other strain ratios of λ=-ν, and +1, respectively.

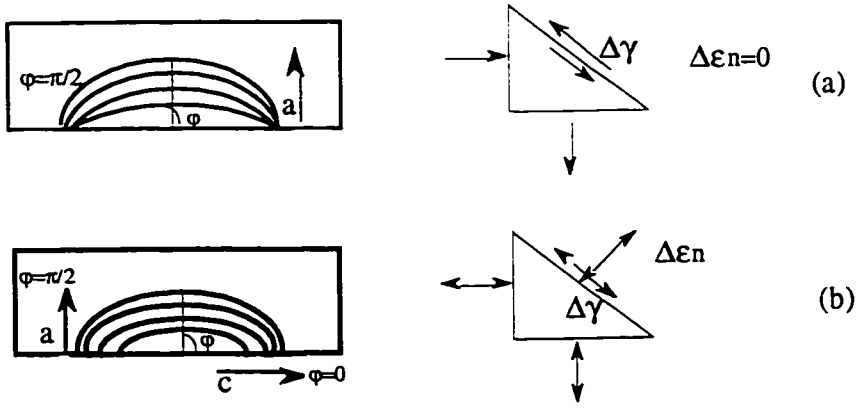

Fig A-3 The states of strain for a) shear loading(λ=-1), and b) strain ratios of λ=-ν, and +1

APPENDIX B

Properties of SAE 1045 Steel

Chemical Composition (weight %):

0.46 C, 0.17 Si, 0.81 Mn, 0.027 P, 0.023 S, and the remainder Fe.

Mechanical Properties	**Magnitude**	**Units**
Modulus of Elasticity	206	GPa
Cyclic Yield Stress (0.2% offset)	448	MPa
Ultimate Tensile Stress	745	MPa
True Fracture Stress	1047	MPa
Brinell Hardness	200	HB
Average Grain Size	50	μm

Fatigue Properties

Tensile Fatigue Limit Stress (R=-1)	300	MPa
Shear Fatigue Limit Strain (R=-1)	0.27	%
Cyclic Strain Hardening Coefficient	1159.6	MPa
Cyclic Strain Hardening Exponent	0.28	---

APPENDIX C

FORTRAN Programming of a Life Prediction Model

This appendix contains the program listing for a life prediction model.

1. A fracture mechanics approach is used. the model follows material deformation, and crack growth on a cycle-by-cycle basis.

2. The crack closure free growth curve and cyclic stress-strain curve are required to run the program.

3. The stress-strain analysis section of the program is based on the critical plane approach, the type of loading, and strain ratio used. The present hard copy contains the uniaxial case and the Brown and Miller approach. The strain-stress analysis sections for the other parameters and various strain ratios are given at the end of the program.

4. Material data for SAE 1045 steel are included in the program although the data can be altered for other materials.

5. A simple MATLAB program is used to calculate the principal stresses required for the input file of the FORTRAN program.

```
C   SYMBOL        VARIABLE DESCRIPTION
C   ------  ----------------------------------------
C     L      ACTUAL CRACK LENGTH (m)
C     AI     INITIAL FLAW SIZE, (m)
C     AF     FAILURE FLAW SIZE, (m)
C     KTH    THRESHOLD INTENSITY FACTOR RANGE, MPa*M^(1/2)
C     KM1    MAXIMUM CHANGE IN 'K' AT START OF INCREMENT(TENSION ONLY)
C     KM2    MAXIMUM CHANGE IN 'K' AT END OF INCREMENT(TENSION ONLY)
C     KMAX1  MAXIMUM STRESS INTENSITY FACTOR, MPa*M^(1/2)
C     KMAX2  MAXIMUM STRESS INTENSITY FACTOR, MPa*M^(1/2)
C     RATE   AVG. RATE OF GROWTH OF CRACK (M/CYCLE)
C     DL     INCREMENTAL CRACK GROWTH LENGTH
C     CYCLE  REAL NUMBER OF CYCLES
C     STRESS NOMINAL STRESS RANGE
C     Q      SURFACE CONCENTRATOR, AFUNCTION OF STRESS RATIO, R
      REAL L, RATE, CYCLE, DL, KM1, KM2, LCUT, KOL, KP,DEOL
      REAL AF, PI, ELG, KN2, C1, C2, G
      REAL STRAIN, STRAINE, STRAINP, STRESS1, STRESS2,  DSTRAIN
     &  ,EOPSM, NUEFF, SSTRAIN, AHMAD, BMPAR
      REAL STRAIN1, STRAIN2, STRAIN3, KIC, KFRA, STR, NDSTRAIN
      REAL STROL, NSTROL, SOPN, A, S2, NFEQ,EMAXOL
      INTEGER IERR
C     LOGICAL PAST
      ELG = 2.718281828
      PI  = 3.1416
C     WIDTH = 12.5E-3
```

```
      KIC = 150.00
C --- Open INPUT file.
      OPEN(10,IOSTAT=IOS,FILE="inputol.dat",STATUS="OLD",ERR=9000)
C --- Open output file.
      OPEN(20,IOSTAT=IOS,FILE="GROWTH.DAT",STATUS="NEW")
C --- READ IN DATA
C       READ(10,*,END=220) SOL
C     SOL=320 (stress range), NFOL=11168
      READ(10,*) DEOL
C   INITIALIZE Constants
       AF =20.0E-3
       E = 206000
       G = 79230.77
       Q = 5.3
       NFOL=11168
  5   CONTINUE
C --- Get input. STRESS NET = NOMINAL STRESS RANGE OF SMALL CYCLES
C             STRESS  = GROSS SECTION STRESS
C             L = 3e-6
      READ(10,*,END=220) STRAIN1,  STRESS1
C             Stress and Strain Analysis
      STRAINE= STRESS1/E
      STRAINP= STRAIN1-STRAINE
      NUEFF= ((0.30*STRAINE)+(0.50*STRAINP))/(STRAINE+STRAINP)
      STRAIN2= -NUEFF* STRAIN1
      NDSTRAIN= (STRAIN1-(NUEFF*STRAIN1))
      SSTRAIN = (STRAIN1+(NUEFF*STRAIN1))/2
```

```
C         AHMAD = 1+(0.15*NDSTRAIN/SSTRAIN)
C        BMPAR = AHMAD*(SSTRAIN+(0.60*NDSTRAIN))
        BMPAR = (SSTRAIN+(0.60*NDSTRAIN))
        DSTRAIN=STRAIN1-STRAIN2
C --- Initialize data.
         L     = 3.0E-6
        CYCLE  = 0.
C 100   DL    = .01*(L)
100       CONTINUE
C --- CALCULATE Q
        FREQ =INT(3.0e-5*DSTRAIN **(-2.82))
        DO 300 M=1 , FREQ, 10
C         N = M
C         PRINT *, 'FREQ=', FREQ
        Q1 = 1 + Q * ELG**(ALPHA*L)
C        PRINT *,'Q1=', Q1
122    CONTINUE
C       DETERMINING OPENING STRESSES FOR SMALL CYCLES AND OVERLOADS
C        EMAXOL=DEOL/2
C        EMINOL=-EMAXOL
C        EOPOL=0.0*EMAXOL*(1-(EMAXOL/0.0045)**2)+1.0*EMINOL
C        IF (EOPOL .LT. EMINOL) THEN
C        DEEFFOL=DEOL
C         ELSE
C        DEEFFOL=EMAXOL-EOPOL
C         END IF
```

```
C       Correction for notch plasticity
C        CALL CYCLIC (SEFFSM, STRAIN, NERR)
C        IF (NERR .EQ. 1) STRAIN=SEFFSM
C        IF (NERR .EQ. -1) STOP 'ERROR'
C        CALL CYCLIC (SEFFOL, STRAINOL, NERR)
C        IF (NERR .EQ. 1) STRAINOL=SEFFOL
C        IF (NERR .EQ. -1) STOP 'ERROR'
C --- Get Shape Factor
C         IF( STRESS1 .LE. 100) THEN
C          F = 0.55
C         ELSE IF ( STRESS1 .GT. 300) THEN
C          F =1.12
C         ELSE
C          F = 0.74
C         END IF
          F=0.257+(491*BMPAR)
C --- Calculate intensity factors.
C        KM1 =(2.60*0.6*DNSTRAIN+SSTRAIN)*G*2 * F
C     &   * AHMAD* Q1 * SQRT(L*PI)
        KM1 =(2.60*0.6*DNSTRAIN+SSTRAIN)*G*2*F
     &    *Q1*SQRT(L*PI)
        KOL = DEOL*E * F * Q1 * SQRT(L*PI)
C        PRINT *, 'KM1,KOL=', KM1,   KOL
         KFRA= EMAXSM*E*F*SQRT(L*PI)
         IF (KFRA .GE. KIC) GOTO 151
```

```
C --- Calculate growth rates at extremes of increment.
      IERR = 0
      CALL GRATE(KM1, XRATE, IERR)
       RATE1 = XRATE
C      PRINT *, 'RATE1=', RATE1
      CALL GRATE(KOL, XRATE, JERR)
       RATE2 = XRATE
      IF (IERR .EQ. 1 ) THEN
C          CYCLE = 1.0E+8
C          GOTO  151
           RATE1 = 0.00
      ENDIF
      IF (IERR .EQ. -1) THEN
          PRINT *, 'KM1 = ', KM1
          WRITE(6,*) 'ERROR IN GROWTH RATE'
          STOP
      ENDIF
C --- Increment crack length
       DL = 10* RATE1
       L    = L+DL
       CYCLE = CYCLE + 10
C       PRINT *, 'L = ',L
C --- Check for failure.
C       WRITE(20,*) 'L= ',L
      IF (L. LE. AF) GO TO 300
      IF (L. GT. AF) GO TO 151
300   CONTINUE
```

```
      DL = 1* RATE2
C       PRINT *, 'DL=', DL
      L = L + DL
      CYCLE = CYCLE + 1
      IF(L .LE. AF) GO TO 100
C       PRINT *, 'l=', L
C --- If failed, end here.
151    CONTINUE
C       PRINT *, 'FREQ=', FREQ
     NFEQ=(CYCLE-(CYCLE/(FREQ+1)))/(1-((CYCLE/(FREQ+1))/NFOL))
      WRITE(20,*) BMPAR, NINT(CYCLE), L
      PRINT *, 'BMPAR=', BMPAR, 'CYCLE=' ,NINT(CYCLE),
     &   'CRACK=' , L
      GOTO 5
C --- No more specimens.
220    CONTINUE
      CLOSE(10)
      CLOSE(20)
C --- Format statements.
110    FORMAT( G9.1,1X,F8.6,1X,2(G9.3,1X),3(F5.3,1X))
120    FORMAT(' STRESS = ',F6.1,' STRAIN =', F7.5,
     *      'FREQ= ', F7.2,' Nf= ',I12, 'NFEQ=', I12)
      STOP
9000   WRITE(6,*) ' *** ERROR **** CAN'T FIND INPUT FILE !'
      END
```

```
SUBROUTINE GRATE( X, Y, NER)
REAL X,Y
INTEGER NER
Y = 0
NER = 0
X1 = 2.40
X2 = 2.80
X3 = 4.0
X4 = 4.80
X5 = 5.70
X6 = 6.90
X7 = 9.80
Y1 = 1.20E-12
Y2 = 1.7E-11
Y3 = 2.50E-10
Y4 = 1.2E-9
Y5 = 3.00E-9
Y6 = 1.1E-8
Y7 = 1.0E-7
IF(X .LE. X1) THEN
 NER = 1
 RETURN
ENDIF
IF(X1 .LT. X .AND. X .LE. X2) THEN
 RISE = ALOG10(Y2) - ALOG10 (Y1)
 RUN =  ALOG10(X2) - ALOG10(X1)
  SLOPE = RISE/RUN
```

```
RISE = (ALOG10(X)-ALOG10(X1)) * SLOPE
 YP = ALOG10(Y1) + RISE
ELSE IF(X2 .LT. X .AND. X .LE. X3) THEN
 RISE = ALOG10(Y3) - ALOG10 (Y2)
 RUN =  ALOG10(X3) - ALOG10(X2)
  SLOPE = RISE/RUN
 RISE = (ALOG10(X)-ALOG10(X2)) * SLOPE
  YP = ALOG10(Y2) + RISE
ELSE IF(X3 .LT. X .AND. X .LE. X4) THEN
 RISE = ALOG10(Y4) - ALOG10 (Y3)
 RUN =  ALOG10(X4) - ALOG10(X3)
  SLOPE = RISE/RUN
 RISE = (ALOG10(X)-ALOG10(X3)) * SLOPE
  YP = ALOG10(Y3) + RISE
ELSE IF(X4 .LT. X .AND. X .LE. X5) THEN
 RISE = ALOG10(Y5) - ALOG10 (Y4)
 RUN =  ALOG10(X5) - ALOG10(X4)
  SLOPE = RISE/RUN
 RISE = (ALOG10(X)-ALOG10(X4)) * SLOPE
  YP = ALOG10(Y4) + RISE
ELSE IF(X5 .LT. X .AND. X .LE. X6) THEN
 RISE = ALOG10(Y6) - ALOG10 (Y5)
 RUN =  ALOG10(X6) - ALOG10(X5)
  SLOPE = RISE/RUN
 RISE = (ALOG10(X)-ALOG10(X5)) * SLOPE
  YP = ALOG10(Y5) + RISE
ELSE IF(X6 .LT. X .AND. X .LE. X7) THEN
```

```
      RISE = ALOG10(Y7) - ALOG10 (Y6)
      RUN =  ALOG10(X7) - ALOG10(X6)
       SLOPE = RISE/RUN
      RISE = (ALOG10(X)-ALOG10(X6)) * SLOPE
       YP = ALOG10(Y6) + RISE
     ELSE IF(X7 .LT. X ) THEN
       RISE = ALOG10(Y7) - ALOG10 (Y6)
       RUN =  ALOG10(X7) - ALOG10(X6)
       SLOPE = RISE/RUN
       RISE = (ALOG10(X)-ALOG10(X7)) * SLOPE
       YP = ALOG10(Y7) + RISE
      ELSE
       NER = -1
       RETURN
      ENDIF
      Y =  10**YP
C      WRITE(6,*) 'L = ',L
C      WRITE(6,*) 'X = ',X
C      WRITE(6,*) 'Y = ',Y
C      WRITE(6,*) "RISE=,RUN=,SLOPE=,YP=",RISE,RUN,SLOPE,YP
      RETURN
C      WRITE(6,*) 'L = ',L
      END
```

STRAIN-STRESS ANALYSIS FOR VARIOUS PARAMETERS AND STRAIN RATIOS

C----- **The shear strain parameter-Uniaxial loading case**

```
      READ(10,*,END=220) STRAIN1, STRESS1
      STRAINE= STRESS1/E
      STRAINP= STRAIN1-STRAINE
      NUEFF= ((0.30*STRAINE)+(0.50*STRAINP))/(STRAINE+STRAINP)
      STRAIN2= -NUEFF* STRAIN1
      NDSTRAIN= (STRAIN1-(NUEFF*STRAIN1))
      SSTRAIN = (STRAIN1+(NUEFF*STRAIN1))/2
      AHMAD = 1+(0.60*NDSTRAIN/SSTRAIN)
C     SHPAR = SSTRAIN+(0.60*NDSTRAIN)
      SHPAR = SSTRAIN
      DSTRAIN=STRAIN1-STRAIN2
```

C----- **The shear strain parameter-Biaxial loading case**

```
      READ(10,*,END=220) STRAIN1, STRESS1, STRESS2
      STRAIN2 = -0.625*STRAIN1 or (STRAIN2 = -1*STRAIN1) or (STRAIN2 =STRAIN1)
      STRAINE1 = STRESS1/E1
      STRAINP1 = STRAIN1-STRAINE1
      STRAINE2 = STRESS2/E2
      STRAINP2 = STRAIN2-STRAINE2
```

C----- Effective Poisson's ratio and Max. Shear Strain Plane Calculation

```
      PART1= (0.35*(STRAIN1+STRAIN2))+(-0.20*(STRAINE1+STRAINE2))
      PART2= (0.70*(STRAIN1+STRAIN2))+(-0.20*(STRAINE1+STRAINE2))
      NUEFF = PART1/PART2
      STRAIN3 = (-NUEFF/(1-NUEFF))*(STRAIN1+STRAIN2)
```

```
      IF (STRAIN3 .LE. STRAIN2) THEN
      NDSTRAIN= (STRAIN1+STRAIN3)
       SSTRAIN = (STRAIN1-STRAIN3)/2
       ELSE
       NDSTRAIN = (STRAIN1+ STRAIN2)
       SSTRAIN  = (STRAIN1-STRAIN2)/2
       END IF
```

C----- **The Brown and Miller parameter-Uniaxial loading case**

```
       READ(10,*,END=220) STRAIN1,  STRESS1
       STRAINE= STRESS1/E
       STRAINP= STRAIN1-STRAINE
       NUEFF= ((0.30*STRAINE)+(0.50*STRAINP))/(STRAINE+STRAINP)
       STRAIN2= -NUEFF* STRAIN1
       NDSTRAIN= (STRAIN1-(NUEFF*STRAIN1))
       SSTRAIN = (STRAIN1+(NUEFF*STRAIN1))/2
C      AHMAD = 1+(0.15*NDSTRAIN/SSTRAIN)
C      BMPAR = AHMAD*(SSTRAIN+(0.60*NDSTRAIN))
       BMPAR = (SSTRAIN+(0.60*NDSTRAIN))
       DSTRAIN=STRAIN1-STRAIN2
```

C----- **The Brown and Miller parameter-Biaxial loading case**

```
       READ(10,*,END=220) STRAIN1, STRESS1, STRESS2
       STRAIN2 = -0.625*STRAIN1 or (STRAIN2 = -1*STRAIN1) or (STRAIN2 =STRAIN1)
       STRAINE1 = STRESS1/E1
```

```
      STRAINP1 = STRAIN1-STRAINE1

      STRAINE2 = STRESS2/E2

      STRAINP2 = STRAIN2-STRAINE2

C-----  Effective Poisson's ratio and Max. Shear Strain Plane Calculation

      PART1= (0.35*(STRAIN1+STRAIN2))+(-0.20*(STRAINE1+STRAINE2))

      PART2= (0.70*(STRAIN1+STRAIN2))+(-0.20*(STRAINE1+STRAINE2))

      NUEFF = PART1/PART2

      STRAIN3 = (-NUEFF/(1-NUEFF))*(STRAIN1+STRAIN2)

      IF (STRAIN3 .LE. STRAIN2) THEN

      NDSTRAIN= (STRAIN1+STRAIN3)

      SSTRAIN = (STRAIN1-STRAIN3)/2

      ELSE

      NDSTRAIN = (STRAIN1+ STRAIN2)

      SSTRAIN  = (STRAIN1-STRAIN2)/2

      END IF
```

```
C-----  The Kandil et al. parameter-Uniaxial loading case

      READ(10,*,END=220) STRAIN1,  STRESS1

      STRAINE= STRESS1/E

      STRAINP= STRAIN1-STRAINE

      NUEFF= ((0.30*STRAINE)+(0.50*STRAINP))/(STRAINE+STRAINP)

      STRAIN2= -NUEFF* STRAIN1

      NDSTRAIN= (STRAIN1-(NUEFF*STRAIN1))

      SSTRAIN = (STRAIN1+(NUEFF*STRAIN1))/2

C     AHMAD = 1+(0.12*NDSTRAIN/SSTRAIN)

C     KANPAR = AHMAD*((SSTRAIN**.55)+(0.20
```

```
C     &    *(NDSTRAIN**0.55)))**1.82
          KANPAR =((SSTRAIN**0.55)+(0.20
        &    *(NDSTRAIN**0.55)))**1.82
          DSTRAIN=STRAIN1-STRAIN2
```

C----- **The Kandil et al. parameter-Biaxial loading case**

```
          READ(10,*,END=220) STRAIN1, STRESS1, STRESS2
          STRAIN2 = -0.625*STRAIN1 or (STRAIN2 = -1*STRAIN1) or (STRAIN2 =STRAIN1)
          STRAINE1 = STRESS1/E1
          STRAINP1 = STRAIN1-STRAINE1
          STRAINE2 = STRESS2/E2
          STRAINP2 = STRAIN2-STRAINE2
C-----    Effective Poisson's ratio and Max. Shear Strain Plane Calculation
          PART1= (0.35*(STRAIN1+STRAIN2))+(-0.20*(STRAINE1+STRAINE2))
          PART2= (0.70*(STRAIN1+STRAIN2))+(-0.20*(STRAINE1+STRAINE2))
          NUEFF = PART1/PART2
          STRAIN3 = (-NUEFF/(1-NUEFF))*(STRAIN1+STRAIN2)
          IF (STRAIN3 .LE. STRAIN2) THEN
          NDSTRAIN= (STRAIN1+STRAIN3)
          SSTRAIN = (STRAIN1-STRAIN3)/2
           ELSE
          NDSTRAIN = (STRAIN1+ STRAIN2)
          SSTRAIN  = (STRAIN1-STRAIN2)/2
           END IF
```

MATLAB PROGRAM FOR THE CALCULATION OF PRINCIPAL STRESSES

```
function [f] = f(x)

f(1)=6.3e-6*x(1)-1.456e-6*(x(1)+x(2))+(1.5*(x(1)-.333*(x(1)+x(2))))*2.63 e-9*sqrt((.5*((x(1)-
x(2))^2+x(1)^2+x(2)^2)^1.22)± Axial strain;

f(2)=6.3e-6*x(2)-1.456e-6*(x(1)+x(2))+(1.5*(x(2)-.333*(x(1)+x(2))))*2.63e-9*sqrt((.5*((x(1)-
x(2))^2+x(1)^2+x(2)^2)^1.22)± Hoop strain;
```

Where x(1) and x(2) are the axial and hoop stresses.

APPENDIX D

Derivation of Equations used in this study

D-1. Equivalent number of small cycles in periodic compressive overload histories

$$D_T = D_{SM} + D_{OL} \tag{D1-1}$$

At failure;

$$\sum D_T = 1 \tag{D1-2}$$

$$D_{SM} = 1 - D_{OL} \tag{D1-3}$$

$$D_{SM} = \frac{n_{SM}}{N_{SM}} \tag{D1-4}$$

$$D_{OL} = \frac{n_{OL}}{N_{f,OL}} \tag{D1-5}$$

$$N_{eq.\,SM} = \frac{n_{SM}}{D_{SM}} \tag{D1-6}$$

$$n_{SM} = N_T - \frac{N_T}{n} = N_T\left(1 - \frac{1}{n}\right) \tag{D1-7}$$

$$D_{SM} = 1 - D_{OL} = 1 - \frac{n_{OL}}{N_{f,\,OL}} = 1 - \left(\frac{N_T}{n\,N_{f,\,OL}}\right) \tag{D1-8}$$

Therefore,

$$N_{eq.\,SM} = \frac{N_T\left(1 - \frac{1}{n}\right)}{1 - \left(\frac{N_T}{n\,N_{f,\,OL}}\right)} \tag{D1-9}$$

D-2. Hoop strain measured using radial extensometer on the thin-walled tubular specimen

Figure D-2 presents schematically the tubular specimen before and after internal pressure.

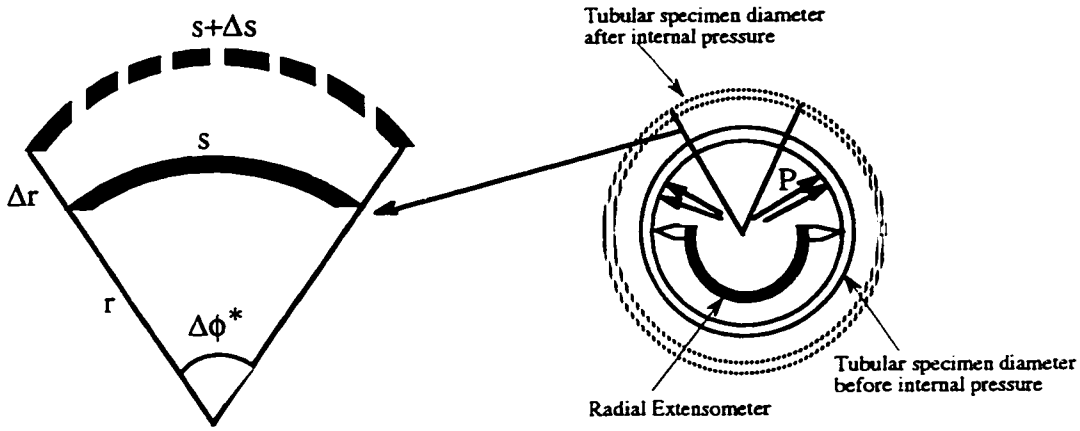

Fig. D-2 Schematic presentation of the diameter of a thin-walled tubular specimen before and after internal pressure applied.

$$Hoop\ strain = \frac{\Delta s}{s} \tag{D2-1}$$

$$s = r\Delta\phi^{*} \tag{D2-2}$$

$$s + \Delta s = (r + \Delta r)\,\Delta\phi^{*} \tag{D2-3}$$

$$\Delta s = r\Delta\phi^{*} + \Delta r\,\Delta\phi^{*} - s \tag{D2-4}$$

$$\Delta s = r\Delta\phi^{*} + \Delta r\,\Delta\phi^{*} - r\Delta\phi^{*} = \Delta r\,\Delta\phi^{*} \tag{D2-5}$$

$$Hoop\ strain = \frac{\Delta s}{s} = \frac{\Delta r}{r} \tag{D2-6}$$

D-3. Coefficients used for ΔK_{eff} models consist of $\Delta\gamma$ and $\Delta\varepsilon_n$ acting on maximum shear plane

Brown and Miller Parameter

From eqn (1.2)

$$\gamma_{max} + 0.3\Delta\varepsilon_n = \text{Constant} \qquad \text{(D3.1-1)}$$

$$\Delta K^{BM}_{eff} = 0.3QF_I\, E\, \Delta\varepsilon_n \sqrt{\pi a} + QF_{II}\, G\, \Delta\gamma\sqrt{\pi a} \qquad \text{(D3.1-2)}$$

By substituting shear modulus $G = \dfrac{E}{2(1+\nu)}$ in to eqns (D3.1-1) and (D3.1-2),

$$\Delta K^{BM}_{eff} = QF_{II}\, G\, \Delta\gamma\sqrt{\pi a} + 0.3QF_I\, (2.6G)\, \Delta\varepsilon_n \sqrt{\pi a} \qquad \text{(D3.1-3)}$$

$$\Delta K^{BM}_{eff} = Q\, G(F_{II}\Delta\gamma + 0.78F_I\, \Delta\varepsilon_n)\sqrt{\pi a} \qquad \text{(D3.1-4)}$$

Kandil et al. Parameter

From eqn (1.3);

$$\bar{\gamma} = 2\left[\left(\frac{\gamma_{max}}{2}\right)^{\kappa} + S\,\varepsilon_n{}^{\kappa}\right]^{\frac{1}{\kappa}} \qquad \text{(D3.2-1)}$$

The constants κ and S obtained by solving equations (D3.2-2)

$$S = \frac{1}{F^{*}_{(\lambda=-\nu)}}\left[\left(\frac{\gamma_{p.(\lambda=-1)}}{\gamma_{p.(\lambda=+1)}}\right)^{\kappa} - 1\right]$$

$$S = \frac{1}{F^{*}_{(\lambda=+1)}}\left[\left(\frac{\gamma_{p.(\lambda=-1)}}{\gamma_{p.(\lambda=+1)}}\right)^{\kappa} - 1\right] \qquad \text{(D3.2-2)}$$

where F^{*} is the biaxial factor and is defined as

$$F^{*} = \left[\frac{(1-\mu)}{\sqrt{\lambda^{*2} + (1-\mu)^2}}\right]^{\kappa} \qquad \text{(D3.2-3)}$$

where μ is a constant equal to 0.50, and λ^* is the ratio of shear strain to normal strain.

The constants S and κ found to be 0.20 and 0.50, respectively.

By substituting constants S and κ into the Kandil et al. parameter, the effective strain intensity factor range can be written as

$$\Delta K^{\kappa}_{eff} = Q\,G\left[F_{II}\,(\Delta\gamma)^{0.5} + 0.73\,F_{I}(\Delta\varepsilon_{n})^{0.5}\right]^{2}\sqrt{\pi\,a} \qquad (6.6c)$$

D-4. Derivation of effective Poisson's ratio under biaxial loading state

The radial strain is given as

$$\varepsilon_r = \frac{-\nu^*}{1-\nu^*}(\varepsilon_a + \varepsilon_h) \tag{D4-1}$$

The effective Poisson's ratio from eqn (D4-1) is

$$\nu^* = \frac{\varepsilon_r}{\varepsilon_r - (\varepsilon_a + \varepsilon_h)} \tag{D4-2}$$

The total radial strain can be decomposed to elastic and plastic parts as

$$\varepsilon_r = \varepsilon^e{}_r + \varepsilon^p{}_r \tag{D4-3a}$$

where radial elastic and plastic strain components are

$$\varepsilon^e{}_r = \frac{-\nu^e}{1-\nu^e}(\varepsilon^e{}_a + \varepsilon^e{}_h) \tag{D4-3b}$$

$$\varepsilon^p{}_r = \frac{-\nu^p}{1-\nu^p}(\varepsilon^p{}_a + \varepsilon^p{}_h) \tag{D4-3c}$$

Substituting eqns (D4-3b) and (D4-3c) into eqn (D4-3a), yields

$$\varepsilon_r = \frac{-\nu^e}{1-\nu^e}(\varepsilon^e{}_a + \varepsilon^e{}_h) + \frac{-\nu^p}{1-\nu^p}(\varepsilon^p{}_a + \varepsilon^p{}_h) \tag{D4-4}$$

By substituting eqn (D4-4) into eqn (D4-2), effective Poisson's ratio is obtained as

$$\nu^* = \frac{\dfrac{-\nu_e(1-\nu_p)(\varepsilon^e{}_a + \varepsilon^e{}_h) - \nu_p(1-\nu_e)(\varepsilon^p{}_a + \varepsilon^p{}_h)}{(1-\nu_e)(1-\nu_p)}}{\dfrac{-\nu_e(1-\nu_p)(\varepsilon^e{}_a + \varepsilon^e{}_h) - \nu_p(1-\nu_e)(\varepsilon^p{}_a + \varepsilon^p{}_h)}{(1-\nu_e)(1-\nu_p)} - (\varepsilon_a + \varepsilon_h)} \tag{D4-5}$$

Equation (D4-5) can be rewritten as

$$\nu^* = \frac{\nu_e(1-\nu_p)(\varepsilon^e{}_a + \varepsilon^e{}_h) + \nu_p(1-\nu_e)\,(\varepsilon^p{}_a + \varepsilon^p{}_h)}{\nu_e(1-\nu_p)\,(\varepsilon^e{}_a + \varepsilon^e{}_h) + \nu_p(1-\nu_e)\,(\varepsilon^p{}_a + \varepsilon^p{}_h) + (1-\nu_e)\,(1-\nu_p)\,(\varepsilon_a + \varepsilon_h)} \qquad \text{(D4-6)}$$

By replacing $(\varepsilon^p{}_a + \varepsilon^p{}_h) = (\varepsilon_a + \varepsilon_h) - (\varepsilon^e{}_a + \varepsilon^e{}_h)$ into eqn (D4-6), we have

$$\nu^* = \frac{[\nu_e(1-\nu_p) - \nu_p(1-\nu_e)](\varepsilon^e{}_a + \varepsilon^e{}_h) + \nu_p(1-\nu_e)\,(\varepsilon_a + \varepsilon_h)}{[\nu_e(1-\nu_p) + \nu_p(1-\nu_e)](\varepsilon^e{}_a + \varepsilon^e{}_h) + [\nu_p(1-\nu_e)(1-\nu_e)(1-\nu_p)](\varepsilon_a + \varepsilon_h)} \qquad \text{(D4-7)}$$

Equation (D4-7) can be simplified as

$$\nu^* = \frac{(\nu_e - \nu_p)(\varepsilon^e{}_a + \varepsilon^e{}_h) + \nu_p(1-\nu_e)(\varepsilon_a + \varepsilon_h)}{(\nu_e - \nu_p)(\varepsilon^e{}_a + \varepsilon^e{}_h) + (1-\nu_e)(\varepsilon_a + \varepsilon_h)} \qquad \text{(D4-8)}$$

Equation (D4-8) presents the effective Poisson's ratio under biaxial loading case. The effective Poisson's ratio derived in this section has been used in the biaxial fatigue life prediction program. This relation has been already presented in Ref. 94.

References

1. P. J. E. Forsyth (1961), Proc. Crack Propagation Symposium, Crafield, pp.76-94.
2. M. Sarfarazi and S. Ghosh (1987), Engng Fract. Mech., Vol.27, No.3, pp.257-267.
3. G. Venkataraman, T. Chung, Y. Nakasone, and T. Mura (1990), Acta Met. Mater., Vol. 38, No.1, pp.31-40.
4. G. Venkataraman, T. Chung, Y. Nakasone, and T. Mura (1991), Acta Met. Mater., Vol. 39, No.11, pp.2621-2638.
5. H. J. Gough (1939), Proc. ASTM, Vol.33, Part II, pp.3-14.
6. R. E. Peterson (1959), in: Metal Fatigue, G. Sines, and J. L. Waisman, Eds.,McGraw-Hill, New York, pp.68-86.
7. N. E. Dowling (1993), in: Mechanical Behaviour of Materials, Prentice Hall, New Jersey.
8. M. W. Brown and K. J. Miller (1973), Proceedings of the Institution Mechanical Engineering, Vol.187, pp.745-755.
9. M. W. Parson and K. J. Pascoe (1976), Material Science Engineering, Vol.22, pp.31-50.
10. J. A. Bannantine and D. F. Socie (1988), ASTM STP 942, H. D.Solomon, G.R. Halford, L.R. Kaisand, and B.N. Leis, Eds., American Society for Testing and Materials, Philadelphia, pp.899-921.
11. D. Socie (1993), ASTM STP 1191, D.L.McDowell, and R.Ellis, Eds., American Society for Testing and Materials, Philadelphia, pp.7-63.

12. M. W. Brown and K. J. Miller (1982), ASTM STP 770, C. Amzallag, B.Leis, and P.Rabbe, Eds., American Society for Testing and Materials, pp.482-499.

13. B. R. You, and S. B. Lee (1996), International Journal of Fatigue, Vol.18, No.4, pp.235-244.

14. E. H. Jordan (1982), in: Fatigue -Multiaxial Aspects, American Society of Mechanical Engineers, pp.507-518.

15. Y. S. Garud (1981), Journal of Testing Evaluation, Vol.9, pp.165-178.

16. Y. S. Garud (1979), Proc. Symp. on Methods for Predicting Materials Life in Fatigue, W.J. Ostergren and J.R. Whitehead, Eds., American Society of Mechanical Engineers, pp.246-264.

17. F. Ellyin and Kujawski (1993), ASTM STP 1191, D.L.McDowell, and R.Ellis, Eds., American Society for Testing and Materials, Philadelphia, pp.55-66.

18. F. Ellyin and Z. Xia (1993), ASME, J. Engng Mater. Tech., American Society of Mechanical Engineers, Vol. 115, pp.411.

19. F. Ellyin and K. Golos (1988), Trans. ASME, J. Engng Mater. Tech., American Society of Mechanical Engineers, Vol. 110, pp.63.

20. A. Fatemi and D. F. Socie (1988), Fatigue Fract. Engng Mater. Struct., Vol.11, No.3, pp.149-165.

21. W. N. Findley, J. J. Coleman, and B. C. Handley (1956), Proc. Conf. on the Fatigue of Metals, The Institution of Mechanical Engineers, New York, pp.150.

22. J. F. Flavenot, and N. Skalli (1989), in: Biaxial and Multiaxial Fatigue, Mechanical Engineering Publications, London, pp.355.

23. F. B. Stulen, and H. N. Cummings (1954), Proc.ASTM, vol.54, pp.822.

24. R. D. Lohr and E. G. Ellison (1980), Fatigue Fract. Engng Mater. Struct., Vol.3, pp.1-17.

25. F. A. Kandil, K. J. Miller, and M. W. Brown (1985), in: Multiaxial Fatigue, ASTM STP 853, pp.651-668.

26. D. F. Socie, and T. W. Shield (1984), Trans. ASME, J. Engng Mater. Tech., Vol.106, pp.227.

27. G. Glinka, G. Shen, and A. Plumtree (1995), Fatigue Fract. Engng Mater. Struct., Vol.18, pp.37-46.

28. O. M. Jadaan, and G. Boys (1995), Design Engineering Technical Conference, ASME, Vol.2, pp.61-72.

29. W. Elber (1971), in: Damage Tolerance in Aircraft Structures, ASTM STP 486, Philadelphia, pp.230-247.

30. N. Walker, and C. J. Beevers (1979), fatigue Fract. Engng Mater. Struct., Vol.1, pp.135-148.

31. S. Purushothaman and J. K. Tien (1979), Proc. BICSMAS Conf., P. Haasen, V. Gerold, and G. kostoz, Eds., Pergamon Press, New York, Vol.2, pp.1267.

32. K. Minakawa, and A. J. McEvily (1981), Scripta Metallurgica, Vol. 15, pp.633-636.

33. S. Suresh and R.O. Ritchie (1982), Metal. Trans. A, Vol.13, pp.1627.

34. W. L. Morris, M. R. James, and O. Buck (1983), Engng Fract. Mech., Vol.18, pp.871-877.

35. L. Shouxin, L. Sun, Q. Zang, and Z. Wang (1992), Mater. Science Engng, Vol.150, pp.209-212.

36. R. L. Carlson, and C. J. Beevers (1985), Engng Fract. Mech., Vol. 22, pp.651-660.

37. E. K. Tschegg (1983), Acta Metallurgica, Vol.31, pp.1323-1330.

38. W. Geary (1992), Int. J. Fatigue, Vol.14, No.6, pp.377-386.

39. R. I. Stephens, D. K. Chen, and B. W. Hom (1976), ASTM STP 595, pp.27-40.

40. N. Ohrloff, A. Gysler, and G. Lutjering (1988), in: Fatigue Crack Growth under Variable Amplitude Loading, J. Petit, D. L. Davidson, S. Suresh, and P. Rabbe, Eds., Elsevier Science Publishers, pp.24.

41. S. Suresh (1988), in: Fatigue Crack Growth under Variable Amplitude Loading, J. Petit, D. L. Davidson, S. Suresh, and P. Rabbe, Eds., Elsevier Science Publishers, pp.146-161.

42. T. H. Topper, D. L. DuQuesnay, and M. A. Pompetzki (1992), in: Theoretical Concepts and Numerical Analysis of Fatigue, A. F. Blom, C. J. Beevers, Eds., Birmingham, pp.201-235.

43. T. H. Topper, and M. T. Yu (1985), Int. J. Fatigue, Vol.7, No.3, pp.159-164.

44. A. Varvani-Farahani and T. H. Topper (1997), Int. J. Fatigue, Vol.19, No.7, pp.589-596.

45. A. Varvani-Farahani and T. H. Topper (1997), Proceedings of the 5th International Conference on Biaxial/ Multiaxial Fatigue and Fracture, E. Macha, and Z. Mroz, Eds., Poland, Vol.II, pp.149-166.

46. H. Kemper, B. Weiss, and R. Stickler (1989), Engng Fract. Mech., Vol.4, pp.591-600.

47. A. J. Tack, and C. J. Beevers (1990), Proceedings of the 4th International Conference on Fracture and Fatigue Thresholds, Honolulu, pp.1179-1184.

48. A. Varvani-Farahani and T. H. Topper (1996), in: "Fatigue 96"-Proceedings of the 6th International Fatigue Congress, C. Lutjering, and H. Nowack, Eds., Germany, pp.295-300.

49. A. Mendelson (1968), Plasticity: Theory and Application, First Edition, MacMillan company, New York.

50. G. Glinka (1997), Course Notes-ME 620, Mechanics of Continua, Mech. Engng. Dept., University of Waterloo, Fall 1997.

51. M. A. Pompetzki, R. A. Saper, and T. H. Topper (1986), Can. Metall. Q., Vol.25, No.2, pp.181-194.

52. C. MacDougall and T. H. Topper (1997), Int. J. Fatigue, Vol.19, No.5, pp.389-400.

53. L. Wagner, J. K. Gregory, A. Gysler, and C. Lutjering (1986), in: Small Fatigue Cracks, R. O. Ritchie, and J. Lankford, Eds., TMS-AIME, Warrendale, PA, pp.117-128.

54. R. P. Gangloff (1981), in: Fatigue Crack Growth Measurements and Data Analysis, ASTM STP738, S. Y. Hudak, and R. J. Bucci, Eds., ASTM, Philadelphia, PA, pp.120-138.

55. O. Vosikovsky, and A. Rivard (1981), Int. J. Fatigue, Vol.3, pp.111-115.

56. B. London, J. C. Shyne, and D. V. Nelson (1986), in: The Behaviour of Short Fatigue Cracks, K. J. Miller, and E. R. de los Rios, Eds., Mechanical Engineering Publications, London, pp.537-552.

57. W. J. Baxter (1983), Int. J. Fatigue, Vol.5, pp.37-42.

58. A. Varvani-Farahani, T. H. Topper, and A. Plumtree (1996), Fatigue Fract. Engng Mater. Struct., Vol.19, No.9, pp.1153-1159.

59. A. Varvani-Farahani, and T. H. Topper (1997), ASTM STP 1318, G. F. Lucas, D. A. Stubbs, Eds., Florida, pp.43-55.

60. S. M. Marco, and W. L. Starkey (1954), Transaction of ASME, Vol.76, pp.627-632.

61. W. Yu, and R. O. Ritchie (1987), Journal of Engineering Materials and Technology, Vol.109, pp.81-85.

62. R. L. Carlson and G. A. Kardomatead (1994), Int. J. Fatigue, Vol.16, pp.141-146.

63. E. Zaken, and R. O. Ritchie (1985), Engng Fract. Mech., Vol.22, pp.35-48.

64. J. A. Henkener, T. D. Scheumann, and A. F. Grandt (1990), in: Proc. 4th Int. Conf. on Fatigue and Fracture Threshold, Honolulu, pp.957-962.

65. W. A. Herman, R. W. Hertzberg, and R. Jaccard (1989), in: Advance Fracture Research, 7th Int. Conf. on Fracture, Houston, pp.1417.

66. R. W. Hertzberg, W. A. Herman, T. Clark, and R. Jaccard (1992), in: Small-Crack Test Methods, ASTM STP 1149, pp.197-220.

67. M. A. Pompetzki, T. H. Topper, and D. L. DuQuesnay (1990), Int. J. Fatigue, Vol.12, pp.207-213.

68. K. Minakawa, H. Nakamura, and J. McEvilly (1984), Scripta Metallurgica, Vol.18, pp.1371-1374.

69. A. A. Dabayeh, T. H. Topper (1995), Int. J. Fatigue, Vol.17, No.4, pp.261-269.

70. K. J. Johnson (1985), in: Contact Mechanics, Cambridge University Press, First Edition.

71. A. Varvani-Farahani and T. H. Topper (1997), Presented and Submitted to the Second Symposium on Advances in Fatigue Crack Closure Measurement and Analysis, Second Volume, ASTM STP 1343, San Diego, Nov.1997.

72. G. Sines and J. L. Waisman (1959), in: Metal Fatigue, Mc Grow-Hill, pp. 145-167.

73. G. Taira, J. Inoue, and M. Takashashi (1967), in: Low Cycle Fatigue under Multiaxial Stresses, 10th Japan Congress on Testing Materials, pp.18-23.

74. K. J. Pascoe, and J. W. R. Devilliers (1967), Journal of Strain Analysis, Vol.2, pp.117-126.

75. T. Yokobori, H. Yamaouahi, and S. Yammamoto (1965), Int. J. Fract. Mech., Vol.1, pp.3-13.

76. D. G. Havard, and T. H. Topper (1971), Third Canadian Congress of applied Mechanics, Calgary, pp.235-236.

77. F. Ellyin and B. Valaire (1982), ASME Journal of Engng Mater. Tech., Vol.104, pp.165-173.

78. D. Socie (1987), ASME, j. Engng Mater. Tech., Vol.109, pp.293-298.

79. A. Fatemi and P. Kurath (1988), ASME, J. Engng Mater. Tech., Vol.110, pp.380-388.

80. D. F. Socie, C. T. Hau, and D. W. Worthem (1987), Fatigue Fact. Engng Mater. Struct., Vol.10, No.1, pp.1-16.

81. J. Y. Berard and A. McDowell (1991), in: Fatigue under Biaxial and Multiaxial Loading, ESIS10, K. Kussmaul, D. McDiarmid, and D. Socie, Eds., Mechanical Engineering Publication, London, pp.413-431.

82. J. Y. Berard, D. L. McDowell, and S. D. Antolovich (1993), in: Advances in Multiaxial Fatigue, ASTM STP 1191, D. L. McDowell, and R. Ellis, Eds., ASTM, pp.326-344.

83. J. Qian and A. Fatemi (1996), Engng Fract. Mech.,Vol.55, No.6, pp.969-990.

84. M. H. El-Haddad, K. N. Smith, and T. H. Topper (1979), ASTM STP 677, pp.274-289.

85. H. S. Kitagawa, S. Takahashi, C. M. Suh, and S. Miyashita (1979), ASTM STP675, pp.420-449.

86. Y. Imai and T. Matake (1983), Japanese Society of Material Science, Vol.32, pp.1157-1161.

87. H. Abdel-Raouf, T. H. Topper, and A. Plumtree (1992), Int. J. Fatigue, Vol.14, pp.57-62.

88. M. W. Brown and K. J. Miller (1985), in: Multiaxial Fatigue, ASTM STP 853, K. J. Miller, and M. W. Brown, Eds., American Society for Testing and Materials, Philadelphia, pp.135-152.

89. K. Tanaka, S. Matsuoka, and M. Kimura (1984), Fatigue Fract. Engng Mater. Struct., Vol.7, pp.195-211.

90. G. R. Irwin (1962), Journal of Applied Mechanics, Transaction of ASME, Vol.29, pp.651-654.

91. A. E. Green, and I. N. Sneddon (1950), Proc. Cambridge Phil. Soc., Vol.46, pp.159-164.

92. M. Kassir and G.C. Sih (1966), Journal of Applied Mechanics, Transaction of ASME, Vol.33, pp.601-611.

93. H. Sehitoglu, D. F. Socie, and D. Worthem (1988), in: Basic Questions in Fatigue, J. T. Fong and R. J. Fields, Eds., ASTM STP 924, Vol.1, pp.120-135.

94. F. Ellyin (1997) in: Fatigue Damage, Crack Growth and Life Prediction, First Edition, Chapman & Hall.

IMAGE EVALUATION
TEST TARGET (QA-3)

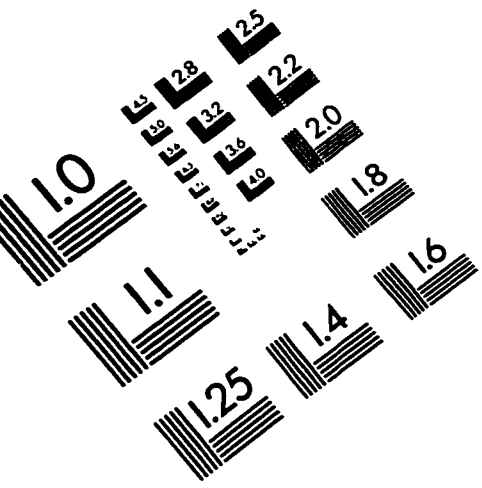

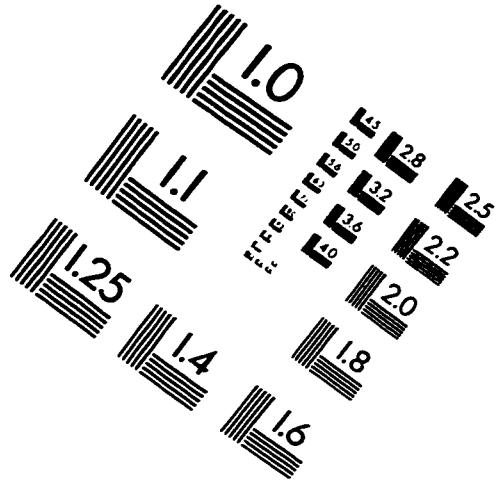

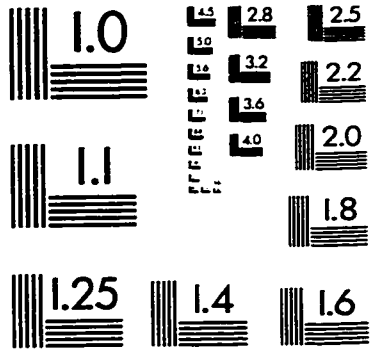

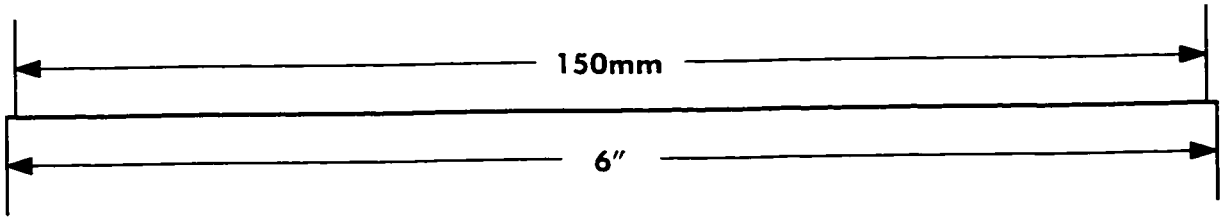

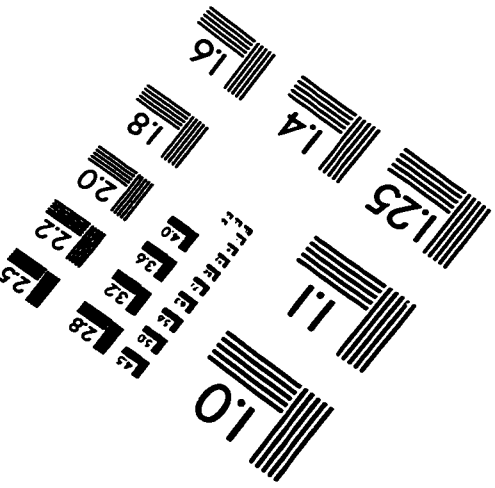

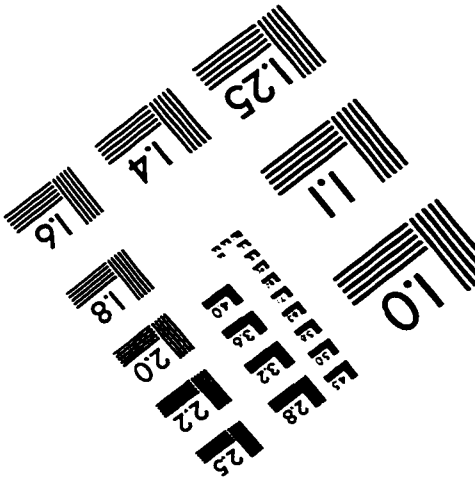

APPLIED IMAGE, Inc
1653 East Main Street
Rochester, NY 14609 USA
Phone: 716/482-0300
Fax: 716/288-5989